

LATTICE BOLTZMANN SIMULATIONS OF MULTIPHASE FLOWS

BY

JEREMY AARON KOLKER HORWITZ

THESIS

Submitted in partial fulfillment of the requirements
for the degree of Master of Science in Mechanical Engineering
in the Graduate College of the
University of Illinois at Urbana-Champaign, 2013

Urbana, Illinois

Advisor:

Professor S. Pratap Vanka

ABSTRACT

This thesis is a comprehensive account of my experiences implementing the Lattice Boltzmann Method (LBM) for the purpose of simulating multiphase flows relevant to Air Conditioning and Refrigeration Center (ACRC) applications. Other methodologies have been used to simulate multiphase flow including finite volume based Navier-Stokes solvers. These methods have found reasonable success in simulating multiphase flows. LBM was chosen because of its ability to capture multi-fluid physics including phase-change and interfacial dynamics with relative ease. In addition, the LBM algorithm can be easily parallelized. This allows larger problems to be simulated quicker. Among the multiphase LBM algorithms, we have implemented the Shan-Chen method, the He-Chen method, and an extension to the He-Chen method. We carefully document our methodology and discuss relevant kinetic theory and fluid dynamics. We present results for a number of fundamental flow problems including droplet impingement on solid and liquid surfaces as well as multiphase flow in complex micro-channels. In addition, we examine in great detail the problem of axial droplet migration and deformation in a square-duct at moderate Reynolds number. Our results suggest that the LBM algorithm is capable of simulating a wide range of flows and can accurately capture flow physics provided the density ratio among fluid phases is not large. Because ACRC equipment often harbor high density ratio flows, the standard LBM procedures require modification to accommodate higher density ratio problems. We investigate one such modification to the He-Chen algorithm by introducing a pressure Poisson equation (PPE) to reduce density variation related to compressibility effects.

DEDICATION

To my family: my father Michael, my mother Elaine, and my sister Deborah, for protecting me, keeping me, and allowing me to reach this season.

ACKNOWLEDGEMENT

I would like to acknowledge the Air Conditioning and Refrigeration Center (ACRC) for its generous support of this work. I would like to express my sincere thanks to Ramnik Singh, Professor Johnathan Freund, Professor Kirti Sahu, and especially my advisor Professor Pratap Vanka for tremendously valuable discussions. I would like to express my gratitude to Professor Pega Hrnjak and his students, Aravind Ramakrishnan and Hanfei Tuo for their insight regarding measurement and physical intuition of multiphase flows. I would also like to thank my colleague Purushotam Kumar, whom I worked with closely on this project, who was tremendously helpful in the development phase for each of the LBM codes. A portion of the results in this thesis were obtained under close collaboration with him. These contributions are gratefully noted.

TABLE OF CONTENTS

| | |
|---|-----|
| LIST OF FIGURES | vi |
| LIST OF TABLES | xi |
| NOMENCLATURE | xii |
| 1. INTRODUCTION | 1 |
| 2. THE LATICE BOLTZMANN METHOD (LBM) | 4 |
| 3. SIMULATION OF DISPERSED MULTIPHASE FLOW IN A CHANNEL | 54 |
| 4. SIMULATION OF DROPLET IMPINGEMENT AND COLLISION | 79 |
| 5. SIMULATION OF FLOW IN MICRO-CHANNELS | 95 |
| 6. DEFORMATION OF A LIQUID DROPLET IN A SQUARE DUCT..... | 107 |
| 7. CONCLUSIONS..... | 146 |
| REFERENCES | 148 |
| APPENDIX..... | 160 |

LIST OF FIGURES

Chapter 2

| | |
|--|----|
| <i>Figure 2.1:</i> Discretized Simulation Domain..... | 6 |
| <i>Figure 2.2:</i> D2Q9 Lattice..... | 7 |
| <i>Figure 2.3:</i> Pictorial representation of the streaming process..... | 9 |
| <i>Figure 2.4:</i> Pictorial representation of the collision process..... | 10 |
| <i>Figure 2.5:</i> Flowchart of typical LBM Algorithm..... | 12 |
| <i>Figure 2.6:</i> Diagram of Ghost-Fluid boundary condition..... | 13 |
| <i>Figure 2.7:</i> Bounce-back boundary condition..... | 15 |
| <i>Figure 2.8:</i> System of two stratified fluids..... | 24 |
| <i>Figure 2.9:</i> Hypothetical EOS for $T < T_c$, reproduced from [71] | 26 |
| <i>Figure 2.10:</i> Phase Separation of a 1 component fluid. Initial density field random with a prescribed 1% perturbation about a density value of 1.00..... | 27 |
| <i>Figure 2.11:</i> GPU vs. CPU theoretical peak performance, variation with time, reproduced from [43]..... | 44 |
| <i>Figure 2.12:</i> G80 and GT200 GPU architectures, reproduced from [9]..... | 45 |
| <i>Figure 2.13:</i> CUDA code, main source code containing kernel calls (top), kernel code (bottom) | 46 |
| <i>Figure 2.14:</i> Speedup between GPU and CPU code for different problem sizes..... | 47 |
| <i>Figure 2.15:</i> LBM Algorithm Flowcharts: He-Chen Algorithm , Pressure Poisson Modification, Shan-Chen Algorithm | 50 |

Chapter 3

| | |
|--|----|
| <i>Figure 3.1:</i> Simulation domain for PPE study..... | 56 |
| <i>Figure 3.2:</i> Density Ratio Study, $Ma = 0.00577$, $Re = 10$, $k = 0.0$ | 60 |
| <i>Figure 3.3:</i> Density Ratio Study, $Ma = 0.00577$, $Re = 10$, $k = 0.0$ | 60 |

| | |
|--|----|
| <i>Figure 3.4:</i> Surface Tension Study, $\text{Ma} = 0.00577$, $\text{Re} = 10$, $\rho_1/\rho_2 = 2.0$ | 62 |
| <i>Figure 3.5:</i> Surface Tension Study, $\text{Ma} = 0.00577$, $\text{Re} = 10$, $\rho_1/\rho_2 = 0.5$ | 62 |
| <i>Figure 3.6:</i> Mach number Study, $\text{Re} = 10$, $\rho_1/\rho_2 = 2.0$, $k = 0.1$ | 64 |
| <i>Figure 3.7:</i> Mach number Study, $\text{Re} = 10$, $\rho_1/\rho_2 = 0.5$, $k = 0.1$ | 64 |
| <i>Figure 3.8:</i> Density variation compared with static conditions as a function of Mach number for an ideal gas. | 66 |
| <i>Figure 3.9:</i> Reynolds Number Study, $\text{Ma} = 0.0115$, $\rho_1/\rho_2 = 2.0$, $k = 0.1$ | 68 |
| <i>Figure 3.10:</i> Reynolds Number Study, $\text{Ma} = 0.0115$, $\rho_1/\rho_2 = 0.5$, $k = 0.1$ | 68 |
| <i>Figure 3.11:</i> Case 8a: $\text{Re} = 10$, $\text{Ma} = 0.00577$, $\rho_1/\rho_2 = 2.0$, $k = 0.01$ | 70 |
| <i>Figure 3.12:</i> Case 9a: $\text{Re} = 10$, $\text{Ma} = 0.00577$, $\rho_1/\rho_2 = 2.0$, $k = 0.1$ | 71 |
| <i>Figure 3.13:</i> Case 10a: $\text{Re} = 10$, $\text{Ma} = 0.00577$, $\rho_1/\rho_2 = 2.0$, $k = 1.0$ | 72 |
| <i>Figure 3.14:</i> Case 11a: $\text{Re} = 10$, $\text{Ma} = 0.00577$, $\rho_1/\rho_2 = 2.0$, $k = 2.0$ | 73 |
| <i>Figure 3.15:</i> Case 12a: $\text{Re} = 10$, $\text{Ma} = 0.00577$, $\rho_1/\rho_2 = 0.5$, $k = 0.01$ | 74 |
| <i>Figure 3.16:</i> Case 13a: $\text{Re} = 10$, $\text{Ma} = 0.00577$, $\rho_1/\rho_2 = 0.5$, $k = 0.1$ | 75 |
| <i>Figure 3.17:</i> Case 14a: $\text{Re} = 10$, $\text{Ma} = 0.00577$, $\rho_1/\rho_2 = 0.5$, $k = 1.0$ | 76 |
| <i>Figure 3.18:</i> Case 15a: $\text{Re} = 10$, $\text{Ma} = 0.00577$, $\rho_1/\rho_2 = 0.5$, $k = 2.0$ | 77 |
| <i>Figure 3.19:</i> Case 8a: $\text{Re} = 10$, $\text{Ma} = 0.00577$, $\rho_1/\rho_2 = 2.0$, $k = 0.01$, top: without PPE equation, bottom: with PPE equation..... | 78 |

Chapter 4

| | |
|---|----|
| <i>Figure 4.1:</i> Definition of Contact Angle..... | 80 |
| <i>Figure 4.2:</i> Droplet Impingement on a smooth surface, $\theta = 27^\circ$ (left) and $\theta = 82^\circ$ (right). | 84 |
| <i>Figure 4.3:</i> Droplet Impingement on a textured surface, $\rho_h/\rho_l = \lambda = 2.0$, $\text{Re} = 180$ | 86 |
| <i>Figure 4.4:</i> Droplet impingement on a solid surface (left), and liquid pool (right), $\rho_h/\rho_l = 60$, $\lambda = 100$, droplet velocity = 0.05 l.u./s..... | 88 |
| <i>Figure 4.5:</i> Droplet Impingement on a smooth surface, isometric (left) and top view | |

| | |
|---|----|
| (right), $\rho_h/\rho_l = 60$, $\lambda = 120$, droplet velocity = 0.05 l.u./s..... | 90 |
|---|----|

| | |
|---|----|
| <i>Figure 4.6:</i> 2 droplets approach with identical velocity, collide and coalesce. density ratio = 60, viscosity ratio = 100 (left) and 120 (right), droplet velocity = 0.05 l.u./s..... | 92 |
|---|----|

| | |
|--|----|
| <i>Figure 4.7:</i> Oblique binary droplet collision, $\zeta = 0^\circ$, $\varphi = 73.3^\circ$ (left), $\zeta = 45^\circ$, $\varphi = 73.3^\circ$ (right)..... | 94 |
|--|----|

Chapter 5

| | |
|---|----|
| <i>Figure 5.1:</i> Displacement flow in a channel. Contours of index function. Case 1: At = 0.5 (left), Case 2: At = 0.85 (right). $\lambda = 20$ for both cases..... | 99 |
|---|----|

| | |
|---|----|
| <i>Figure 5.2:</i> Displacement flow in a channel. At = 0, $\lambda = 0.9$. Contours of index function.... | 99 |
|---|----|

| | |
|---|-----|
| <i>Figure 5.3:</i> Droplet formation in a T-junction, Density ratio = 1, Viscosity ratio = 1, channel width ratio = 1 | 102 |
|---|-----|

| | |
|--|-----|
| <i>Figure 5.4:</i> Liquid-vapor jetting and slug flow in a T-junction, geometric effect, density ratio = 5, viscosity ratio = 5, Q = 8, a) channel width ratio = 1, b) channel width ratio = $\frac{1}{2}$ | 103 |
|--|-----|

| | |
|--|-----|
| <i>Figure 5.5:</i> Liquid-vapor jetting and slug flow in a T-junction, effect of viscosity ratio, density Ratio = 5, flow rate ratio = 8 and channel width ratio = 1, a) viscosity ratio = 5, b) viscosity ratio = 10..... | 104 |
|--|-----|

| | |
|--|-----|
| <i>Figure 5.6:</i> Displacement flow in complex geometries. Contours of index function. Case 1: Flow in a cross-junction (left), Case 2: Flow in a distributor header (right). At = 0.3, and viscosity ratio = 0.9 for both cases..... | 105 |
|--|-----|

| | |
|---|-----|
| <i>Figure 5.7:</i> Array of droplets flowing in a T-junction, $\rho_h/\rho_l = 2$, $\lambda = 2$, Re = 9..... | 106 |
|---|-----|

Chapter 6

| | |
|---|-----|
| <i>Figure 6.1:</i> Simulation domain and droplet initial condition..... | 111 |
|---|-----|

| | |
|--|-----|
| <i>Figure 6.2:</i> Algorithm validation with boundary element simulation of low Reynolds number droplet deformation in a square duct, $\lambda = 2.04$, confinement = 0.8, LBM results (dashes), results reproduced from [78] (solid and dotted lines)..... | 116 |
|--|-----|

| | |
|--|-----|
| <i>Figure 6.3:</i> Effect of interface definition on deformation results, Ca = 0.1, Confinement = 0.8, Re = 2..... | 118 |
|--|-----|

| |
|--|
| <i>Figure 6.4:</i> Droplet contours, geometric definitions, grid resolution (a) 3D droplet contour, isometric view, (b) side view, (c) 2D horizontal slice, initial droplet shape, (d) 2D horizontal slice, transient droplet shape, (e) 2D droplet contour overlaid with finest grid, |
|--|

| | |
|--|-----|
| (f) zoomed view of droplet contour overlaid with finest grid. $Ca = 0.25$, $Re = 100$, $\lambda = 1$... | 120 |
| <i>Figure 6.5:</i> Grid study, legends correspond to duct cross-section. $Ca = 0.25$, $Re = 100$, $\lambda = 1$ | 123 |
| <i>Figure 6.6:</i> Droplet contour history for different capillary numbers, $Re = 100$, $\lambda = 1$ | 124 |
| <i>Figure 6.7:</i> Capillary number study, elongation (a) maximum, (b) axial, (c) difference, $Re = 100$, $\lambda = 1$ | 125 |
| <i>Figure 6.8:</i> Capillary number study, (a) spreading, (b) deformation, $Re = 100$, $\lambda = 1$ | 126 |
| <i>Figure 6.9:</i> Duct center-plane stream-wise velocity contours overlaid with two-dimensional droplet shape, $Ca = 0.25$, $\lambda = 1$, $Re = 100$, (a) $t^* = 2$, (b) $t^* = 4$, (c) $t^* = 5$, (d) $t^* = 6$, (e) $t^* = 8$, (f) $t^* = 10.7$ | 128 |
| <i>Figure 6.10:</i> Duct center-plane wall-normal velocity contours overlaid with two-dimensional droplet shape, $Ca = 0.25$, $\lambda = 1$, $Re = 100$, (a) $t^* = 2$, (b) $t^* = 4$, (c) $t^* = 5$, (d) $t^* = 6$, (e) $t^* = 8$, (f) $t^* = 10.7$ | 129 |
| <i>Figure 6.11:</i> Characteristic time when $E - E_A$ is a maximum for different capillary numbers, $Re = 100$, $\lambda = 1$ | 130 |
| <i>Figure 6.12:</i> Droplet contour history for different Reynolds numbers, $Ca = 0.25$, $\lambda = 1$ | 131 |
| <i>Figure 6.13:</i> Reynolds number study, elongation (a) maximum, (b) axial, (c) difference, $Ca = 0.25$, $\lambda = 1$ | 132 |
| <i>Figure 6.14:</i> Reynolds number study, (a) spreading, (b) deformation, $Ca = 0.25$, $\lambda = 1$ | 133 |
| <i>Figure 6.15:</i> Characteristic time when $E - E_A$ is a maximum for different Reynolds numbers, $Ca = 0.25$, $\lambda = 1$ | 135 |
| <i>Figure 6.16:</i> Droplet contour history for different viscosity ratios, $Ca = 0.25$, $Re = 100$... | 136 |
| <i>Figure 6.17:</i> Viscosity Ratio study, elongation (a) maximum, (b) axial, (c) difference, $Ca = 0.25$, $Re = 100$ | 137 |
| <i>Figure 6.18:</i> Viscosity ratio study, (a) spreading, (b) deformation, $Ca = 0.25$, $Re = 100$.. | 138 |
| <i>Figure 6.19:</i> Droplet contour history for different viscosity ratios (continued), $Ca = 0.25$, $Re = 100$ | 140 |
| <i>Figure 6.20:</i> Viscosity ratio study (continued), elongation (a) maximum, (b) axial, (c) difference, $Ca = 0.25$, $Re = 100$ | 141 |

Figure 6.21: Viscosity ratio study (continued), (a) spreading, (b) deformation, $Ca = 0.25$, $Re = 100$ 142

Figure 6.22: Characteristic time when $E - E_A$ is a maximum for different viscosity ratios, $Ca = 0.25$, $Re = 100$ 143

Figure 6.23: Velocity contours overlaid with 2D droplet interface for two viscosity ratios, (a) and (b) stream-wise velocity normalized by mean stream-wise velocity, (c) and (d) wall-normal velocity normalized by mean stream-wise velocity, $\lambda = 1$ for (a) and (c), $\lambda = 16$ for (b) and (d), $Re = 100$, $Ca = 0.25$, $t^* = 4$ for both cases..... 145

Appendix

Figure A.1: Instantaneous snapshot of molecules and their respective velocity vectors in an arbitrary control volume. 160

Figure A.2: Transition from discrete to continuous particle distribution as the number of molecules sampled becomes large..... 162

LIST OF TABLES

Chapter 3

| | |
|---|----|
| <i>Table 3.1:</i> Geometric Parameters, channel flow simulations with and without PPE..... | 56 |
| <i>Table 3.2:</i> Effect of PPE on calculation of developing channel flow varying the density ratio, a-No PPE, b-PPE..... | 57 |
| <i>Table 3.3:</i> Effect of PPE on calculation of developing channel flow varying the density ratio, a-No PPE, b-PPE..... | 57 |
| <i>Table 3.4:</i> Effect of PPE on calculation of developing channel flow varying the surface tension, a-No PPE, b-PPE..... | 57 |
| <i>Table 3.5:</i> Effect of PPE on calculation of developing channel flow varying the surface tension, a-No PPE, b-PPE..... | 57 |
| <i>Table 3.6:</i> Effect of PPE on calculation of developing channel flow varying the Mach number, a-No PPE, b-PPE..... | 58 |
| <i>Table 3.7:</i> Effect of PPE on calculation of developing channel flow varying the Mach number, a-No PPE, b-PPE..... | 58 |
| <i>Table 3.8:</i> Effect of PPE on calculation of developing channel flow varying the Reynolds number, a-No PPE, b-PPE..... | 58 |
| <i>Table 3.9:</i> Effect of PPE on calculation of developing channel flow varying the Reynolds number, a-No PPE, b-PPE..... | 58 |

Chapter 6

| | |
|---|-----|
| <i>Table 6.1:</i> List of cases for droplet deformation in a square duct study..... | 115 |
|---|-----|

NOMENCLATURE

Symbols

| | |
|--------|--|
| At | Atwood Number |
| a | Repulsion parameter |
| b | EOS parameter |
| Ca | Capillary Number |
| c | Lattice speed |
| c_s | Speed of sound |
| D | Deformation |
| D/Dt | Material Derivative |
| d | Droplet Diameter |
| E_A | Axial Elongation |
| E_T | Total Elongation |
| e_i | Discrete velocity vectors |
| F | Force |
| f, g | Particle Distribution Function |
| f_i | Component of distribution function f in i^{th} -direction |
| G | Interaction Strength |
| H | Channel, Duct Height |
| $I(a)$ | Interfacial Integral |
| L | Droplet Initial Length |
| L_A | Droplet Axial tip-to-tip distance |
| L_T | Droplet Stream-wise tip-to-tip distance |
| l | Channel Length |
| Ma | Mach Number |
| N | Particle density function |
| N_T | Total number of molecules |
| p | Pressure |
| Q | Flow Rate Ratio |

| | |
|------------|---|
| R | Specific Gas Constant |
| Re | Reynolds Number |
| r | Duct Half-Height |
| S | Spread Factor |
| T | Temperature |
| Δt | Time Step |
| t^* | Characteristic Time |
| u, U | Velocity |
| V | Specific Volume |
| W | Droplet Initial Width |
| W_T | Droplet Wall-normal tip-to-tip distance |
| We | Weber Number |
| w_i | Quadrature Weights |
| Δx | Grid Spacing |

Abbreviations

| | |
|------|--------------------------------|
| CPU | Central Processing Unit |
| C-S | Carnahan-Starling |
| EOS | Equation of State |
| GPU | Graphics Processing Unit |
| H-C | He and Chen |
| L.U. | Lattice Units |
| PDF | Particle Distribution Function |
| PPE | Pressure Poisson Equation |
| S-C | Shan and Chen |

Superscripts and Subscripts

| | |
|-----------|-----------------|
| 1 | Fluid 1 |
| 2 | Fluid 2 |
| c | critical |
| eq | equilibrium |
| g | gas |
| l | liquid |
| n | Fluid n |
| \bar{n} | Fluid \bar{n} |
| s | solid |

Greek Letters

| | |
|------------|-------------------------------|
| β | Quality Factor |
| γ | Specific heat ratio |
| κ | Interfacial tension parameter |
| ξ | Continuous molecular velocity |
| λ | Dynamic viscosity ratio |
| μ | Dynamic viscosity |
| ∇ | Gradient |
| ∇^2 | Laplacian |
| ν | Kinematic viscosity |
| φ | Polar Angle |
| ϕ | Index Function |
| ψ | Interaction Potential |
| ρ | Density |
| σ | Surface/Interfacial Tension |
| τ | Relaxation time |
| θ | Contact angle |
| ζ | Azimuthal Angle |

1. INTRODUCTION

Multiphase flows are of great interest to scientists from a theoretical standpoint, who seek to understand their fundamental physics, as well as to engineers from a practical standpoint, who perform flow analysis which affects engineering design in a broad range of applications. The term “multiphase” flow can have different definitions depending on the application so the term should be defined to avoid ambiguity. By “multiphase” flow, we mean any flow where the system dynamics cannot be adequately described by the equations of motion corresponding to a single fluid. One example of such a flow is any particle-laden flow where fluid-particle interactions alter the trajectories of both particles and fluid elements. Other examples include atmospheric transport and clustering of rain droplets in clouds, any interaction at a free surface between two fluids such as that found between the ocean and the atmosphere, and the boiling of water on a stove-top. Hence, “multiphase” can refer to any system involving more than one component as long as one of the components is considered a fluid, be it Newtonian or non-Newtonian, in some practical regime. Therefore, the term “phase” has been generalized from the thermodynamic sense. Discounting any interaction with a free surface, the boiling of water on a stove-top is an example where there exists two thermodynamic phases of the same fluid (water). The free-surface interaction between the ocean and atmosphere is a two-phase system comprised of two Newtonian fluids with no equation of state (EOS) linking the fluids. Particle-laden flows such as those concerning atmospheric interaction with sand dunes involve a Newtonian fluid (air) and a second non-fluid phase (sand particles). Under our definition, all of these are considered multiphase flows.

In multiphase flow problems, it is often helpful to demarcate fluids by their relative influence on global system dynamics. Consider flow in a pipe containing oil and small pockets of

trapped air. In this case, the oil is typically referred to as the “primary” or “carrier” phase, while the air is referred to as the “secondary” or “dispersed” phase. In systems involving more than two phases, additional phases may be referred to as “tertiary” or the system may be said to have two “secondary” phases. In some sense, the labeling of phases is arbitrary since there exists non-trivial coupling between phases in most systems where the single-phase flow equations are not suitable. Nonetheless, we will try to adopt a consistent convention in referring to a fluid with the highest volume fraction as the “carrier” fluid and other phases that may be present as “secondary” phases. When the volume fraction of all phases is comparable, we may refer to the multiphase system as “binary,” or “ternary,” etc. where appropriate. In addition, to avoid confusion, we will refer to multiphase systems as having multiple “components” when we want to emphasize the two fluids are immiscible liquids, say, which do not share an EOS under normal conditions. In systems where phase-change is possible, say between water and water-vapor, we will be careful to emphasize this thermodynamic possibility by identifying the two fluids as “phases.”

Having identified the relevance of multiphase flow to many practical regimes as well as introduced some of the necessary vocabulary needed to describe these flows, we can now identify the purpose of this thesis. Our source of funding for this work is the Air Conditioning and Refrigeration Center (ACRC) at the University of Illinois Urbana-Champaign. ACRC is funded by the National Science Foundation (NSF) as well as a consortium of industry sponsors in ACRC-related fields. Our goal was to conduct scientific investigations of multiphase flows in regimes relevant to ACRC applications. These applications include multiphase flow in heat exchangers, distributor headers, and other complex geometries. These flows often involve heat transfer and phase-transition as well as the interaction of liquid droplets or gaseous bubbles with

a carrier fluid. Significant experimental work has been done in recent decades by Professors Pega Hrnjak and Anthony Jacobi and others at the University of Illinois on ACRC-related applications. To complement their empirical investigations, our group has sought to develop computational strategies to evince fundamental insight into multiphase problems relevant to ACRC. Therefore, the purpose of this thesis is to document the computational approaches we investigated. We will address the advantages and short-comings of these methods, present our findings, and discuss what work can be done in the future. The remainder of the paper is organized as follows: Chapter 2 provides an introduction to the chosen computational methodology, the Lattice Boltzmann Method (LBM). We discuss in detail two of the methods widely used in literature and discuss a modification to one of the former methods. In the remaining chapters, we present and discuss results obtained from the LBM methods we have implemented. In Chapter 3 we present results for two-dimensional dispersed flow in a channel with an emphasis on demonstrating the modified algorithm presented in Chapter 2. In Chapter 4, we present two-dimensional droplet impingement and collision results. In Chapter 5 we explore droplet flow in complex micro-channels. Chapter 6 is devoted to a systematic analysis of droplet deformation in a three-dimensional square duct. Concluding remarks are followed by supplementary material in the Appendix. For deeper insight into the LBM method, the curious reader is strongly encouraged to read Appendix A, which contains a short theoretical discussion, before reading further.

2. THE LATTICE BOLTZMANN METHOD (LBM)

2.1 Introduction

In this section, we present the details of the single-phase LBM algorithm. The reader is strongly encouraged to review to Appendix A for additional theory relevant to the derivation of the LBM equations before reading further.

Since its inception more than twenty years ago, LBM has proved to be a versatile computational fluid dynamics procedure, particularly in its use for simulating multiphase, multicomponent fluid systems. Among its application to such multiphase fluid systems, LBM has been used to simulate the Rayleigh-Taylor Instability [71, 28], droplet flow in T-junctions [4, 3, 6], bubble-rise dynamics [35], and droplet impingement on surfaces of varying contact angle [69, 2, 5]. The multiphase LBM algorithm is a special case of the single-phase algorithm, where the distinction comes from additional treatment to model interaction between different fluids.

The first widely adopted LBM procedure for multiphase systems was introduced by Gustensen and Rothman [8] in 1991. Gustensen’s method, commonly referred to in literature as the “Color-Method,” represents distinct fluid components by color functions who each separately evolve via their own discretized Boltzmann equation, and which interact with each other via local color gradients. In 1993, Shan and Chen [75] introduced the pseudo-potential method which gave a simple expression relating interaction forces between disparate fluid phases and each fluid’s equation of state. Swift et. al [38] developed an LBM algorithm capable of simulating multiple fluids and modeled interaction forces by a free-energy potential. Inamuro et al. [64] extended the work of Swift et al. by introducing an order parameter to demarcate fluids and also explored the effect of adding a Poisson equation into the LBM framework. An algorithm developed earlier by He and Chen [71] also used an order-like parameter, as well as an

interaction potential similar that used in Shan and Chen's method. All LBM algorithms for multiphase flows, to the best of our knowledge are derivatives of the above formulations. Furthermore, the above methods are themselves essentially derivatives of each other. The main difference among multiphase LBM formulations is the treatment of the interface between fluid phases and the approach used to model interaction forces. What is consistent among all LBM procedures is the modeling of a fluid on a mesoscopic scale by a single particle distribution function which evolves according to a discretized Lattice Boltzmann equation [71]. Macroscopic characteristics of a fluid such as density and velocity are related to the moments of the distribution function. Such a model is suitable in situations in which the continuum hypothesis applies¹.

We build up to the multiphase LBM algorithms by first discussing the relatively simple single-phase LBM algorithm. Before introducing the LBM equations, it is necessary to introduce the general method of discretization used in LBM algorithms. In LBM, the principal discretized quantity, the particle distribution function, is dependent on velocity, space, and time. Most LBM algorithms, including those discussed in this report are analogous to finite difference methods with respect to spatial and temporal discretization. That is, derivatives are approximated using truncated Taylor expansions. The notion of velocity discretization however is less obvious. Whereas the macroscopic fluid velocity is the dependent variable in the Navier-Stokes equations (the quantity that is solved for), velocity, specifically molecular velocity is an independent variable in the pdf formulation. Interestingly, the S-C evolution for the n^{th} pdf will contain no explicit instance of the molecular velocity. Recall as well that the continuous evolution equation for a single pdf given in (6) of Appendix A similarly did not contain an explicit derivative of molecular velocity. The most apparent reason to discretize velocity space then is to approximate

¹ See Appendix A.

the integral moments for density and momentum given in (A.3), (A.4) of Appendix A by means of quadrature.

Consider *Figure 2.1* which represents a subset of a discretized two-dimensional domain.

The horizontal grid spacing is Δx and the vertical grid spacing is Δy . For the moment, it is not necessary to assume uniform grid spacing. However, we will now introduce the concept of a lattice which will provide a coupling between spatial, temporal, and velocity discretization.

Consider the grid point centered at (x_o, y_o) shown in *Figure 2.1*. To approximate an integral of the form given equations (A.3) and (A.4) of Appendix A we may write for example:

$$\int f d\xi \approx \sum_i w_i f_i \quad (2.1)$$

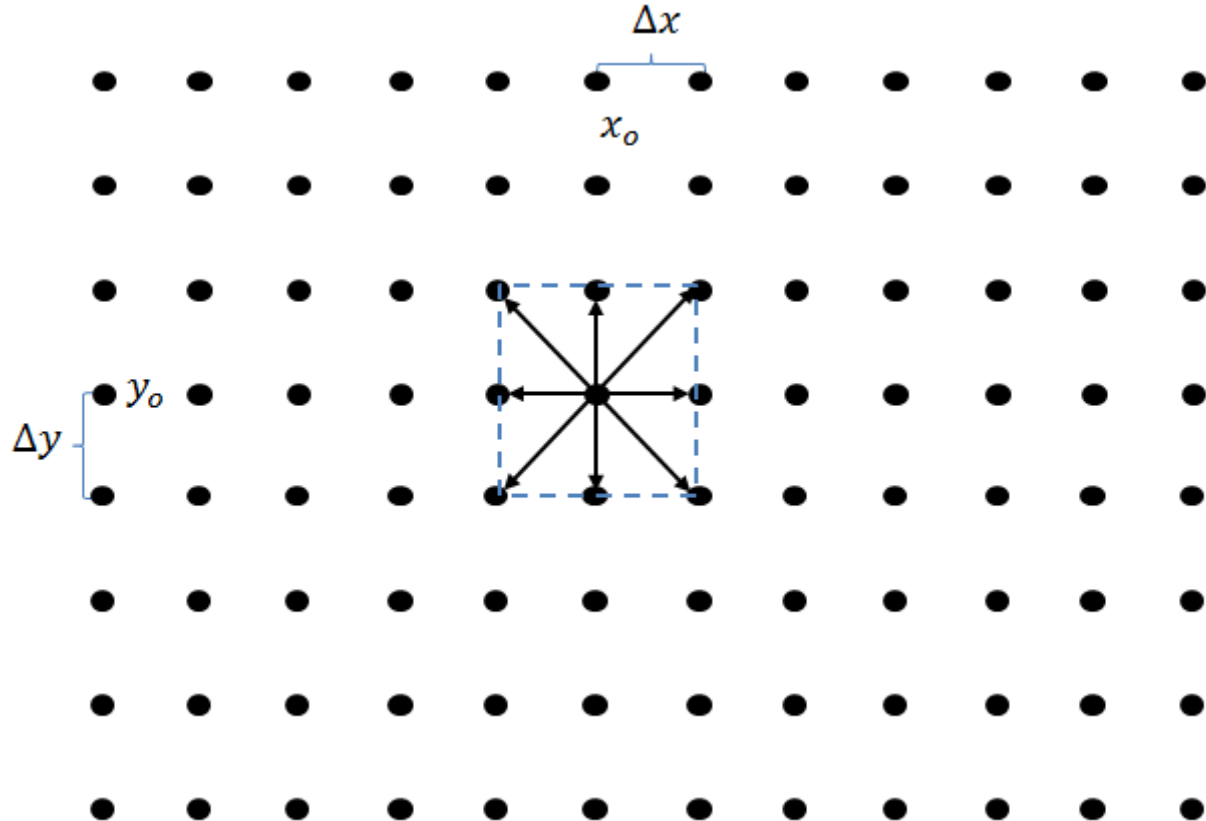


Figure 2.1: Discretized Simulation Domain.

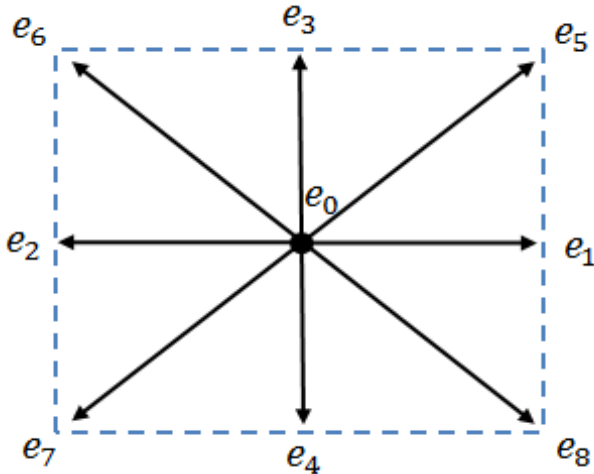


Figure 2.2: D2Q9 Lattice.

Equation (2.1) is a general expression for quadrature. That is, a definite integral of some function f over a continuous range of velocities can be approximated by a weighted sum of that function evaluated at a finite number of those velocities. The concept of a “lattice” addresses the issue of establishing which velocities should be used to evaluate the pdf for the purpose of quadrature. One example of such a lattice is the D2Q9 lattice shown in *Figure 2.2*. Here, 2 stands for the spatial dimension and 9 stands for the number of velocity directions. Suppose we focus on evaluating the integral at one location and one instance in time. Then, using the D2Q9 lattice, it suffices to know the value of the pdf for 9 values of molecular velocity to evaluate a moment integral. The reader will note the discrete velocities are labeled e_{0-8} , where e_0 is the zero vector and e_{1-8} point to neighboring nodes. Locally, these velocities may be written in a Cartesian form viz.:

$$e_{0-8} = \left\{ \begin{bmatrix} 0 \\ 0 \end{bmatrix}, \begin{bmatrix} 1 \\ 0 \end{bmatrix}, \begin{bmatrix} -1 \\ 0 \end{bmatrix}, \begin{bmatrix} 0 \\ 1 \end{bmatrix}, \begin{bmatrix} 0 \\ -1 \end{bmatrix}, \begin{bmatrix} 1 \\ 1 \end{bmatrix}, \begin{bmatrix} -1 \\ 1 \end{bmatrix}, \begin{bmatrix} -1 \\ -1 \end{bmatrix}, \begin{bmatrix} 1 \\ -1 \end{bmatrix} \right\} \quad (2.2)$$

The choice of velocity vectors used to evaluate the quadrature is not unique in the sense that other lattices are possible as addressed in [62]. What is unique is the fact that each velocity vector chosen must extend the entire distance from its origin to a neighboring node². This necessity is made clear by considering the following example. Suppose the pdf is known along each velocity vector in the lattice at one point in time. What will be the local value of the pdf at the next instance in time? Before answering this question, we recall the continuous Boltzmann equation where we have left off the forcing term for simplicity and incorporated the BGK-approximation:

$$\frac{\partial f}{\partial t} + \xi \cdot \nabla f = -\frac{f-f^{eq}}{\tau} \quad (2.3)$$

We note again that the left hand side takes the form of a convective derivative, but is not a material derivative because the molecular velocity ξ is not known at the macroscopic scale and is therefore not capable of transporting material. This distinction is subtle but important. Note that if the pdf is the equilibrium distribution, that is $f = f^{eq}$, then (2.3) is an advection equation. Another interpretation of the previous statement is that while collisions between molecules will still exist at the molecular scale, the net effect of collisions does not change the particle distribution function.

Suppose we work with the analogy that the pdf is advected with some molecular velocity. The lattice then, is a rule for advecting the pdf. In constructing a lattice with 9 directions, we have restricted the pdf to be advected in one of 9 directions. Lattice Boltzmann is then understood as a procedure to advect the pdf along discrete vectors at each time step. The process

² In some diagrams, we use different arrow lengths. Our convention is that small arrows will be used when information is local, such as the f_i -component of a pdf in the i^{th} -direction (e_i) at one node will have a small arrow to emphasize its direction and that it is a local quantity. Large arrows will be used to emphasize transport of information (typically of f_i along direction e_i from one node to a neighboring node).

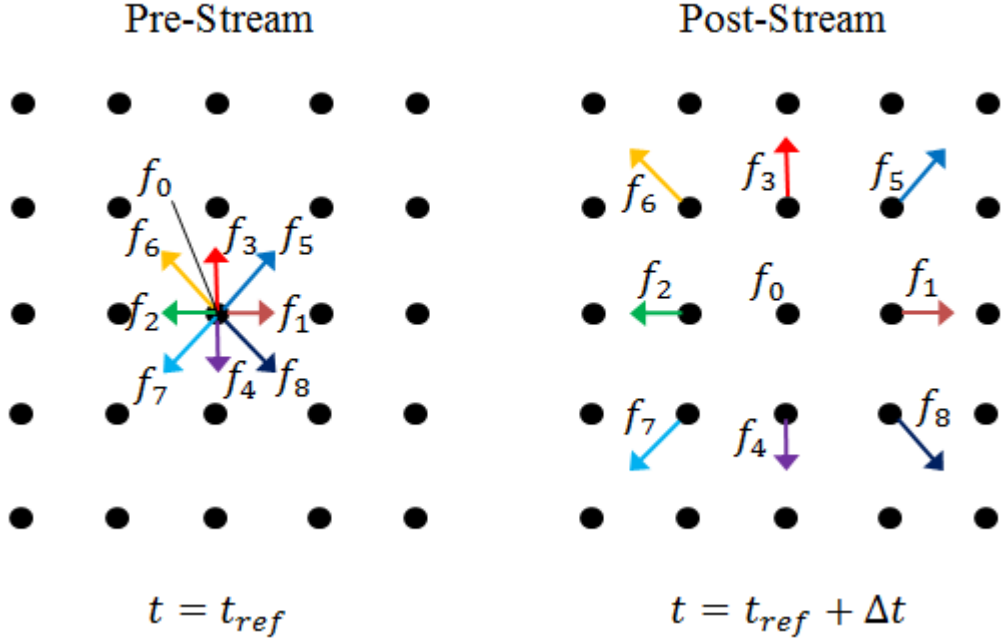


Figure 2.3: Pictorial representation of the streaming process.

of advection is called “streaming.” The vectors therefore must extend the entire distance from the origin node to a neighbor since each portion of the pdf must be advected completely during a time step. In other words, streaming is the process where each portion of the pdf is advected to nearby neighbors. By considering a finite number of directions, 9 in this case, we assume that the portion of the pdf advected in the e_i direction contains many molecules all with the instantaneous characteristic velocity direction e_i . The process of streaming is depicted in *Figure 2.3*. Assuming the 9 components of the pdf are known at one time step, the process of streaming takes the f_i component of the pdf and advects it to the neighboring node in the e_i direction. Note that no arrow is drawn for component f_0 since this portion of the pdf is streamed along the e_0 direction. In other words, this portion of the pdf maps to the origin node at every time step. The process of

streaming is completed in parallel for lattices in the domain. Once streaming is completed, a new set of pdf components will be present at each lattice corresponding to those that arrived from the neighboring nodes³. If the pdf were in equilibrium, the process of streaming would be carried out indefinitely with no changes to the pdf at any spatial location for all time. In other words, every pdf component streamed away from a given lattice would be replaced by an identical component streamed to the same lattice. Suppose though that the pdf is not in equilibrium or there is a net body force present at a spatial location. Then the right hand side of equation (2.3) is non-zero. Then the pdf components cannot simply be advected at each time step, but must be changed at each time step by the local net body force and net result of collisions. The process of changing

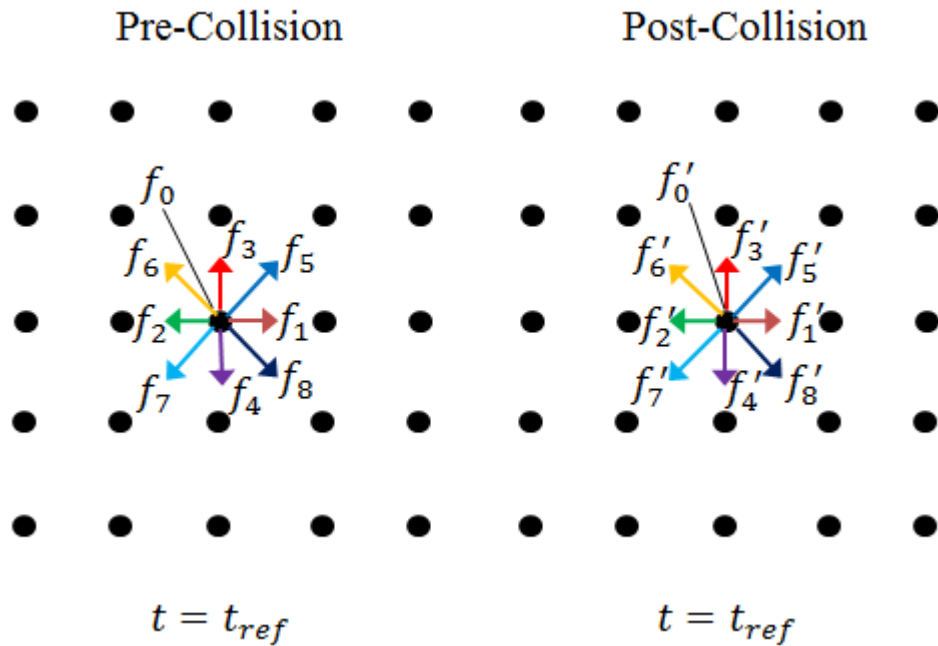


Figure 2.4: Pictorial representation of the collision process.

³ It is now apparent why the convective derivative cannot be called a material derivative. While the discrete molecular velocities e_i have transported portions of the pdf f_i , we have already assumed that the smallest piece of measurable material at a point is the entire pdf itself. Therefore, while f_i may ostensibly exist on a scale comparable to the pdf itself, they nonetheless must exist on a scale smaller than a point and therefore cannot be called material.

pdf components as a net result of collisions or a net body force is collectively referred to as “collision.” The process of collision is shown in *Figure 2.4*. With respect to implementing an LBM algorithm, note that the process of collision is local with respect to each lattice and can therefore be executed in parallel. In other words, the process of collision alters pdf components at each lattice independent of the other lattices. This process changes component f_i at lattice j say, to component f'_i at lattice j. Because the process of collision often involves calculation of body forces or other quantities that depend on macroscopic fluid properties like density and velocity, there is typically an intermediate step between streaming and collision where intermediate quantities are computed. Once the local equilibrium distribution and body forces are computed, the collision phase can be executed yielding a new set of pdf components at each lattice. The resulting pdf components can then be streamed to neighboring lattices. A general LBM algorithm can now be summarized in *Figure 2.5*. Distribution functions are initialized to their equilibrium value based on the initial macroscopic fluid properties (density and velocity) at each node. With the pdfs initialized, the algorithm commences with alternating collision and streaming routines with macroscopic quantities calculated at each time step for the purpose of determining the equilibrium distribution and forcing terms. We have implemented three multiphase LBM algorithms with their respective details found in sections 2.2.-2.4.

Finally, we briefly discuss the method of implementing boundary conditions into the LBM algorithm. Because the incorporation of boundary conditions in LBM is dependent on the particular LBM algorithm, a boundary conditions routine has been purposely left off the flowchart shown in *Figure 2.5*. Flowcharts which include more details including how boundary conditions fit into the sequence of steps in our adopted LBM algorithms are found in section 2.6.

A discussion of several LBM boundary condition strategies is found in [17]. In our LBM algorithms, we have implemented both “ghost-fluid” [11] and “bounce-back” [50] boundary conditions. These implementations were chosen because of their relative ease of implementation without sacrificing order of accuracy.

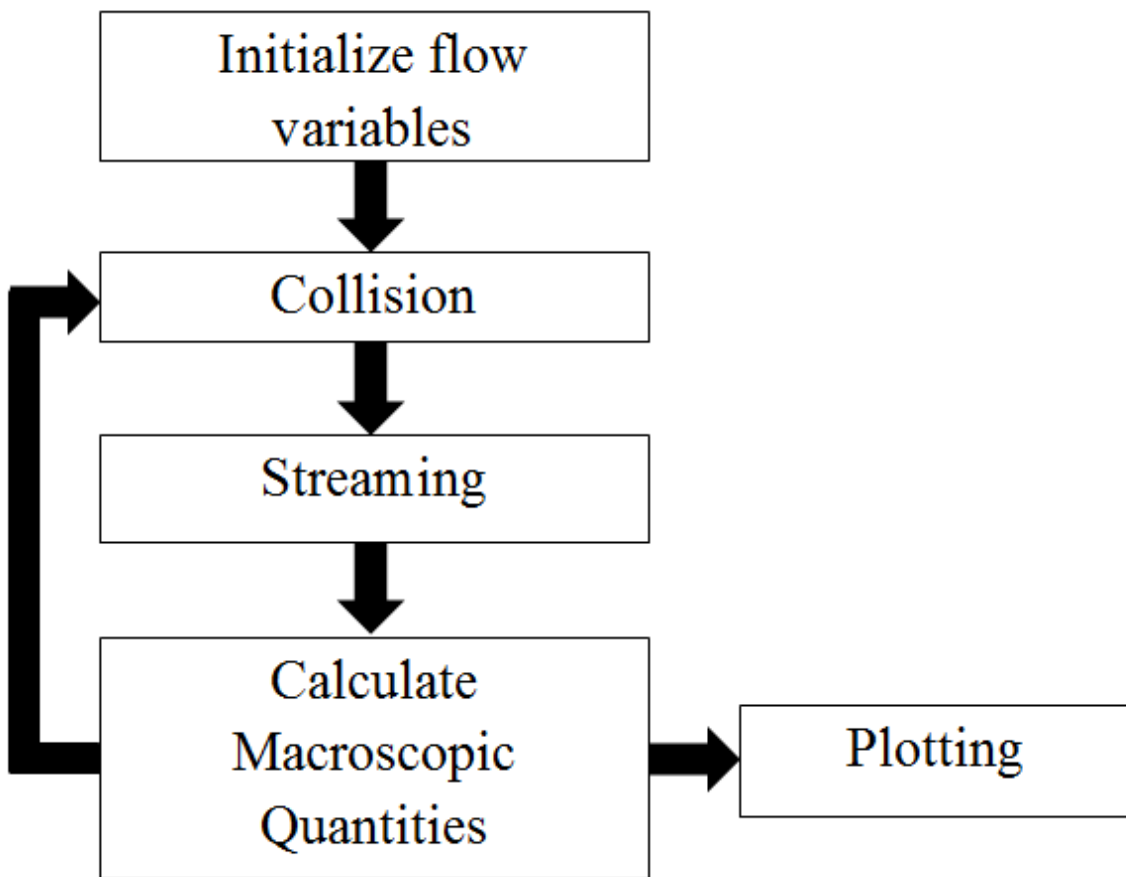


Figure 2.5: Flowchart of typical LBM Algorithm.

Beginning with the “ghost-fluid” method, we must define two types of points. Interior points are those points on the interior of a solution domain. Ghost-fluid points are those points exterior to the solution domain. The boundary of the domain then does not fall on any grid points but rather exists some distance between interior and ghost points as shown in *Figure 2.6*. The

process of streaming and collision and is carried out exclusively on interior nodes. The ghost nodes are used to construct pdfs exterior to the domain that imply a specified boundary condition at the boundary of the domain. For example, suppose we seek to impose a Dirichlet or prescribed boundary condition on the velocity, as would be the case to satisfy a no-slip, no-penetration condition. Suppose in addition that the velocity at the interior node adjacent to the boundary is u_i . What should be the value of velocity at the ghost node u_g , to imply a boundary velocity of u_w ? Assuming the boundary falls half-way between the interior and ghost node, and that the velocity varies linearly from one grid point to the next, the boundary velocity is simply the arithmetic mean of the interior and ghost velocities viz.:

$$u_w \approx \frac{u_i + u_g}{2} \rightarrow u_g = 2u_w - u_i \quad (2.4)$$

To apply a Neumann condition, we could use a central-difference formula and write for example:

$$\left. \frac{\partial u}{\partial y} \right|_{y=y_w} \approx \frac{u_i - u_g}{2\Delta y} = 0 \rightarrow u_g = u_i \quad (2.5)$$

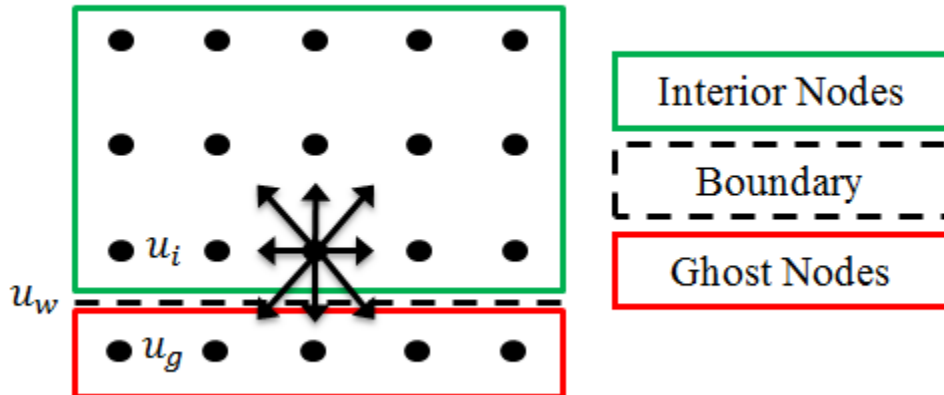


Figure 2.6: Diagram of Ghost-Fluid boundary condition.

Similar expressions can be written for pressure and density boundary conditions. Once the ghost value is computed, it only remains to calculate the pdf at each ghost point, the components of

which will be streamed to interior points by the same rule depicted in *Figure 2.6*. If the pdf at interior points were in equilibrium, then it would be reasonable to assume the correct pdf at the ghost nodes would be the equilibrium distribution given in equation (A.5) of Appendix A, with macroscopic velocity u_g . This would imply an equilibrium pdf at the boundary with associated macroscopic velocity of u_w . However, the pdf at the interior node is generally not in equilibrium. Even for non-turbulent multiphase flows, the spatial variation in fluid properties gives rise to unsteady velocity fields. In other words, the pdf at one spatial location may change with time even for low Reynolds number flows. Therefore, the pdf at the interior node adjacent to the boundary will, in general, will be made up of two components, an equilibrium portion and a non-equilibrium portion.

The pdf at an interior lattice⁴, or a ghost for that matter, can therefore be written:

$$f_i = f_i^{eq} + (f_i - f_i^{eq}) = f_i^{eq} + f_i^{neq} \quad (2.6)$$

Here, f_i^{neq} is read as the non-equilibrium component of the pdf at a given lattice, in the e_i direction. Taking the equilibrium distribution at the ghost as known using a discrete relationship analogous to (A.5) in Appendix A with associated macroscopic velocity u_g , the final task is to determine f_i^{neq} at each ghost node. We employ a Neumann condition on the non-equilibrium component of the pdf and write:

$$(f_i^{neq})_{ghost} = (f_i - f_i^{eq})_{interior} \quad (2.7)$$

Which yields:

$$(f_i)_{ghost} = f_i^{eq}(u_g) + (f_i^{neq})_{ghost} \quad (2.8)$$

⁴ Here we are being imprecise by using the term grid point or node interchangeably with lattice. Note that distinction is often not relevant, but that in some contexts, the term lattice is preferred when considering for example, the pdf, since at any given point, the pdf will have several components corresponding to the lattice or discrete molecular velocity directions. Lattice is therefore typically used in place of node when we wish to emphasize the structure of the pdf.

The assumption here is that the pdf at the boundary is not in equilibrium. However, by linear interpolation, it will have the same non-equilibrium form as that at the adjacent interior and ghost nodes with associated macroscopic velocities of u_i and u_g , respectively. Hence, the boundary pdf, while not in equilibrium, will have an implied macroscopic velocity, associated with its pdf of u_w . Note that this method of extrapolating the non-equilibrium component of the pdf is valid whether a Dirichlet or Neumann condition is imposed on the velocity since in either case the implied velocity at the boundary will be u_w . The ghost-fluid technique ensures second-order accuracy of the boundary condition [11]. This procedure was presented in the context of a simple Cartesian boundary, although the extension to boundaries defined by complex shapes can also be treated by the ghost-fluid method via multi-linear interpolation [11].

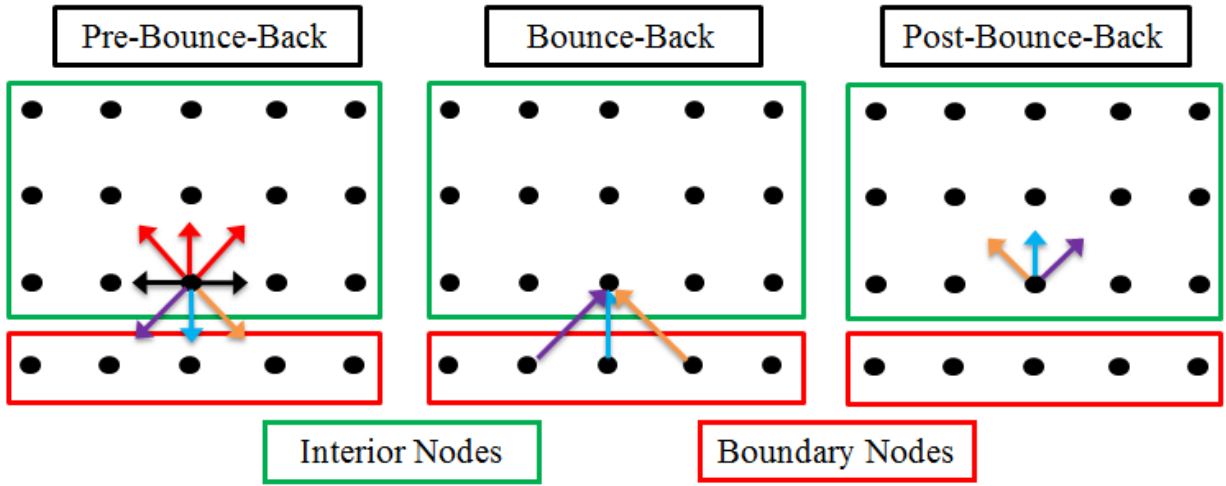


Figure 2.7: Bounce-back boundary condition.

We have also explored the implementation of a “bounce-back” boundary condition [50] to enforce no-slip, no-penetration conditions at solid boundaries. The bounce-back condition enforces Dirichlet conditions by tracking each component of the pdf that would be streamed out of the domain during a given time step. Consider *Figure 2.7*. After the collision step, all

components of the pdf at each interior node are known. The streaming phase is entered and new pdf components will be streamed to neighboring interior lattices. However, the pdf components denoted by the red arrows in *Figure 2.7* will be unknown after streaming is completed since there are no interior nodes to replace these components. To mitigate this, we note which components of the pdf at interior lattices adjacent to the boundary actually leave the interior of the domain so that they can be replaced. After streaming on interior nodes is complete, we note three components originating at an interior lattice neighboring the domain boundary (the purple, blue, and orange) will leave the interior of the domain. We therefore apply the bounce-back condition and reflect *these* pdf components. If we take the purple component for example which is in the e_7 direction, bounce-back takes the magnitude of this component, and replaces the e_5 component at the boundary node, with this value. The same procedure is done for each of the pdf components leaving the interior. Once bounce-back has been applied, a second streaming phase is entered, only for the boundary nodes, so that new pdf components calculated on the boundary nodes can be streamed to the interior. This post-streaming process replaces the previously unknown red pdf components in *Figure 2.7*. The bounce-back method is useful because it ensures mass conservation in the simulation. That is, each piece of mass streamed out of the domain is replaced once bounce-back has been applied. In comparison, the ghost-fluid method will have a small but finite amount of mass lost at each time step as we have observed. In addition, the bounce-back condition ensures no-slip, and no penetration is satisfied to 2nd-order of accuracy [50]. The disadvantage of bounce-back is in the application of non-wall boundary conditions, e.g. Neumann velocity boundary conditions and pressure boundary conditions at the entrance and exit of open domains for instance, however some authors [50] have extended bounce-back to these type of boundary conditions. For ease of implementation, the ghost-fluid

method was adopted for most simulations and yielded satisfactory enforcement of given boundary conditions. When presenting results in chapters 4, 5, and 6, we will note which boundary conditions were employed, as well as in the implementation of each LBM algorithm given in sections 2.6.

With the requisite theory presented, we can now introduce the LBM algorithms we have implemented in the next sections. Note that the previous discussion was in the context of a single pdf (or single fluid system). Because the algorithms discussed next will be for multiphase flows, we will be careful to note the additional considerations necessary for modeling such systems.

2.2 Shan and Chen Method

We have implemented the multiphase Lattice Boltzmann algorithm originally formulated by Shan and Chen [75, 74]. We follow a similar notation as that given by Wang et al. [68]. In the Shan and Chen (S-C) procedure, a set of n-discretized Boltzmann equations is solved, one for each of n-fluids present in the system being simulated.

The discretized governing equation for the n^{th} -pdf⁵ is given in (2.9):

$$f_i^n(x + e_i t, t + \Delta t) = f_i^n(x, t) - \frac{\Delta t}{\tau_n} \left(f_i^n(x, t) - f_i^{eq^n}(x, t) \right) \quad (2.9)$$

where f_i^n is the single particle distribution function of the n^{th} fluid component⁶ in the i^{th} direction. The collision term in the lattice Boltzmann equation is discretized using the BGK-approximation [47], with single relaxation time of each fluid component given by τ_n . Assuming low Mach number, the equilibrium distribution function of the n^{th} fluid component, $f_i^{eq^n}$ is given by the Maxwell-Boltzmann distribution [55]:

$$f_i^{eq^n}(x, t) = w_i \rho_n \left[1 + 3 \frac{(e_i \cdot u_n^{eq})}{c^2} + \frac{9}{2} \frac{(e_i \cdot u_n^{eq})^2}{c^4} - \frac{3}{2} \frac{(u_n^{eq})^2}{c^2} \right] \quad (2.10)$$

⁵ It is natural to wonder what it means for multiple pdfs (or fluids for that matter) to be defined at the same point. Invoking the Continuum hypothesis, we recall that at any given spatial location (much smaller than the fluid-element scale), there will likely be no matter present, but rather in the neighborhood of that location. With this understanding, there is no special treatment needed to define additional pdfs at a point than the original assumptions incorporated in defining a single pdf. As far as which fluid is present at any given location, ambiguity will only be present in the neighborhood of the interface between two or more fluid components. At an interfacial location, the concept of a single fluid becomes less meaningful. The models employed however attempt to capture the measurable dynamics, that is, if two fluids are “present” at one point (fluid-element size), the majority fluid by mass should have the largest contribution to the dynamics at and in the neighborhood of that point.

⁶ The term component is used purposefully here to emphasize the modeled fluids are assumed distinct and immiscible, e.g. water and oil, or water and air. However, phase change within a component, viz. from water to water vapor say, will still be possible according to an assumed equation of state. This point will be addressed in more detail in the subsequent discussion.

Here, the lattice speed c , is taken to be unity, i.e. $c = \Delta x / \Delta t = 1$. Velocity space has been discretized using the D2Q9 lattice where the e_i directions are given by:

$$e_{0-8} = \left\{ \begin{bmatrix} 0 \\ 0 \end{bmatrix}, \begin{bmatrix} 1 \\ 0 \end{bmatrix}, \begin{bmatrix} -1 \\ 0 \end{bmatrix}, \begin{bmatrix} 0 \\ 1 \end{bmatrix}, \begin{bmatrix} 0 \\ -1 \end{bmatrix}, \begin{bmatrix} 1 \\ 1 \end{bmatrix}, \begin{bmatrix} -1 \\ 1 \end{bmatrix}, \begin{bmatrix} -1 \\ -1 \end{bmatrix}, \begin{bmatrix} 1 \\ -1 \end{bmatrix} \right\} \quad (2.11)$$

The corresponding quadrature weights, w_i for the D2Q9 stencil are:

$$w_i = \begin{cases} \frac{4}{9}; & i = 0 \\ \frac{1}{9}; & i = 1 - 4 \\ \frac{1}{36}; & i = 5 - 8 \end{cases} \quad (2.12)$$

$\rho_n(x, t)$ is the local fluid density of the n^{th} fluid component at location x , at time t . The density of the n^{th} component at each point is calculated by the discrete analog to equation (A.3) in Appendix A:

$$\rho_n(x, t) = \sum_i f_i^n(x, t) \quad (2.13)$$

The total density of the system at any point is then:

$$\rho(x, t) = \sum_n \rho_n(x, t) \quad (2.14)$$

Note that the lattice Boltzmann equation (2.9) given in the S-C procedure has no explicit forcing term. The forcing term rather, is introduced implicitly to the lattice Boltzmann equation via the definition of the equilibrium velocity of the n^{th} component:

$$u_n^{eq} = u_{mix} + \frac{\tau_n}{\rho_n} F_n \quad (2.15)$$

Where F_n is the net force on the n^{th} component and the mixture velocity, u_{mix} ⁷ is defined as:

$$u_{mix} = \frac{\sum_n \rho_n u_n / \tau_n}{\sum_n \rho_n / \tau_n} \quad (2.16)$$

The forcing term requires a more detailed discussion. F_n is the total contribution of forces acting on the n^{th} component at a spatial location and can be written as the sum of two terms:

$$F_n = F_{inter}^n + F_{body}^n \quad (2.17)$$

Here, F_{body}^n is the total body force which may include gravity and F_{inter}^n is the net measurable force accounting for intermolecular effects (which occur solely on a sub-continuum scale) that act on spatial variations in the pdf. Wang and Liu [68], and Gupta and Kumar [2] further decompose F_{inter}^n into two components:

$$F_{inter}^n = F_{fluid}^n + F_{solid}^n \quad (2.18)$$

⁷ Several velocities are defined in this algorithm which do not have a clear physical analog. Physical arguments are made in [74] as to the origin of these definitions, although these rationales will not be presented here. As in many LBM algorithms, Shan and Chen will make the argument that the end justifies the means, that is the assumptions made in their algorithm provide a reasonable approximation to the flow equations. This discussion to follow.

Here, F_{fluid}^n is the net intermolecular force on the n^{th} fluid component at location x due to spatial variations in itself or due to the presence of another fluid component in the neighborhood of x . F_{solid}^n is the net intermolecular force on the n^{th} fluid component due the presence of a solid boundary in the neighborhood of that component. Using kinetic theory arguments, Shan and Chen [75] originally proposed that the fluid intermolecular force could be written as the gradient of a scalar ψ , referred to as the interaction potential. Assuming that intermolecular forces at any point are weak except in the neighborhood of that point [24], it may be reasonable to only consider nearest neighbor interactions.⁸ Under this assumption, Shan and Chen [75] proposed a discretization of F_{fluid}^n of the form:

$$F_{fluid}^n = -\psi_n(x) \sum_n G_{n\bar{n}} \sum_i w_i \psi_{\bar{n}}(x + e_i) e_i \quad (2.19)$$

Here, ψ_n is read as the interaction potential of the n^{th} component, \bar{n} refers to other components, w_i are the quadrature weightings corresponding to a given lattice, (2.12) for the D2Q9 lattice, and $G_{n\bar{n}}$ represents the strength of interaction between like, and un-like fluid components. Taking for example, a multiphase system containing two fluid components, $G_{n\bar{n}}$ can be written as:

$$G_{n\bar{n}} = \begin{cases} G_{11} \\ G_{21} \\ G_{12} \\ G_{22} \end{cases} \quad (2.20)$$

⁸ Other authors [73] have proposed higher order discretizations that take into account both nearest, and next-nearest neighbor interactions, for example.

Here, when the interaction strength G has a repeated subscript, a non-zero value of G_{11} for example will denote self-interaction where as a non-zero value of G_{12} say, will denote interaction between different components. G_{12} is read as the magnitude of the interaction between components 1 and 2, where the net force is on component 1, and the net force is due to the presence of component 2. Note, to ensure global momentum conservation, $G_{12} = G_{21}$ or more generally, $G_{n\bar{n}} = G_{\bar{n}n}$ [75]. Similarly, the fluid solid force is written as [68]:

$$F_{solid}^n = -\psi_n(x) \sum_n G_{nS} w_i s(x + e_i) e_i \quad (2.21)$$

Here, G_{nS} is the magnitude of the interaction force on the n^{th} fluid component due to a solid boundary, and $s(x + e_i)$ is unity if $x + e_i$ is not an interior point, and zero otherwise. Whether fluid-fluid or fluid-solid interaction is considered, negative values of G indicate an attractive force and positive values indicate a repelling force. Note that the definition of an interaction potential in this context means that other observable properties such as interfacial tension and contact angle, for instance, are each defined implicitly by the relative strengths of interaction, and by the definition of the interaction potential itself. Therefore, in principle, variation of interaction strengths allows arbitrary control⁹ over these properties, but not direct tuning.

Thus far, there has been no discussion of pressure. The treatment of pressure in LBM requires more attention than can be given in this section. However, the definition of an interaction potential provides a good segue. LBM is fundamentally a compressible scheme. That is, the local pressure is coupled to the density at any point via an equation of state (EOS). In the absence of intermolecular interaction, the fluid behaves as an ideal gas, that is, the equation of

⁹ Subject to the scheme's stability. Very large forces can destabilize the numerical scheme.

state is simply that pressure is directly proportional to density. Therefore, the introduction of interaction potentials implies a non-ideal component in the system's EOS [75]. The implied EOS takes the form [68]:

$$p(x, t) = \underbrace{c_s^2 \sum_n \rho_n(x, t)}_{\text{Ideal}} + \underbrace{\frac{1}{2} c_s^2 \sum_{n\bar{n}} G_{n\bar{n}} \psi_n(x, t) \psi_{\bar{n}}(x, t)}_{\text{Non-Ideal}} \quad (2.22)$$

Where c_s is the sound speed and typically defined such that $c_s^2 = RT = 1/3$. The definition of interaction potentials determine what form the non-ideal term in the EOS will take. Shan and Chen [75] originally proposed an interaction potential of the form:

$$\psi_n(x, t) = \rho_{no} \left[1 - \exp \left(-\frac{\rho_n(x, t)}{\rho_{no}} \right) \right] \quad (2.23)$$

Here, ρ_{no} is a constant equal to the initial density of the n^{th} component, assumed to be spatially uniform wherever the n^{th} component is initially defined in the domain. Other equations of state have been proposed; for a thorough account, see [49].

The EOS may serve two purposes. Taking a one-component system for example, say water, if an appropriate interaction potential was implemented that implied the equation of state of water (as could be determined experimentally), then in principle it would be possible to model the phase change between liquid water and water vapor. In a two component system then, say oil and water, there could be interaction between two fluid components one of which could change its thermodynamics phase. The second purpose is to model a fluid system in which there exists a large difference in the density of the two fluids. Consider for example first, what would happen

if we had the fluid system considered in *Figure 2.8*. We initialize the velocity to be zero everywhere and consider this system without the effect of gravity. What would happen? If we assume the two fluids to be non-interacting ideal gases, then over time we would see a diffusion of the blue fluid to the lower part of the box, and diffusion of the red fluid to the upper part of the box. This diffusion occurs not because of gradients in velocity (the fluid velocity everywhere is initially quiescent) but there is initially a concentration gradient for each of the fluids which tends to smooth out over time. After much time, there will be a uniform concentration of both

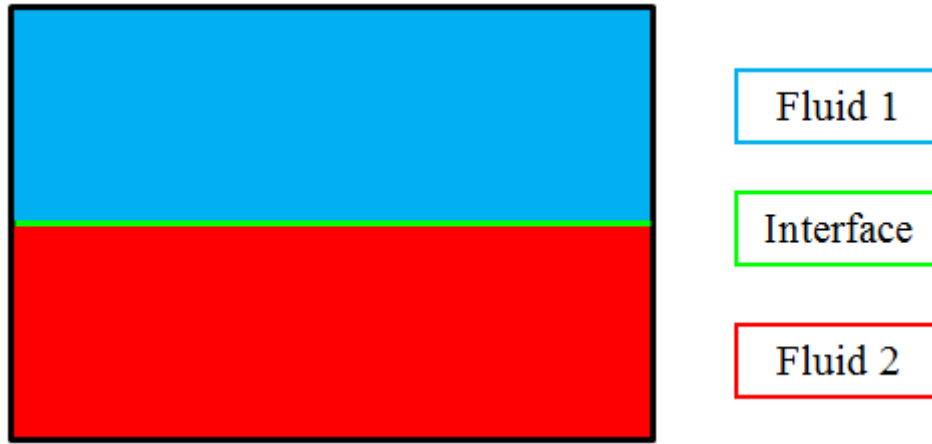


Figure 2.8: System of two stratified fluids.

blue and red fluids, everywhere in the domain. There is nothing wrong with this possibility from the LBM standpoint. However, suppose we wish for these two fluid components to remain immiscible. Then it is necessary to introduce forces that resist the mutual diffusion of these components. To limit the diffusion, we could define an interaction force between fluids 1 and 2 such that the preference towards diffusion of one component is inhibited by the presence of another. This means for example that diffusion of fluid 1 to the bottom region is being inhibited because fluid 2 is occupying that space. Alternatively, we could limit the diffusion of fluid 1 via

a self-interaction force, that is a negative value of G_{11} . That is, there must exist a large enough positive value of G_{12} or a large enough negative value of G_{11} such that fluid 1 remains quiescent. The same can be said for fluid 2. In practice, the relative miscibility of the components is determined by tuning both cross-interaction G values (G_{12}) and self-interaction G-values (G_{11} and G_{22}). In principle, these parameters can be tuned arbitrarily to yield desired macroscopic properties (interfacial tension for instance). Cross interaction typically has a finite value (positive indicates repulsion of un-like components and negative indicates attraction of un-like components) which is problem dependent. This maximum corresponds to the calculation's stability boundary, above which the calculation will be unstable.

Now we may consider the meaning of the sign of the self-interaction term. Considering for example a one component fluid system where the fluid density is not spatially uniform. Assuming the volume of the system domain is fixed, will the system retain its spatial variation in density? Consider the general non-ideal gas EOS (2.22). For strictly positive values of G, the pressure will increase monotonically with density since the non-ideal term will be positive-definite. In a system where there initially exists spatial non-uniformities in the density, the tendency will be towards an equilibrium non-varying spatially constant density which implies a constant pressure for the system. Therefore, a positive value of self-interaction will tend to eliminate spatial variation in the fluid density.

Suppose now the self-interaction magnitude is taken to be strictly less than zero. For some critical value of G, the pressure curve will have an inflection point. This value of G is analogous to the critical temperature of the fluid, so that the location of the inflection point in a state-diagram is termed the critical point. For negative values of G, greater in magnitude than G_c , the pressure will no longer vary monotonically with density but rather will exhibit a trend similar

to that depicted in *Figure 2.9*¹⁰. Here, $V \equiv 1/\rho$ is the specific volume. Note that for $G < G_c$, or analogously, temperature $T < T_c$, there will exist in general three possible values of density for a

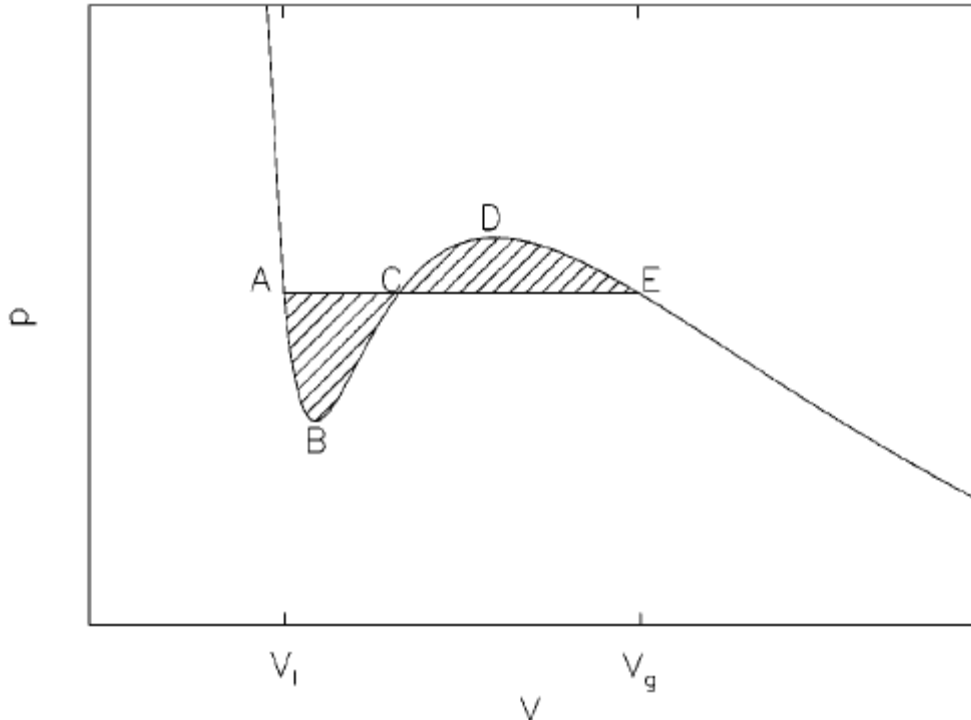


Figure 2.9: Hypothetical EOS for $T < T_c$, reproduced from [71].

a given pressure. These possible values of density correspond to states A, C, and E in *Figure 2.9*. However, position C corresponds to an unstable state where pressure increases (decreases) with volume (density). Physically, this state is not favored. Therefore, the system will tend toward states A and E which lie on stable branches of the fluid's EOS [71, 75].

We may now observe what happens to a system in which the density is initially spatially non-uniform and G is below its critical value. Consider *Figure 2.10*. The initial density is prescribed a 1% perturbation about a value of 1.00 as shown in *Figure 2.10a*. As time progresses in *Figure 2.10b-d*, we observe that phases of like density attract each other and we also observe a

¹⁰ The interaction potential must remain bounded above by $\sim \sqrt{\rho}$ to ensure the pressure tends toward infinity as $\rho \rightarrow \infty$, $\forall G$ [75].

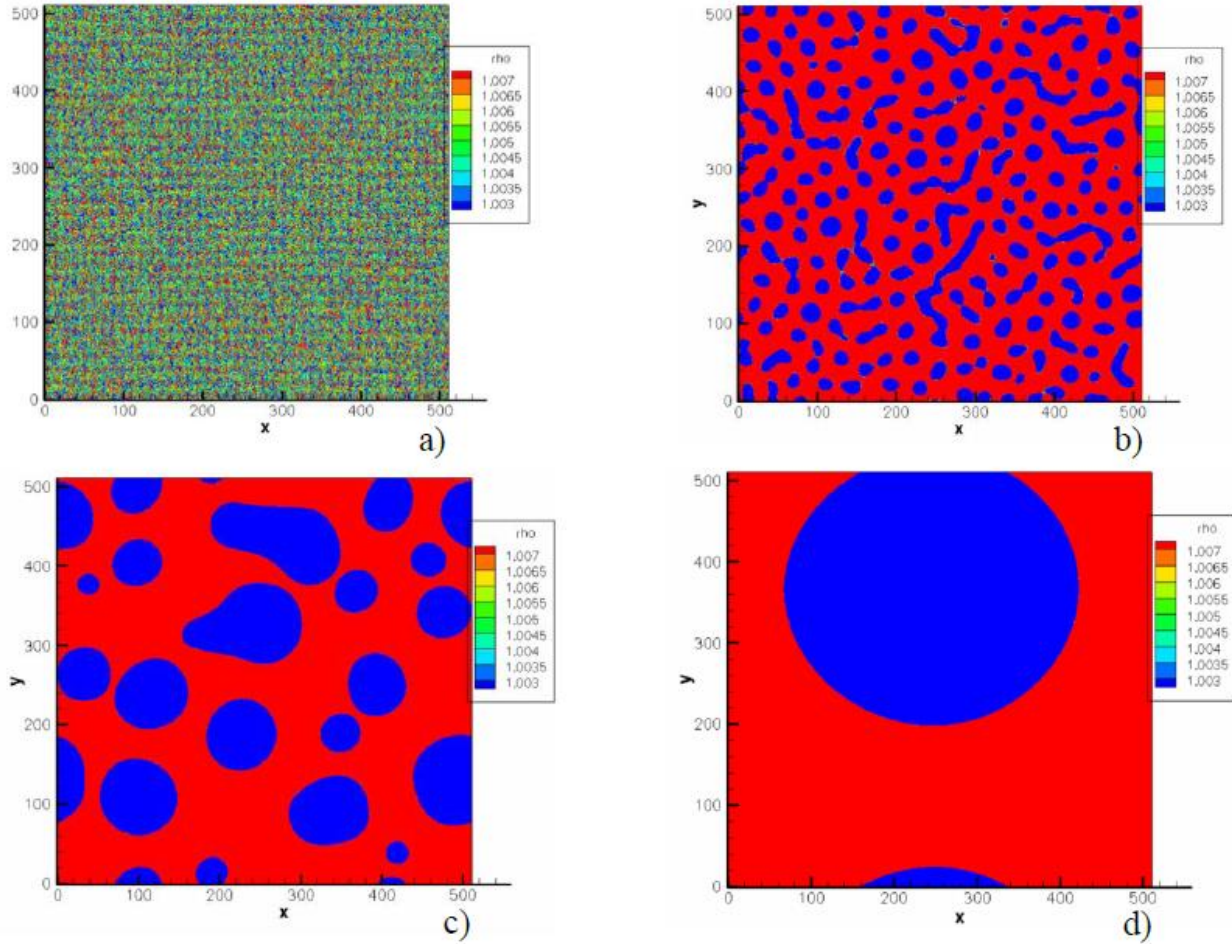


Figure 2.10: Phase Separation of a 1 component fluid. Initial density field random with a prescribed 1% perturbation about a density value of 1.00.

transition from a state of many densities to a state where there exists only two densities (corresponding to red and blue contours). As a consequence, given an EOS, we could simulate a high density ratio problem involving a liquid and a gas without the need to incorporate large interaction forces to segregate components, as would be necessary for a multiple component system not linked by an EOS. That is, several calculations we have performed suggest the density ratio that can be achieved in a multiple component system is typically order 10 or less¹¹, while

¹¹ Several authors, [79] for example claim much higher density ratios for multiple component systems. Some authors [65, 64, 28] have developed modified LBM procedures to achieve higher density ratios, although it is unclear whether the stability at high density ratio comes at the price of other essential physics. Nevertheless, the density ratio limitation puts sharp constraints on the applicability of LBM to simulate a range of practical systems. Our experience gives us the most confidence in low density ratio (< 5) multiple component liquid-liquid flows.

the density ratio we can achieve for a single component system of two phases may reach O(500) with the incorporation of an appropriate equation of state¹². However, in the single component case, surface tension is a result of the particular EOS and cannot be tuned once the EOS is set, while in the multiple component case, surface tension may be tuned by varying both self-interaction and cross-interaction magnitudes, and in principle by the definition of the interaction potential or the EOS itself. In either case, the surface tension in the S-C method is implied by Laplace's Law [75], which for a symmetric bubble takes the form:

$$\frac{\sigma}{R} = p_{in} - p_{out} \quad (2.24)$$

Here, σ is the surface or interfacial tension, R is the local radius of curvature, and p_{in} and p_{out} refer to the pressure on the in and outside of the bubble, respectively. To imply an EOS of a given form, we note the interaction potential can be written as (2.25) [49]:

$$\psi(\rho) = \sqrt{\frac{2(p(\rho) - c_s^2 \rho)}{c_s^2 G}} \quad (2.25)$$

Here, $p(\rho)$ is the EOS of a single fluid component which may be obtained theoretically or experimentally.

It is natural to wonder whether the S-C LBM scheme is a suitable model for a fluid system, in other words, is the discrete solution to the LBM equations equivalent to a discrete solution to the Navier-Stokes and continuity equations? As noted in [75] and shown in [74, 56]

¹² The Carnahan-Starling EOS [41] proves to be a good choice for high density ratio single component calculations. More description regarding this EOS will be given in the next section.

using multiple-scale asymptotic expansions, the S-C scheme will in fact recover the Navier-Stokes and Continuity equations, in their compressible form to second order in Mach number. The pressure is related to the density via an EOS implied by the choice of interaction potential. The effect of compressibility is often small for low Mach numbers, however as discussed in Sections 2.4 and chapter 3, the condition of small Mach number is not always sufficient to guarantee “small” compressibility. From the analysis in [56], the relaxation time of the n^{th} component, τ_n is related to the kinematic viscosity of the n^{th} , ν_n via (2.26):

$$\nu_n = \frac{1}{3} \left(\tau_n - \frac{1}{2} \right) \quad (2.26)$$

Based on this definition, $\tau_n = \frac{1}{2}$ corresponds to an inviscid fluid. In practice, the lowest value of relaxation time at which the numerical scheme remains stable is $\tau_n \approx 0.53$. The relaxation time may exceed unity although we have observed that most authors use values of the relaxation time close to 1. It is worth noting that the definition in (2.26) may be counter-intuitive, that is, small relaxation times are associated with small viscous effects and large relaxation times are associated with highly viscous effects. One interpretation of the response time is with respect to (2.9). A large relaxation time for the n^{th} -component indicates a small collision term on the right-hand side of (2.9) for that component. That is, the net result of collision does not have a large effect on the shape of n^{th} -component pdf. (2.9) is then approximately an advection equation where pieces of the pdf are streamed and interchanged at neighboring lattices with the net result being the new pdf at each lattice site is approximately unchanged. With this interpretation, the relaxation time may be understood as the characteristic time over which the pdf of the n^{th} -component changes, that is, the characteristic time in which local fluid properties such as

density, velocity, and pressure change. In this respect, it is consistent with our expectation that a highly viscous fluid would have a large relaxation time, and therefore “observably respond” to an external stimulus (body force) over a similarly large characteristic time. For very large relaxation times, the flow scenario is consistent with viscous stresses dominating inertial stresses. In this limit, the Navier-Stokes equations would yield the steady elliptic Stokes’ equation. The solution to this low Reynolds number equation would be time-invariant. Therefore, in the limit of infinite relaxation time, the solution to (2.9) would also be time-invariant.

For completeness, we state the expression for the macroscopic fluid velocity which is consistent with the velocity definition in the Navier-Stokes equations [74]:

$$\rho(x, t)U(x, t) = \sum_n \sum_i e_i f_i^n(x, t) + \frac{1}{2} \sum_n F_n(x, t) \quad (2.27)$$

Here, $U(x, t)$ is the macroscopic fluid velocity at location x , at time t , and $\rho(x, t)$ and $F_n(x, t)$ are defined in equations (2.14) and (2.17) respectively. Note that for a two-component fluid system each with a single phase, the expression for the macroscopic fluid velocity (2.27) will be identical to that expressed in (2.16), except in the neighborhood of the interface between disparate components where interaction forces are likely to be present. The macroscopic velocity is defined by expressing the average of the momentum of each component before and after their respective collision phase. See [74] for more details.

This completes the necessary discussion of equations and theory relevant to the Shan and Chen algorithm. The He-Chen algorithm, and an extension to it, will be discussed in the next sections. Finally in section 2.6, we discuss the respective algorithms from the standpoint of implementation.

2.3 He and Chen Method

We have also implemented an LBM algorithm originally formulated by He et al. [71, 70]. The He-Chen (H-C) method tracks a set of two generalized forms of the lattice Boltzmann equation. These equations are (2.28) and (2.29):

$$f_i(x + e_i t, t + \Delta t) = f_i(x, t) - \frac{\Delta t}{\tau} (f_i(x, t) - [f_i(x, t)]_{eq}) - \frac{2\tau - 1}{2\tau} \frac{(e_i - u) \cdot \nabla \psi(\phi)}{RT} \Gamma_i(u) \cdot \Delta t \quad (2.28)$$

$$\begin{aligned} g_i(x + e_i t, t + \Delta t) &= g_i(x, t) - \frac{\Delta t}{\tau} (g(x, t) - [g_i(x, t)]_{eq}) \\ &- \frac{2\tau - 1}{2\tau} (e_i - u) \cdot [\Gamma_i(u) \cdot F_t - (\Gamma_i(u) - \Gamma_i(0)) \cdot \nabla \psi(\rho)] \cdot \Delta t \end{aligned} \quad (2.29)$$

Here, f_i and g_i are generalized distribution functions. f_i is the distribution function related to a quantity known as the index function ϕ , which is analogous to a level-set function [71]. The index may be defined such that a given value of the index corresponds to a particular fluid component:

$$\phi = \begin{cases} \text{fluid 1}, & \phi = \phi_1 \\ \text{interfacial region}, & \phi_1 < \phi < \phi_2 \\ \text{fluid 2}, & \phi = \phi_2 \end{cases} \quad (2.30)$$

It is possible to define ϕ in such a way that it can be representative of more than two fluid components, however the He-Chen algorithm was formulated to model systems with strictly two fluid components. f_i is related to ϕ , which in turn can be used to calculate the density at any location via linear interpolation. Those respective relationships are given in (2.31) and (2.32):

$$\phi = \sum_i f_i \quad (2.31)$$

$$\rho(\phi) = \rho_1 + \frac{\phi - \phi_2}{\phi_1 - \phi_2} (\rho_1 - \rho_2) \quad (2.32)$$

Similarly, the local kinematic viscosity can be written as (2.33):

$$\nu(\phi) = \nu_1 + \frac{\phi - \phi_2}{\phi_1 - \phi_2} (\nu_1 - \nu_2) \quad (2.33)$$

The relaxation time is related to the kinematic viscosity via equation (2.34):

$$\tau = \left(\tau - \frac{1}{2} \right) RT \Delta t \quad (2.34)$$

The equilibrium distribution function related to the index is given in (2.35)

$$[f_i(x, t)]_{eq} = w_i \phi \left[1 + 3(e_i \cdot u) + \frac{9}{2}(e_i \cdot u)^2 - \frac{3}{2}(u)^2 \right] \quad (2.35)$$

The form of this equilibrium pdf is similar to that used in the S-C method, however the H-C method only uses one velocity \mathbf{u} , namely the macroscopic fluid velocity at location \mathbf{x} , at time t . Note, we have implicitly taken to the lattice speed c to be unity. $\Gamma_i(u)$ in (2.28) and (2.29) is shorthand for:

$$\Gamma_i(\mathbf{u}) = [f_i(x, t)]_{eq}/\phi = w_i \left[1 + 3(e_i \cdot u) + \frac{9}{2}(e_i \cdot u)^2 - \frac{3}{2}(u)^2 \right] \quad (2.36)$$

Unlike in the S-C procedure, the local velocity and pressure are related to a second distribution function g_i according to the relationships given in (2.37) and (2.38):

$$\rho R T u = \sum_i e_i g_i + \frac{RT}{2} F_t \cdot \Delta t \quad (2.37)$$

$$p = \sum_i g_i - \frac{1}{2} u \cdot \nabla \psi(\rho) \cdot \Delta t \quad (2.38)$$

The equilibrium distribution function related to pdf g_i is (2.39):

$$[g_i(x, t)]_{eq} = w_i \left[p + \rho \left(1 + 3(e_i \cdot u) + \frac{9}{2}(e_i \cdot u)^2 - \frac{3}{2}(u)^2 \right) \right] \quad (2.39)$$

These definitions ensure both second order and spatial and temporal accuracy of the H-C scheme, assuming the boundary conditions are handled properly [71]. We have implemented two and three-dimensional versions of the H-C algorithm. We used a D2Q9 lattice for the two-dimensional code and a D3Q27 lattice for the three-dimensional code. The associated discrete molecular velocities and quadrature weightings for the D3Q27 lattice are:

e_{0-26}

$$= \left\{ \begin{bmatrix} 0 \\ 0 \\ 0 \end{bmatrix}, \begin{bmatrix} 1 \\ 0 \\ 0 \end{bmatrix}, \begin{bmatrix} -1 \\ 0 \\ 0 \end{bmatrix}, \begin{bmatrix} 0 \\ 1 \\ 0 \end{bmatrix}, \begin{bmatrix} 0 \\ -1 \\ 0 \end{bmatrix}, \begin{bmatrix} 1 \\ 1 \\ 0 \end{bmatrix}, \begin{bmatrix} -1 \\ 1 \\ 0 \end{bmatrix}, \begin{bmatrix} 1 \\ -1 \\ 0 \end{bmatrix}, \begin{bmatrix} -1 \\ -1 \\ 0 \end{bmatrix}, \begin{bmatrix} 0 \\ 0 \\ 1 \end{bmatrix}, \begin{bmatrix} 1 \\ 0 \\ 1 \end{bmatrix}, \begin{bmatrix} -1 \\ 0 \\ 1 \end{bmatrix}, \begin{bmatrix} 0 \\ 1 \\ 1 \end{bmatrix}, \begin{bmatrix} 0 \\ -1 \\ 1 \end{bmatrix}, \begin{bmatrix} 1 \\ 1 \\ 1 \end{bmatrix}, \begin{bmatrix} -1 \\ 1 \\ 1 \end{bmatrix}, \begin{bmatrix} 1 \\ -1 \\ 1 \end{bmatrix}, \begin{bmatrix} -1 \\ -1 \\ 1 \end{bmatrix} \right\} \quad (2.40)$$

$$w_i = \begin{cases} \frac{8}{27}; & i = 0 \\ \frac{2}{27}; & i = 1 - 4, 9, 18 \\ \frac{1}{54}; & i = 5 - 8, 10 - 13, 19 - 22 \\ \frac{1}{216}; & 14 - 17, 23 - 26 \end{cases} \quad (2.41)$$

Two terms in particular require further discussion, namely the forcing term F_T , and the interaction potential ψ . The forcing term takes the following form:

$$F_T = F_g + k\phi\nabla\nabla^2\phi \quad (2.42)$$

Here, F_g is the net body or gravitational force per unit volume and the second term represents the contribution of gradients in curvature of the index function to interfacial forces [72]. Other models for interfacial forces have been proposed, for example [29]. For comparison, we have incorporated the CSF [29] model into our calculations but found no discernible difference in the results of our calculations compared with results obtained with inclusion of surface tension force under the former definition given in (2.42). Zhang et al. [53] showed that κ is related to the magnitude of the interfacial tension via a surface integral equation of the form:

$$\sigma = \kappa \int \left(\frac{\partial \phi}{\partial z} \right)^2 dz = \kappa I(a) \quad (2.43)$$

The integral in (2.43) is taken along the entire interfacial surface between two components and z is taken as the direction everywhere normal to that surface. In general, this integral is problem dependent. However, as [53] notes, assuming a fixed choice for discretizing the interface between disparate components, the behavior of ϕ in the interfacial region depends solely on the choice of the equation of state. This is one of the most notable features of the H-C method. That is, the H-C method is an algorithm used to simulate two fluid components where the EOS is chosen so as to govern the dynamics, and the shape of the density profile, in the neighborhood of the interface. In principle, this could be used to simulate problems with phase-change. However as has been used by He and Chen [71] and other authors [28], we use the H-C formulation strictly for the modeling of two immiscible components as was discussed for the multiple component S-C algorithm. However, as we shall now see, the H-C formulation now allows for explicit prescription of the interfacial or surface tension.

Returning to the discussion of the surface integral in (2.43), assuming an appropriate EOS has been prescribed, that is the density profile has a fixed smooth shape in the interfacial region, where this profile is problem independent, the integral in (2.43) will have a constant value $I(a)$ [53]:

$$I(a) = \int \left(\frac{\partial \phi}{\partial z} \right)^2 dz \quad (2.44)$$

Here, we have allowed for the possibility that the EOS, which we have fixed, may depend on some parameter a . He and Chen [71] adopted a fairly general Carnahan-Starling (C-S) EOS [41], which the latter authors showed rather cleverly to be an excellent approximation to a general virial equation of state for non-ideal gases which can be derived using kinetic theory arguments

[55, 71]¹³. We have incorporated the C-S EOS for all of our simulations with the H-C method.

The C-S EOS takes the form [71]:

$$p = \rho RT \left[\frac{1 + \frac{b\rho}{4} + \left(\frac{b\rho}{4}\right)^2 - \left(\frac{b\rho}{4}\right)^3}{\left(1 - \frac{b\rho}{4}\right)^3} \right] - a\rho^2 \quad (2.45)$$

Here, b is typically taken to be 4, and “a” is a repulsion parameter [55]. The critical temperature T_c below which two stable (and immiscible in this context) states will exist is given in [71]:

$$T_c = 0.3773a/bR \quad (2.46)$$

We follow the convention taken by several authors to fix the value of $RT = c_s^2 = 1/3$ and instead use “a” as our parameter used to implicitly define a critical temperature. All studies (unless noted) are performed with $a = 4$. Keep in mind this prescription of “a” will control the stable values of density and of the smoothness of the interface. To allow for arbitrary densities to be chosen,¹⁴ He and Chen [71] chose to write the C-S equation in terms of the index ϕ instead of the density. The bounds on the index could then be mapped to the densities of each component via equation (2.32) which allows for the possibility of arbitrary prescription. The C-S EOS enters the H-C algorithm in a similar form as found in the S-C algorithm, i.e. as the gradient of a scalar potential. Whereas the surface tension and EOS are encapsulated in this potential form in the S-C algorithm, the EOS and surface tension are partially decoupled in the H-C algorithm in that their

¹³ The perceptive reader will note that the first term in the C-S equation, to leading order is the ideal gas equation where higher order terms come from n-molecule interactions [55].

¹⁴ Again, subject to the stability of the calculation. Increasing the density ratio decreases the stability of the calculation.

respective terms are distinct in the governing equations. The EOS enters in equations (2.28), (2.29), (2.38) and is written via the interaction potential:

$$\psi(\rho) = p - \rho RT \quad (2.47)$$

for equations (2.29), (2.38) and

$$\psi(\phi) = \phi RT \left[\frac{1 + \frac{b\phi}{4} + \left(\frac{b\phi}{4}\right)^2 - \left(\frac{b\phi}{4}\right)^3}{\left(1 - \frac{b\phi}{4}\right)^3} - 1 \right] - a\phi^2 = p_{CS}(\phi) - \phi RT \quad (2.48)$$

for (2.28). Here, the Carnahan-Starling pressure as calculated from equation (2.45) is identified as $p_{CS}(\phi)$ for emphasis. The gradients of the interaction potentials are calculated by a compact scheme similar to that given in [65]. With the C-S EOS and its repulsion parameter, a , specified through the interaction potential, we can return to the prescription of surface tension. This prescription allows $I(a)$ in equations (2.43) and (2.44) to be calculated and the surface tension can therefore be calculated as in equation (2.43). For $b = 4$, Zhang et al. [53] calculated the critical value of a , corresponding to the critical temperature to be $a_c = 3.53374$. A correlation for $I(a)$ was developed over a values in the range $a \in [a_c, 4.6]$, where $a > a_c$ corresponds to $T < T_c$. For the reader's reference, $I(a)|_{a=4} \approx 0.0146$. With $I(a)$ known, the surface tension σ may now be explicitly chosen.

This concludes the discussion of the relevant equations in the H-C algorithm. An extension to the H-C algorithm is discussed in the next section.

2.4 Pressure Poisson Modification

Any LBM algorithm, be it the Shan and Chen, or the He and Chen method, is fundamentally a compressible flow algorithm. That is, no matter the equation of state specified, pressure will always be a function of density in LBM. In simulating compressible flows, this point does not present any issue. However the point is very important with respect to the simulation of incompressible flows (which is the purpose of our work). Authors [79, 56, 57] have argued that in the limit of low Mach number Ma , the effects of compressibility will be small so that an approximately incompressible system can be modeled with reasonable accuracy. Since, to leading order, the variation of state variables (pressure, density) carry a quadratic dependence on Mach number, flows where the Mach number is less than 0.3 are often considered incompressible since the characteristic variation of the state variable will typically be less than 10%. As will be presented in later section, we have found that the condition of low Mach number is not sufficient to guarantee incompressibility in the Lattice Boltzmann scheme. Specifically, compressibility may affect the density of fluid material significantly, at low Mach numbers. Other parameters including surface tension also affect the compressibility and will be discussed in Chapter 3. Because of these compressibility errors, we considered implementing a correction that would yield a pressure field consistent with an incompressible flow. Inamuro [64] first considered implementing such a correction, namely a Pressure Poisson equation (PPE) into the LBM formulation and found that the calculation was stable at much higher density ratios. Because our ultimate goal is to simulate vapor-liquid flows, this finding was particularly encouraging and gave another reason for reducing compressibility effects.

Our task now is to seek a pressure that guarantees the flow remains incompressible. Before writing down the solution, it is important to be precise about what constraint

incompressibility puts on the velocity field in a multiphase flow. The constraint will not be consistent across all multiphase flows, so we define more precisely multiphase flows characterized by immiscible Newtonian fluids of possibly differing fluid properties. We may equivalently express such a system as a single fluid with spatially varying viscosity and density where surface tension exists in every neighborhood that there is density variation. Regions of density variation are called interfaces. Under this assumption, the normal continuity equation applies¹⁵:

$$\frac{\partial \rho}{\partial t} + \frac{\partial}{\partial x_i} (\rho u_i) = 0 \quad (2.49)$$

This equation may be re-written as:

$$\frac{D\rho}{Dt} = \frac{\partial \rho}{\partial t} + u_i \frac{\partial \rho}{\partial x_i} = -\rho \frac{\partial u_i}{\partial x_i} \quad (2.50)$$

where D/Dt is a material derivative. The condition of a solenoidal velocity field (i.e. $\frac{\partial u_i}{\partial x_i} = 0$) is still appropriate. Such a condition yields the resulting advection equation for the density:

$$\frac{D\rho}{Dt} = \frac{\partial \rho}{\partial t} + u_i \frac{\partial \rho}{\partial x_i} = 0 \quad (2.51)$$

¹⁵ This section relies heavily on index notation. Note here that subscripts in general denote components of a vector and do *not* correspond to e_i lattice directions.

Similarly, the viscosity obeys the same material equation. It is with this understanding that the density and viscosity may vary both spatially and temporally at every point in the flow. In the Lagrangian sense however, the density and viscosity of each fluid material element will not change since in a reference frame moving with each piece of fluid material, the material derivative of any fluid property is zero.

We may now derive the pressure equation consistent with the incompressibility condition. The pressure equation is derived under the assumption the LBM equations recover the incompressible Navier-Stokes equations in the limit of small Mach Number [56]. The Navier-Stokes equations for incompressible, Newtonian fluids are written as:

$$\frac{\partial u_i}{\partial t} + u_j \frac{\partial u_i}{\partial x_j} = -\frac{1}{\rho} \frac{\partial p}{\partial x_i} + \frac{\mu}{\rho} \frac{\partial^2 u_i}{\partial x_j \partial x_j} \quad (2.52)$$

(2.52) is applicable to variable density flows, however, the incorporation of surface tension and variable viscosity would introduce additional terms.¹⁶ Assume we solve equation (2.52) with a fractional-step scheme such that an intermediate velocity u_i^* satisfies the momentum equations, but is not necessarily divergence-free. Thus, this velocity satisfies:

$$\frac{\partial u_i^*}{\partial t} = -u_j \frac{\partial u_i}{\partial x_j} + \frac{\mu}{\rho} \frac{\partial^2 u_i}{\partial x_j \partial x_j} \quad (2.53)$$

¹⁶ These additional terms will end up being irrelevant, at least with respect to the derivation of the pressure equation.

Subtracting (2.53) from (2.52), we have:

$$\frac{\partial(u_i - u_i^*)}{\partial t} = -\frac{1}{\rho} \frac{\partial p}{\partial x_i} \quad (2.54)$$

Finally, taking the divergence of (2.54) results in the elliptic pressure Poisson equation (PPE):

$$\frac{\partial}{\partial x_i} \{2.54\} \rightarrow \frac{\partial}{\partial x_i} \left(\frac{1}{\rho} \frac{\partial p}{\partial x_i} \right) = \frac{\partial}{\partial t} \left(\frac{\partial u_i^*}{\partial x_i} \right) \quad (2.55)$$

It is important to note that Equation (2.55) is non-separable. There are various schemes for solving such an equation e.g. [61]. We discretize the left-hand side of (2.55) using a finite-volume scheme and the right-hand side is discretized using central differencing. The left-hand side can be written in two-dimensions as¹⁷:

$$\frac{\partial}{\partial x} \left(\frac{\nabla p}{\rho} \right) + \frac{\partial}{\partial y} \left(\frac{\nabla p}{\rho} \right) \approx \frac{\left[\frac{1}{\rho} \frac{\partial p}{\partial x} \right]_{i+1/2,j} - \left[\frac{1}{\rho} \frac{\partial p}{\partial x} \right]_{i-1/2,j}}{\Delta x} + \frac{\left[\frac{1}{\rho} \frac{\partial p}{\partial y} \right]_{i,j+1/2} - \left[\frac{1}{\rho} \frac{\partial p}{\partial y} \right]_{i,j-1/2}}{\Delta y} \quad (2.56)$$

This expression can be further discretized as:

$$\frac{\frac{1}{\rho_{i+1/2,j}} \left[\frac{p_{i+1} - p_i}{\Delta x} \right] - \frac{1}{\rho_{i-1/2,j}} \left[\frac{p_i - p_{i-1}}{\Delta x} \right]}{\Delta x} + \frac{\frac{1}{\rho_{i,j+1/2}} \left[\frac{p_{j+1} - p_j}{\Delta y} \right] - \frac{1}{\rho_{i,j-1/2}} \left[\frac{p_j - p_{j-1}}{\Delta y} \right]}{\Delta y} \quad (2.57)$$

¹⁷ Regard the change in notation in the discussion of discretization, where a typical grid point is centered (i, j) .

Where, for example,

$$\rho_{i+1/2,j} = \frac{1}{2}(\rho_i + \rho_{i+1}) \quad (2.58)$$

Assuming the compressibility error from the previous time step is small, the source-term on the right-hand side of (2.55) is discretized as:

$$\frac{\partial}{\partial t} \left(\frac{\partial u_i^*}{\partial x_i} \right) \approx \frac{1}{\Delta t} \left(\frac{u_{i+1}^* - u_{i-1}^*}{2\Delta x} + \frac{v_{j+1}^* - v_{j-1}^*}{2\Delta y} \right) \quad (2.59)$$

The entire PPE may then be written in the form:

$$(A + B + C + D)p_{i,j} = Ap_{i+1} + Bp_{i-1} + Cp_{j+1} + Dp_{j-1} - S_{i,j} \quad (2.60)$$

Here, $A = 1/\rho_{i+1/2,j}$, $B = 1/\rho_{i-1/2,j}$, $C = 1/\rho_{i,j+1/2}$, $D = 1/\rho_{i,j-1/2}$, and $S_{i,j}$ is the source term. This resulting discretized equation is solved using a point-Jacobi scheme, so that:

$$(A + B + C + D)p_{i,j}^{n+1} = Ap_{i+1}^n + Bp_{i-1}^n + Cp_{j+1}^n + Dp_{j-1}^n - S_{i,j} \quad (2.61)$$

While more efficient solvers could have been used, the algorithm's implementation on a GPU made the simple Jacobi solver the most appropriate choice. Nevertheless, the pressure solver made a substantial difference on the overall system compressibility as will be discussed in Chapter 3. For completeness, the velocity is corrected by:

$$u = u^* - \frac{\Delta t}{\rho_{i,j}} \left[\frac{p_{i+1} - p_{i-1}}{2\Delta x} \right] \quad (2.62)$$

The discussion of algorithm implementation is given in section 2.6, including how the PPE is integrated into the LBM algorithms.

2.5 GPU Implementation

Each of the LBM algorithms discussed has been implemented on a Graphics Processing Unit (GPU). Unlike single core Central Processing Units (CPUs), which may only do single tasks in succession, GPUs are many core architectures capable of performing parallel multi-task calculations with great efficiency. Whereas CPUs are optimized for sequential tasks, where often

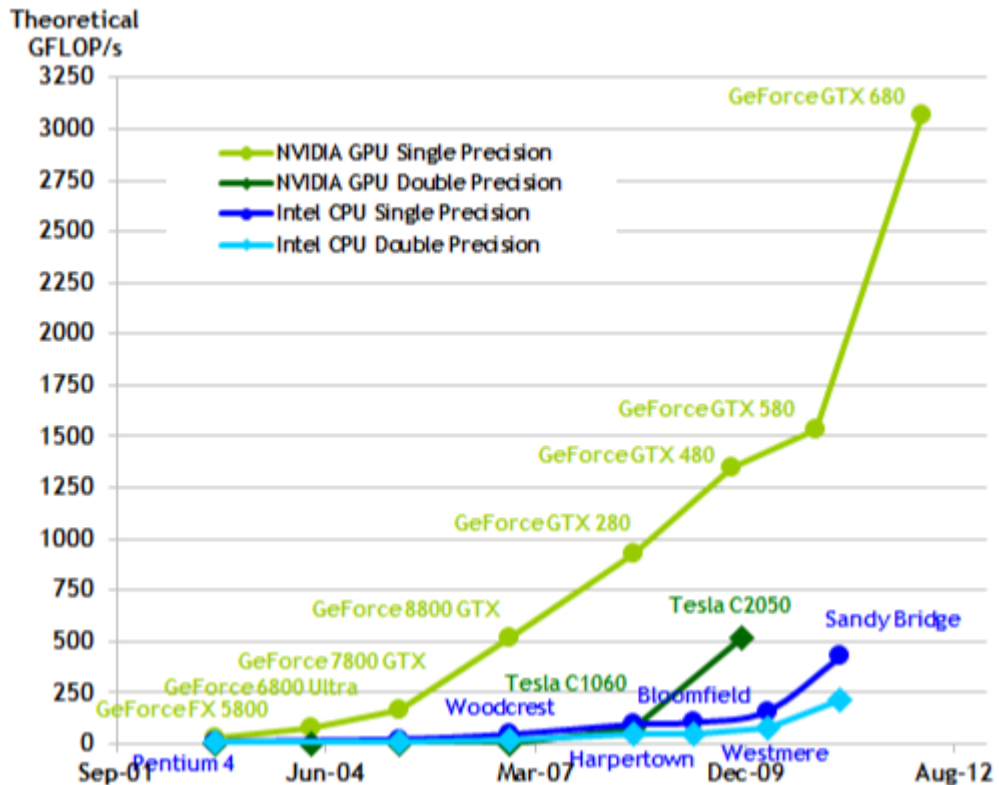


Figure 2.11: GPU vs. CPU theoretical peak performance, variation with time, reproduced from [43].

a piece or pieces of data are processed according to whether some set of conditionals are satisfied in succession, GPUs are optimized for handling large data sets where identical or nearly identical instructions are applied to each piece of data [43]. For this reason, an optimized algorithm on a GPU may significantly outperform the most optimized CPU version of the same algorithm. This

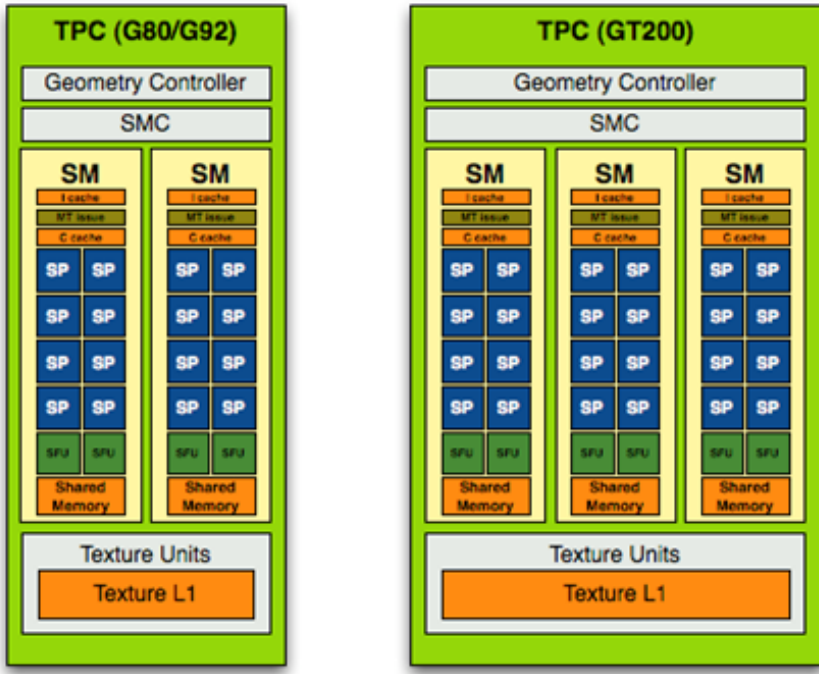


Figure 2.12: G80 and GT200 GPU architectures, reproduced from [9].

trend is evident in examining *Figure 2.11*. For example, in 2009, the peak theoretical performance of the NVIDIA GeForce GTX 480 was approximately 10 times greater than the leading Intel processor at the time. A typical GPU architecture is shown in *Figure 2.12*. A typical GPU is a hierarchy where the top level is Streaming multiprocessor (SM) which is further divided into smaller streaming processors (SPs) [15]. The SMs are responsible for dividing up the workload among each SP. Each SP itself may then launch many threads concurrently. What is also evident in *Figure 2.12* is the existence of multiple discrete memory units, including Texture L1, Shared Memory, various Cache, and Global Memory (not pictured). A large part of developing a parallel algorithm is deciding how to process data most efficiently. That is, different types of memory have different finite sizes and access times. For example, global memory is relatively large and can hold lots of data, but the access time, that is, the time required for a thread to access the piece of data before any operations are performed on that data,

```

dim3 block(bx_f);
dim3 grid1(ncell_grid);
collision_kernel<<<grid1, block>>> (Fx_d, Fy_d, Fz_d, rho_d, rhoavg,
    gx, gy, gz, kappa, phi_d, dd2phix_d, dd2phiy_d, dd2phiz_d, ex_d,
    ey_d, ez_d, t_d, u_d, v_d, w_d, f_d, tau_d, psix_d,
    psiy_d, g_d, psix1_d, psiy1_d, psiz_d, psiz1_d, nu_d, nxm_d, nym_d,
    nxp_d, nyp_d, ncell, ptherm_d);

cutilCheckMsg("Kernel execution failed");

dim3 grid2(ntotal_ncell_grid);

boundfg_kernel<<<grid2, block>>> (ncell, nintr_d, u_d, v_d, w_d,
    uin, vin, f_d, g_d, phi_d, ex_d, ey_d, ez_d,
    t_d, rho_d, ub_d, alpha_d, wb_d, beta_d, pin, dpdx, ntotal, vb_d, pb_d, ptherm_d);

cutilCheckMsg("Kernel execution failed");
global void
boundfg_kernel (int ncell, int *nintr_d, NUMBER_DUB *u_d, NUMBER_DUB *v_d, NUMBER_DUB *w_d,
    NUMBER_DUB uin, NUMBER_DUB vin, NUMBER_DUB *f_d,
    NUMBER_DUB *g_d, NUMBER_DUB *phi_d, NUMBER_DUB *ex_d, NUMBER_DUB *ey_d, NUMBER_DUB *ez_d,
    NUMBER_DUB *t_d, NUMBER_DUB *rho_d, NUMBER_DUB *ub_d, int *alpha_d, NUMBER_DUB *wb_d,
    int *beta_d, int *delta_d, NUMBER_DUB pin, NUMBER_DUB dpdx, int ntotal, NUMBER_DUB *vb_d, NUMBER_DUB *pb_d)
{
    int ij, k, ijn, ijk, ijk;
    NUMBER_DUB ut, vt, wt, feqt, term, term1, pt, ptijn;
    int tx = threadIdx.x + blockIdx.x * blockDim.x;
    ij = tx + ncell + 1;
    if(ij <= ntotal)
    {
        // Boundary conditions for f and g
        ijn = nintr_d[ij];
        ut = alpha_d[ij] * (2.0 * ub_d[ij] - u_d[ijn]) + (1.0 - alpha_d[ij]) * u_d[ijn];
        vt = alpha_d[ij] * (2.0 * vb_d[ij] - v_d[ijn]) + (1.0 - alpha_d[ij]) * v_d[ijn];
        wt = alpha_d[ij] * (2.0 * wb_d[ij] - w_d[ijn]) + (1.0 - alpha_d[ij]) * w_d[ijn];
        ptherm_d[ij] = delta_d[ij] * (2.0 * pb_d[ij] - ptherm_d[nintr_d[ij]]) + (1 - delta_d[ij]) * ptherm_d[nintr_d[ij]];
        pt = ptherm_d[ij];
        ptijn = ptherm_d[ijn];
        for (k = 1; k<=27; k++ ) {
            ijk = (ij -1) * 27 + k;
            ijk = (ijn -1) * 27 + k;
            term1 = 3.0 * (ex_d[k] * ut + ey_d[k] * vt + ez_d[k] * wt) +
                4.5 * (powf ((ex_d[k] * ut + ey_d[k] * vt + ez_d[k] * wt), 2.0)) - \
                1.5 * (powf (ut, 2.0) + powf (vt, 2.0) + powf (wt, 2.0));
            f_d[ijk] = t_d[k] * phi_d[ij] * (1.0 + term1);
            g_d[ijk] = t_d[k] * (pt + (rho_d[ij] / 3.0) * term1);
        }
    }
}

```

Figure 2.13: CUDA code, main source code containing kernel calls (top), kernel code (bottom).

is relatively large for global memory. In contrast, shared memory can be accessed relatively quickly, but the amount of data that can be stored in shared memory is relatively small. Other memory access issues concern the scope of the data, that is, which threads can access which pieces of data. Data in global memory may be accessed by any thread. Another type of

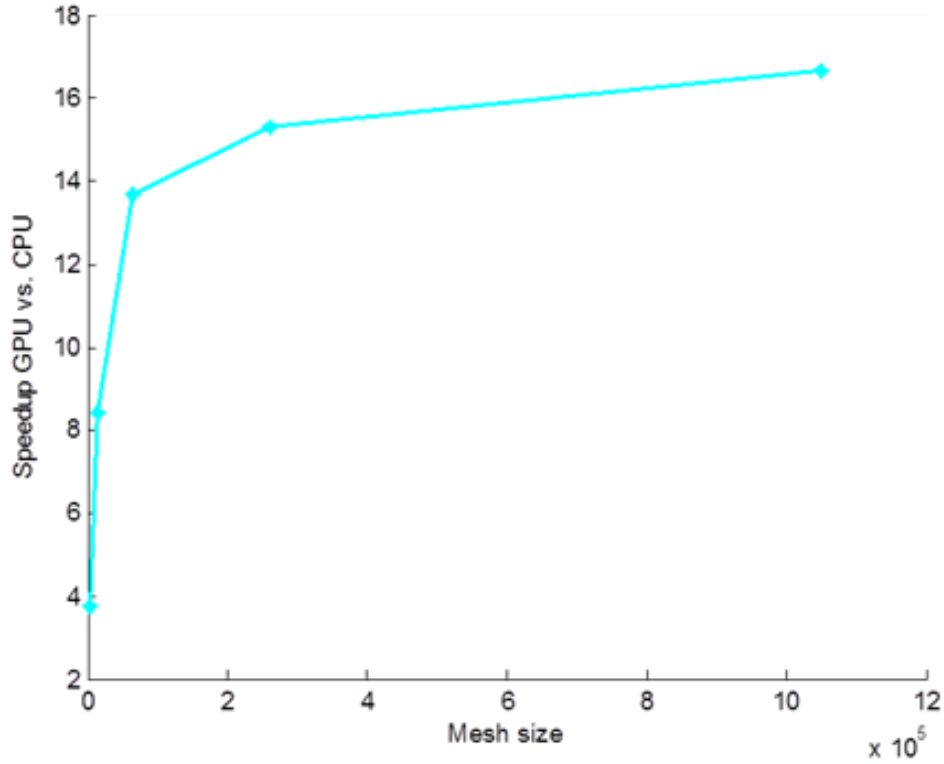


Figure 2.14: Speedup between GPU and CPU code for different problem sizes.

memory called registers have the lowest access time and the smallest size. Typically, there will be a register that is assigned to and only accessible by its own thread [15]. Of course there are other issues that arise in implementing a parallel code on a GPU. However, this discussion gives the reader a brief introduction into considerations the developer takes when implementing a parallel algorithm.

Each LBM algorithm has been written in CUDA and programmed on a CUDA-compatible NVIDIA GPU. CUDA is a programming language that extends C. A portion of our CUDA code is shown in *Figure 2.13*. Much of the CUDA algorithm is no different than a C code. The computational strategy is often called hybrid, that is, data I/O is done on the CPU side. Initial Conditions, domain specification, and memory allocation are handled by the CPU. Then, all data that will be processed by the GPU are copied from CPU memory into GPU global memory. Once all of the data have been copied, a special CUDA command called a kernel is

launched. Referring to the top pane in *Figure 2.13*, a kernel looks like a typical function call in C, except it begins with the syntax `<<<arg, arg>>>`. A kernel is a direct command to the GPU telling it to execute the named function, `collision_kernel` and `boundfg_kernel` in this case, on the data passed within the parenthesis. The arguments in the brackets are used to manage the number of threads that will be launched on the GPU. Consider now the bottom pane in *Figure 2.13*. Besides a few specifiers needed to identify this code as a GPU function, everything in the `boundfg_kernel` routine is C code. The reader will note the variable `tx`, which is later passed to a variable called `ij`, represents a thread number. The thread number is a way of identifying each thread. In this way, it is possible to write one code which tells each thread to do a different task, (more precisely, the same task on different pieces of data). That is, each thread may execute the same code, but the piece of data each thread operates on is different. Consider in *Figure 2.13* the line pointed to by the red arrow. Thread `ij` will perform this calculation and store the result in the ij^{th} location of the `p_therm` array. Because each thread has a unique `ij`, one line of code can be written to tell a large number of threads to perform the same task on different pieces of data.

To assess the performance of our GPU code, we also wrote a CPU code and performed a calculation on the model problem shown in *Figure 2.10*. The test was carried out using the Shan-Chen algorithm. We did our best to implement this algorithm on both architectures incorporating little optimization to get an idea of the inherent parallelism within the LBM algorithm itself and also between the GPU and CPU architectures. Calculations were performed on an NVIDIA Tesla C1060 (1.30 GHz) GPU and an Intel Xeon 5160 (3.00 GHz). The results are shown in *Figure 2.14*. Even though our implementations were relatively naïve, we were able to achieve approximately a 15x speedup on the GPU code vs. the CPU code. Therefore, we were able to demonstrate the inherently parallel nature of LBM and achieve significant speedup for the GPU

code compared with the CPU code without spending a lot of time on code development. For more information regarding the development of CUDA codes, the interested reader is referred to the CUDA C Programming Guide [43] and Kirk and Hwu's *Programming Massively Parallel Processors: A Hands-on Approach* [15].

2.6 Algorithm Flowcharts

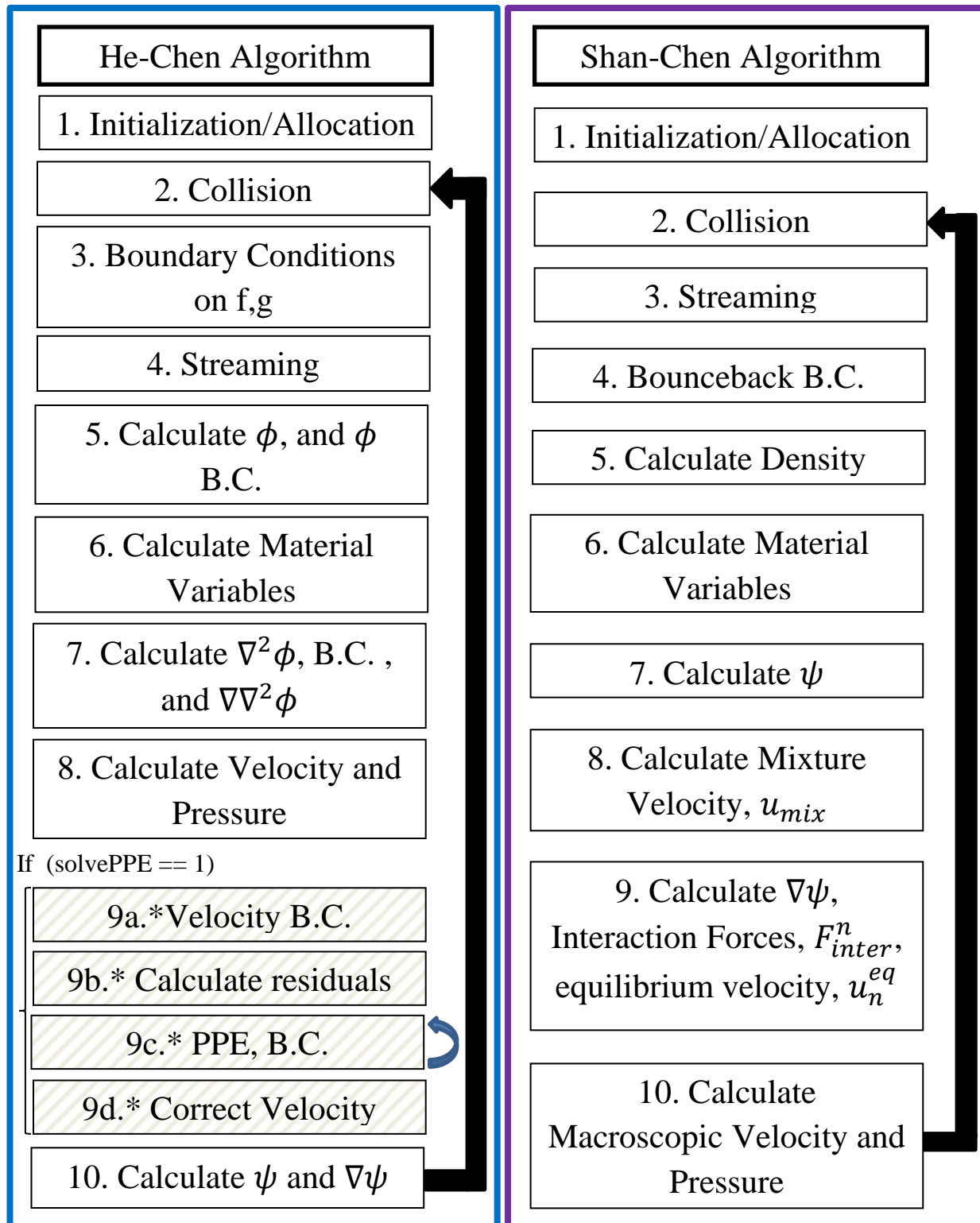


Figure 2.15: LBM Algorithm Flowcharts:
 He-Chen Algorithm, Pressure Poisson Modification, Shan-Chen Algorithm

Flowcharts for the He-Chen and Shan-Chen algorithms are shown in *Figure 2.15*. The He-Chen flow chart also has an optional section where a pressure Poisson equation is solved to reduce any compressibility errors¹⁸. Both the H-C and S-C algorithms begin with an initialization phase where a domain and boundary conditions are specified. Macroscopic variables (density, velocity, pressure) are specified at interior points and pdfs are initialized to their equilibrium values. Then, the algorithms begin marching in time starting with a collision phase where the distributions are collided with their equilibrium values (subject to explicit or implicit forcing terms). In the H-C algorithm, we have prescribed ghost-fluid boundary conditions. These B.C.'s are applied before updated pdfs are streamed along discrete velocity vectors according to the lattice directions. In the S-C algorithm, we have implemented the Bounceback boundary condition. Therefore, in the S-C implementation, there are two rounds of streaming. The first streaming step is carried out exclusively for interior nodes. The bounceback boundary condition is then applied to determine what portion of the pdf were streamed out of the domain. Finally, a post-bounceback streaming step is carried out to stream discrete boundary pdfs to the neighboring interior nodes (as described in *Figure 2.7*). The remaining steps in each algorithm are used to calculate macroscopic variables. In the H-C method, the index function is calculated from the f-distribution function. Once the index function is known, the density at each node can be calculated by linear interpolation. The density in the S-C method however is calculated directly by summing the f-distributions for each component at a given node. In step 6 of each algorithm, material variables (kinematic viscosity, relaxation time) of each fluid component are

¹⁸ Note, this optional section is NOT present in the Sean-Chen algorithm. We attempted to implement the PPE equation into the Sean-Chen algorithm. However, because multiple velocities are defined in the S-C method, it was unclear which velocity to correct to guarantee an incompressible flow and how to correct it. We were ultimately not successful in formulating a strategy that included solving a PPE and ultimately correcting a velocity to satisfy a divergence-free velocity condition for the S-C method. The PPE modification to the H-C method however was successful using the strategy discussed in the previous section; results with this modification are presented in the next section.

calculated. In step 7 of the H-C algorithm, discrete differential operators are applied to the index function. These expressions are used to evaluate the surface tension force which is applied as a body force in the collision phase at the beginning of the next time step. At this point in the S-C algorithm, the interaction potential (which is used to model observable macroscopic forces based on intermolecular interactions) is evaluated using an equation of state. After calculating a mixture velocity, the interaction potential is used to evaluate the net interaction force on each component which can then be used to calculate an equilibrium velocity for each component. This equilibrium velocity is used to evaluate the equilibrium distribution function used in collision at the beginning of the next time step. With the interaction forces and interaction potential known, macroscopic fluid velocity and pressure can be calculated in step 10 of the S-C algorithm. All information is now known and the S-C algorithm returns to the collision step. Returning to the H-C algorithm, the macroscopic velocity and pressure are calculated using the g-distribution function obtained during the collision phase. If no PPE is being solved, the time step is completed after an interaction potential, defined according to the C-S EOS, and its gradient are calculated.

If a PPE is being solved, extra care must be taken. The pressure calculated in step 8 will be called the thermodynamic pressure, that is, it is the pressure consistent with the prescribed equation of state. This pressure is NOT used in the PPE. Rather, a new pressure is defined, whose sole purpose is to correct the velocity field¹⁹. When solving the PPE, it is necessary to first apply boundary conditions on the temporary velocity field and calculate the residual or source term in the PPE given in (2.61). In our implementation, we next perform an iterative

¹⁹ Strictly speaking, it is not incorrect to work with the thermodynamic pressure in the PPE since we have already defined this as the macroscopic fluid pressure. However, we have completed trial runs such as fully developed single-phase flow in a channel and have found that it is necessary to work with a second pressure whose sole purpose is to correct the velocity to ensure a solenoidal field. It is this pressure, whose gradient can be compared with the analytical pressure drop needed for a given flow rate in a channel, for example.

Jacobi solver where the pressure at a given node is corrected successively based on the neighboring pressures and the local source term²⁰. After each iteration, boundary conditions are applied on the pressure field. After the residual to the PPE have satisfactorily converged, the macroscopic velocity is corrected using the pressure field obtained from the PPE according to equation (2.62)²¹. The corrected velocity is then used to evaluate the equilibrium distribution function for the g-distribution in the collision phase at the beginning of the next time step.

Having presented the various LBM methods and discussed the implementation of the respective algorithms, we can now present results obtained from each of the methods. These results are the respective subjects of the remaining chapters.

²⁰ More powerful solvers could have been implemented such as multigrid. The GPU architecture made a Jacobi solver much easier to implement than Gauss-Seidel Successive Over-Relaxation for example, although this type of solver is possible to implement using a Black-Red strategy for example [30]. However, our main goal with the PPE modification was to see if the PPE could make a difference as far as compressibility errors were concerned and we started with the simplest implementation of the PPE. Our results suggest that even a naïve PPE solver makes a substantial difference in a number of flow regimes.

²¹ It is important to note this pressure, which is consistent with an incompressible flow, is not used anywhere else in the algorithm. When not discussing the PPE modification to H-C algorithm, it should be assumed that any mention of pressure is the thermodynamic pressure related to the g-distribution function.

3. SIMULATION OF DISPERSED MULTIPHASE FLOW IN A CHANNEL

3.1 Problem Description

The use of LBM to simulate incompressible flow is of great interest. Several authors [71, 64, 65] have used LBM to simulate incompressible multiphase flows. However, LBM is fundamentally a compressible flow procedure. Unlike the Navier-Stokes equations, pressure is not explicitly present in the Lattice Boltzmann equation. Pressure only enters the LBM procedure after interaction forces have been appropriately modeled. Depending on how the interaction forces are modeled, a different pressure will be implied. This pressure will in general be related to the density via a non-ideal gas EOS. This is counter to the notion of an incompressible fluid. However, as many authors [57, 74] have shown, it is possible to recover the Navier-Stokes equations from the Boltzmann equation and that any compressibility errors should remain small provided the Mach number is small compared to unity. The goal of this section is to show the assumption of small Mach number is not always sufficient to guarantee that the compressibility errors in an LBM simulation are small. Specifically, we explore the effect of the system density ratio, surface tension, Mach number, and Reynolds number on the magnitude of the compressibility.

A second task of this section addresses how to mitigate these errors. As with many multiphase flow schemes, LBM calculations become increasingly unstable as the density ratio increases. One hypothesis is that compressibility errors and/or spurious currents (generated by discretizing a steep or discontinuous interface) can decrease the stability of a calculation. This has limited LBM calculations to low density ratio flow problems (typically 10:1 or less for the H-C algorithm, and O(100) for the S-C algorithm depending on the EOS chosen). However in

2004, Inamuro [64] showed that the addition of a pressure Poisson equation (PPE) could dramatically increase the density ratio that could be simulated with an LBM algorithm. His LBM algorithm was based on the free-energy LBM procedure developed by Swift [38]. Inamuro extended this work by introducing a PPE into the LBM procedure and showed that the new procedure was capable of simulating density ratios of 1000:1.

Therefore, the addition of a PPE into our own LBM algorithm seemed an appropriate strategy to explore. Ostensibly, the PPE could allow our LBM algorithm to handle higher density ratio problems. Because our goal is to simulate flows of interest to the industry sponsors of the Air Conditioning and Refrigeration Center (ACRC), it is necessary to develop an algorithm that is capable of handling high density ratios which are typical of industrial flows in the ACRC context. The other ostensible advantage was a PPE would reduce compressibility errors which yield a formulation more in line with an incompressible flow solver.

In the next section, we solve a model problem and present a number of results to quantify compressibility errors that are inherent in the LBM algorithm. We then solve the same problem with the PPE modification to our LBM algorithm which will allow us to assess the advantages and disadvantages of such a modification.

3.2 Results²²

The model problem we study is shown in *Figure 3.1*. The domain is a two-dimensional channel with an aspect ratio of 20:1. The carrier fluid enters the domain with a uniform velocity profile of magnitude U_0 and density ρ_1 . A secondary phase of density ρ_2 and diameter d equal to half the channel height is prescribed at the center of the domain. For cases in which the secondary phase is lighter than the carrier phase, that is $\rho_1/\rho_2 > 1$, the secondary phase is referred to as a light droplet while in the opposite case, the secondary phase is called a heavy droplet. All fluid in the domain is initialized with the uniform inlet velocity. Unless otherwise

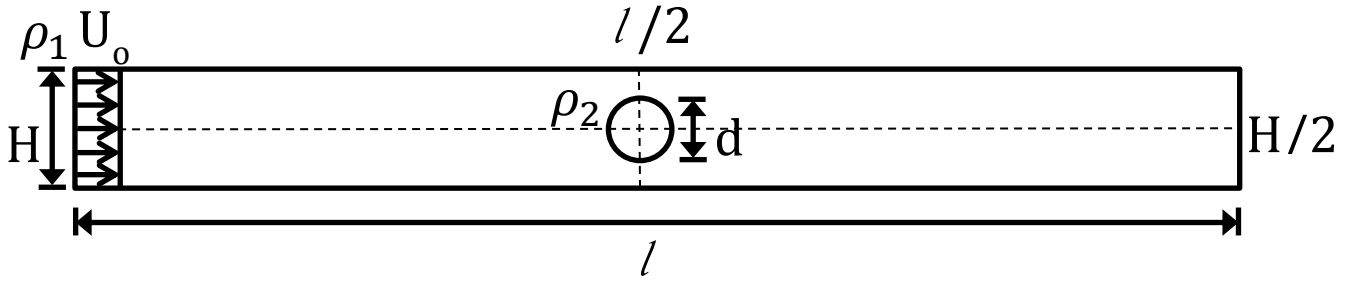


Figure 3.1: Simulation domain for PPE study.

| | |
|------------------|----------------|
| d | 50 l.u. |
| l | 2000 l.u. |
| H | 100 l.u. |
| U_0 | 0.00333 l.u./s |
| τ_1, τ_2 | 0.6 |

Table 3.1: Geometric Parameters, channel flow simulations with and without PPE.

noted, relaxation time of both fluids is the same and equal to 0.6. A summary of the cases considered is presented in *Table 3.2-3.9*. Specifically, we study the effect of density ratio, surface tension magnitude, Mach number, and Reynolds number on the system's compressibility. In addition, we explore whether the system's compressibility is changed if the secondary phase

²² A portion of this results section was presented at APS DFD 2012.

Density Ratio Study

| Case | Re | Ma | ρ_1/ρ_2 | k |
|---------|------|---------|-----------------|-----|
| 1. a, b | 10.0 | 0.00577 | 1.0 | 0.0 |
| 2. a, b | 10.0 | 0.00577 | 2.0 | 0.0 |
| 3. a, b | 10.0 | 0.00577 | 5.0 | 0.0 |
| 4. a, b | 10.0 | 0.00577 | 10.0 | 0.0 |

Table 3.2: Effect of PPE on calculation of developing channel flow varying the density ratio, a-No PPE, b-PPE.

| Case | Re | Ma | ρ_1/ρ_2 | k |
|---------|------|---------|-----------------|-----|
| 5. a, b | 10.0 | 0.00577 | 0.5 | 0.0 |
| 6. a, b | 10.0 | 0.00577 | 0.2 | 0.0 |
| 7. a, b | 10.0 | 0.00577 | 0.1 | 0.0 |

Table 3.3: Effect of PPE on calculation of developing channel flow varying the density ratio, a-No PPE, b-PPE.

Surface Tension Study

| Case | Re | Ma | ρ_1/ρ_2 | k |
|----------|------|---------|-----------------|------|
| 8. a, b | 10.0 | 0.00577 | 2.0 | 0.01 |
| 9. a, b | 10.0 | 0.00577 | 2.0 | 0.1 |
| 10. a, b | 10.0 | 0.00577 | 2.0 | 1.0 |
| 11. a, b | 10.0 | 0.00577 | 2.0 | 2.0 |

Table 3.4: Effect of PPE on calculation of developing channel flow varying the surface tension, a-No PPE, b-PPE.

| Case | Re | Ma | ρ_1/ρ_2 | k |
|-----------|------|---------|-----------------|------|
| 12. a, b* | 10.0 | 0.00577 | 0.5 | 0.01 |
| 13. a, b* | 10.0 | 0.00577 | 0.5 | 0.1 |
| 14. a, b* | 10.0 | 0.00577 | 0.5 | 1.0 |
| 15. a, b* | 10.0 | 0.00577 | 0.5 | 2.0 |

Table 3.5: Effect of PPE on calculation of developing channel flow varying the surface tension, a-No PPE, b-PPE.

is a heavy or light droplet for a given ratio of densities²³. Specifically, we track the magnitude of the largest density variation for each phase in the system²⁴. Surprisingly, this does not always occur at early times when spurious currents are highest but may occur at later times as the

²³ We define only one density ratio for this model problem, i.e. ρ_1/ρ_2 . However, for the purpose of comparing a heavy droplet of one density ratio, 0.5 say, and a light droplet of another density ratio, say 2.0, these magnitudes will be regarded as being the most reasonable comparison when all other parameters (k , Ma, Re) are held constant since the ratio of fluid densities present in the system is a constant under these conditions.

Mach number Study

| Case | Re | Ma | ρ_1/ρ_2 | k |
|-------------|------|---------|-----------------|-----|
| 9/16. a, b* | 10.0 | 0.00577 | 2.0 | 0.1 |
| 17. a, b* | 10.0 | 0.0115 | 2.0 | 0.1 |
| 18. a, b* | 10.0 | 0.0288 | 2.0 | 0.1 |
| 19. a, b* | 10.0 | 0.0577 | 2.0 | 0.1 |

Table 3.6: Effect of PPE on calculation of developing channel flow varying the Mach number, a-No PPE, b-PPE.

| Case | Re | Ma | ρ_1/ρ_2 | k |
|--------------|------|---------|-----------------|-----|
| 13/20. a, b* | 10.0 | 0.00577 | 0.5 | 0.1 |
| 21. a, b* | 10.0 | 0.0115 | 0.5 | 0.1 |
| 22. a, b* | 10.0 | 0.0288 | 0.5 | 0.1 |
| 23. a, b* | 10.0 | 0.0577 | 0.5 | 0.1 |

Table 3.7: Effect of PPE on calculation of developing channel flow varying the Mach number, a-No PPE, b-PPE.

Reynolds number study

| Case | Re | Ma | ρ_1/ρ_2 | k |
|--------------|------|--------|-----------------|-----|
| 17/24. a, b* | 10.0 | 0.0115 | 2.0 | 0.1 |
| 25. a, b* | 20.0 | 0.0115 | 2.0 | 0.1 |
| 26. a, b* | 40.0 | 0.0115 | 2.0 | 0.1 |

Table 3.8: Effect of PPE on calculation of developing channel flow varying the Reynolds number, a-No PPE, b-PPE.

| Case | Re | Ma | ρ_1/ρ_2 | k |
|--------------|------|--------|-----------------|-----|
| 21/27. a, b* | 10.0 | 0.0115 | 0.5 | 0.1 |
| 28. a, b* | 20.0 | 0.0115 | 0.5 | 0.1 |
| 29. a, b* | 40.0 | 0.0115 | 0.5 | 0.1 |

Table 3.9: Effect of PPE on calculation of developing channel flow varying the Reynolds number, a-No PPE, b-PPE.

secondary phase moves downstream²⁵. Cases marked in green have been completed and their

²⁴ Recall that the continuity equation for the multiphase system allows for the possibility of the density at a point to change with time. However, the density of a piece of fluid material moving in the reference frame of that material must be constant. Therefore, the density of each phase, where it exists should be constant to satisfy the incompressibility condition.

²⁵ Spurious currents generated by discretizing sharp interfaces can generate local variations in density. During initialization, the density profile is literally a discontinuity. As the interface is diffused, eventually reaching the profile related to the prescribed EOS, the spurious currents are suppressed. We have explored initializing smoother interfaces such as hyperbolic tangent profiles. We found this may help in allowing a higher density ratio simulation to remain stable that would otherwise blow-up due to spurious currents generated at early times.

results are presented in the following subsections. Cases marked in red with an asterisk “*” were not completed due to time constraints.

3.2.1 Density Ratio Study (Cases 1-7)

The effect of density ratio on system density variation was explored in Cases 1-7 and summarized in *Tables 3.2* and *3.3*. The results are presented in *Figure 3.2* and *3.3*. Black asterisks and blue diamonds are respectively the density variation for the secondary phase and carrier phase as a function of density ratio. In *Figure 3.2*, the density variation is seen to increase as the density ratio increases when the dispersed phase is a light droplet. The density variation appears to increase exponentially in the secondary phase with increasing density ratio, while the density variation in the carrier phase changes only nominally as the density ratio is increased. Consider now the red x’s and green circles which represent, respectively the density variation in the secondary and continuous phases when a PPE equation has been solved. Observe, especially for the secondary phase, the dramatic difference in density variation with and without the PPE. At a density ratio of 5, the density variation in the droplet is approximately 18% without the PPE, but only about 3% with the PPE. The PPE has a comparatively nominal effect on the density variation in the continuous phase.

Consider now the case of a heavy droplet moving in a carrier fluid of lower density. Those results are presented in *Fig. 3.3*. We observe the opposite trends for density variation and effect of PPE. That is, the secondary phase (the droplet) exhibits only a small density variation whether or not a PPE is solved, while the PPE makes a substantial difference on the density variation in the continuous phase. When the carrier phase is 10x lighter than the droplet, the maximum density variation is about 5% with the PPE, and approximately 17% without the PPE. At this density ratio, the PPE provides little benefit to the droplet phase with regard to density

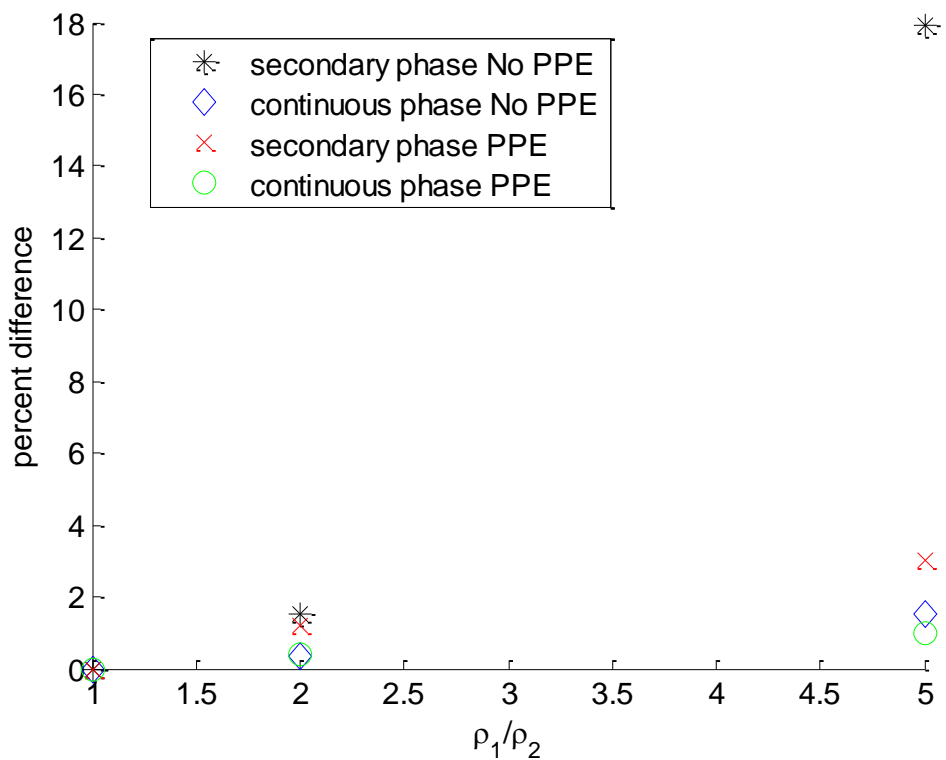


Figure 3.2: Density Ratio Study, $\text{Ma} = 0.00577$, $\text{Re} = 10$, $k = 0.0$.

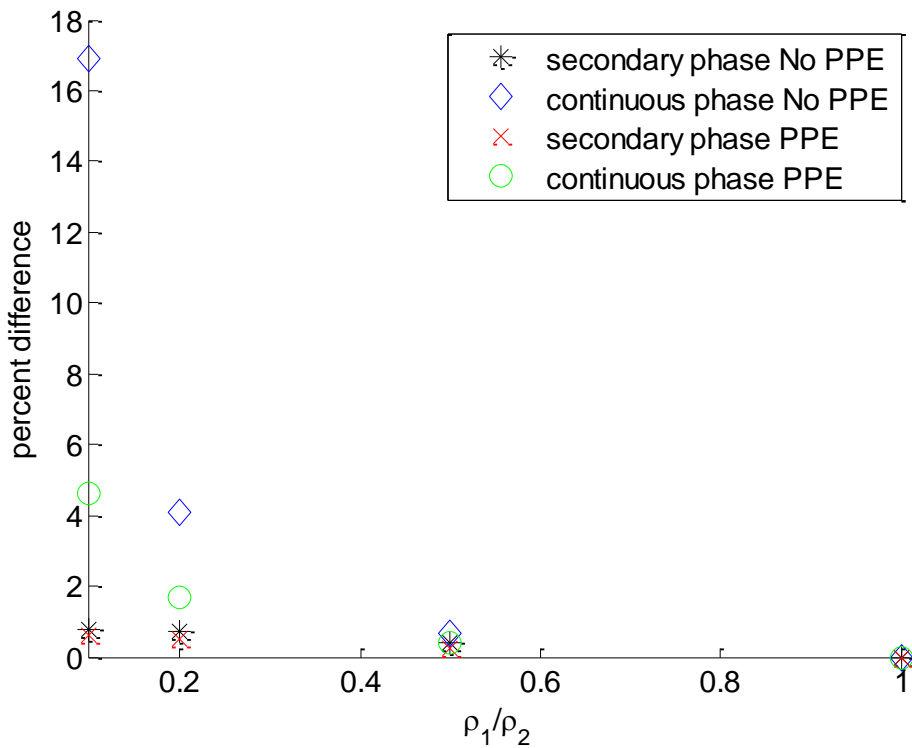


Figure 3.3: Density Ratio Study, $\text{Ma} = 0.00577$, $\text{Re} = 10$, $k = 0.0$.

variation. This suggests the density variation may tend to be highest in the lighter phase compared with the heavier phase, independent of whether the light phase is the dispersed or primary phase. These observations also suggest the PPE acts to reduce the density variation in the lighter phase and will have a comparably nominal effect on the heavier phase²⁶. We conclude this section by noting that the case of a unity density ratio experiences no density variation²⁷.

3.2.2 Surface Tension Study (Cases 8-15)

We have also examined the effect of surface tension on system density variation. In the He-Chen formulation, the magnitude of the surface tension force, scales with the k parameter, as shown in (2.43). We may expect that increasing the magnitude of the surface tension will increase the density variation owing to spurious currents generated by discretizing a sharp interface. The results are presented in *Figures 3.4* and *3.5*. When the secondary phase is a light droplet as shown in *Figure 3.4*, we see a similar trend as discussed earlier. That is, the largest density variation is exhibited in the lighter (secondary phase in this case). Interestingly, the density variation does not vary monotonically with increasing k . Rather, there appears to exist a local minimum in the density variation when plotted vs. k . That is, lower density variation is observed

²⁶ With regard to system stability, the reader will note that we had intended to explore a density ratio of 10 for the light droplet case, but this case was unstable. This suggests that heavy droplets may in general be more stable than light droplets for the same system density ratio.

²⁷ We sometimes observe that the interface of the dispersed phase may contract over time for very long simulations. This effect is most pronounced for coarse simulations or small droplets such that the diameter of the droplet is not large compared with the interfacial width (typically ~ 3 lattice units). Typically droplets smaller than 25 l.u. experience discernible contraction if simulated for long times. Any contraction present for larger droplets is typically too small to observe. This may also happen as a result of a mismatch between surface tension magnitude and prescribed droplet size. The pressure in and outside the droplet theoretically balances the interfacial tension, but small retraction (or sometimes expansion) of the interface may nonetheless be observed under the conditions previously discussed. It should be noted that zero density variation will occur at unity density ratio only for the H-C method, where the EOS is only used to determine interfacial thickness. In the S-C method, pressure is calculated directly from density via the EOS. In unbounded flows, the density variation may be small, for example in the case of two colliding droplets. However, in internal flows, where a pressure gradient is needed to drive the flow, large density variation may be observed, even for unity density ratio, and low Mach number. See Fig. 6 in [79] or *Figure 5.3* in Chapter 5.

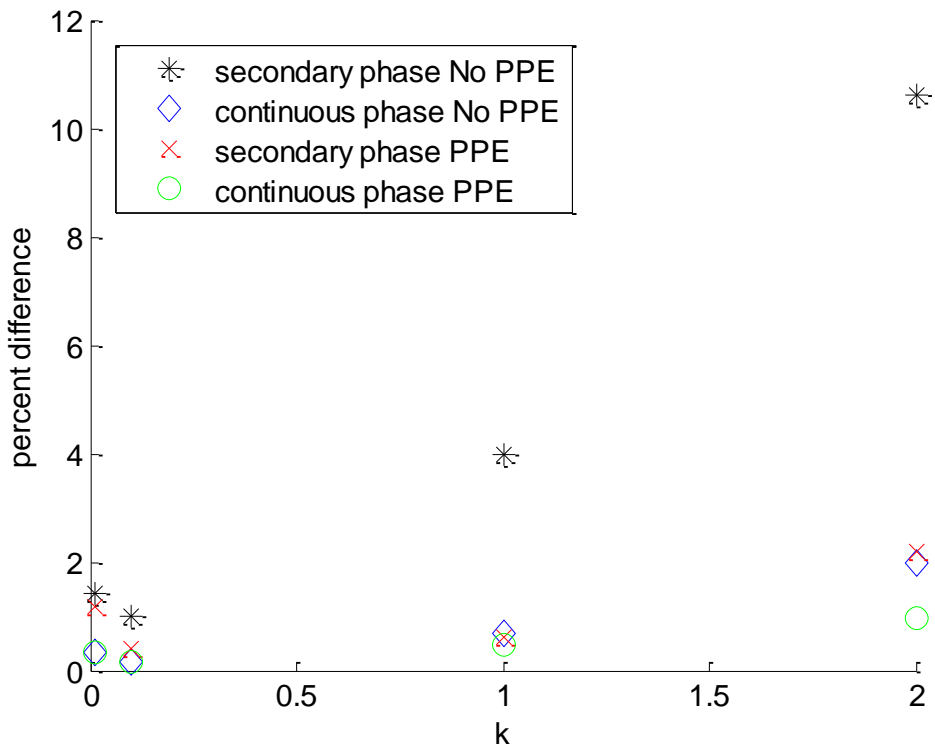


Figure 3.4: Surface Tension Study, $\text{Ma} = 0.00577$, $\text{Re} = 10$, $\rho_1/\rho_2 = 2.0$.

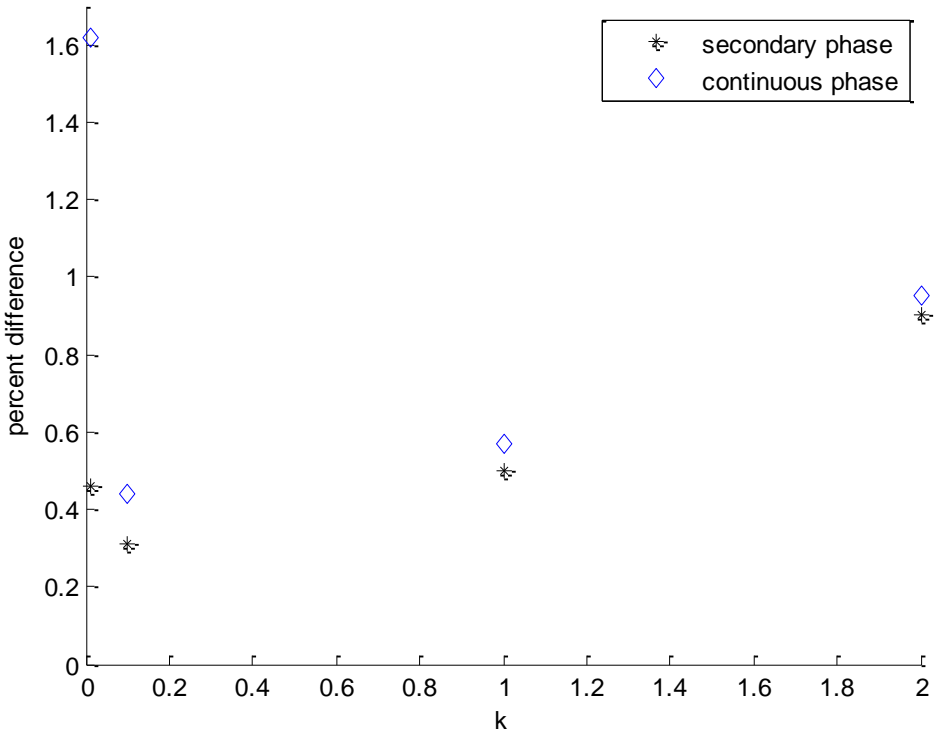


Figure 3.5: Surface Tension Study, $\text{Ma} = 0.00577$, $\text{Re} = 10$, $\rho_1/\rho_2 = 0.5$.

for $k = 0.1$ than for $k = 0.01$ or $k = 1.0$ for example. This suggests that the variation in density owing to the presence of a surface tension force is not solely related to discretization but that the surface tension itself is altering the compressibility of the system²⁸. We may recognize as in the previous section that the PPE substantially reduces the density variation in the lighter phase, while the difference in density variation with and without the PPE for the heavier phase, is less pronounced. Observe now *Figure 3.5* which shows the density variation vs. surface tension magnitude when the dispersed phase is a heavy droplet. While the trend of density variation also presents a local minimum in the droplet density variation curve, the magnitude of the density variation is significantly suppressed, both in the light and heavy phases. Interestingly, the maximum density variation, which occurs in the continuous (lighter) phase for $k = 0.01$, exhibits a density variation of only 1.6%. Further, the *difference* between the droplet and continuous phase density variations for each other surface tension magnitude is quite small and appears to decrease as the surface tension magnitude increases. What is evident from these figures, as will be corroborated in a later section, is that the surface tension has a much greater impact on system density variation, or arguably the system's dynamics itself, when the dispersed phase is a light droplet, compared with a heavy droplet, for the same system density ratio.

3.2.3 Mach Number Study (Cases 16-23)

We examine the effect of Mach number on system density variation. Those results are presented in *Figs 3.6, 3.7*. While in both cases, the lighter phase experiences greater density

²⁸ It is not readily apparent why the system's compressibility would be dependent on the surface tension. It may be speculated that the surface tension will balance the pressure in and outside of interface so as to keep the interface in equilibrium. The tuning of the surface tension therefore, in maintaining a constant radius of curvature must also change the differential pressure, which, through an EOS effects the local density. Perhaps, for some intermediate values of k , this effect is stabilizing with respect to the system's compressibility. As will be observed in the droplet contours later, the assumption of the pressure simply adjusting while the radius of curvature remains fixed will not be sufficient for all cases considered.

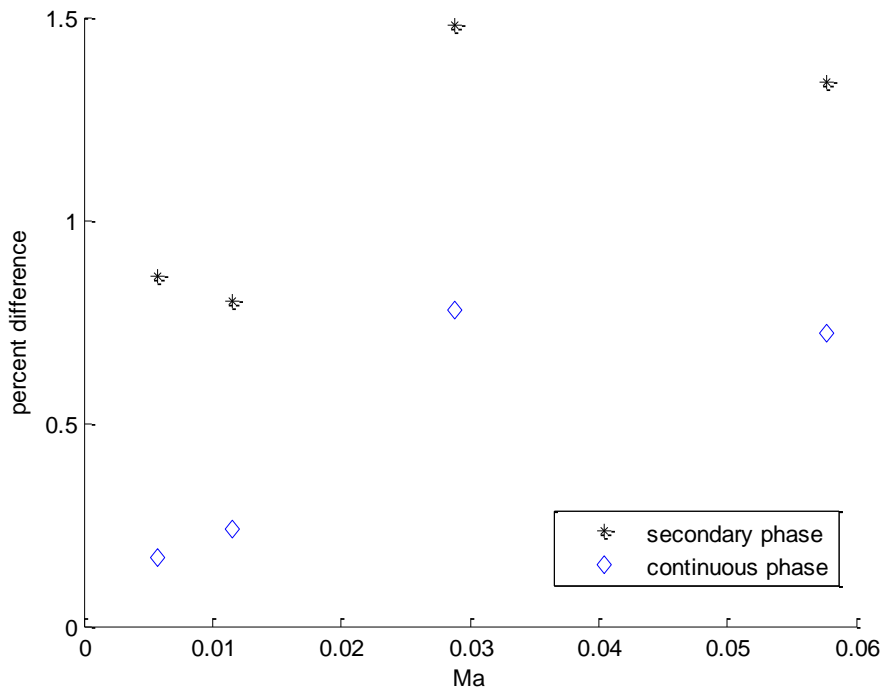


Figure 3.6: Mach number Study, $\text{Re} = 10$, $\rho_1/\rho_2 = 2.0$, $k = 0.1$.

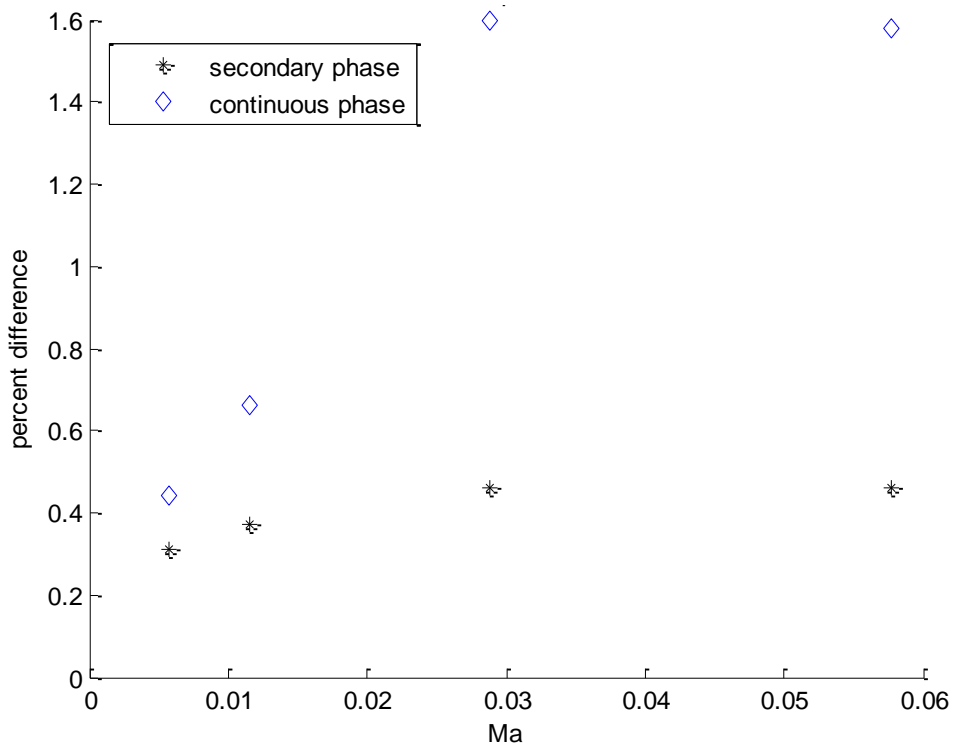


Figure 3.7: Mach number Study, $\text{Re} = 10$, $\rho_1/\rho_2 = 0.5$, $k = 0.1$.

variation compared with the heavier phase, the scaling with Mach number is unclear. The density variation appears to increase in general as the Mach number is increased, but the variation is not monotonic within the range of the cases investigated. What we may say is the Mach number plays a comparatively minor role in density variation, at least within this range of Mach numbers. We may for comparison ask the question of what would be the typical density variation in a single phase flow at the Mach numbers considered. Under steady and isentropic conditions, we may write thermodynamic state variables as a function of Mach number. The variation in density of a gas, compared with the static fluid density, as a result of compressibility effects may be written as [19]:

$$\frac{\rho_o}{\rho} = \left[1 + \frac{\gamma + 1}{2} Ma^2 \right]^{\frac{1}{\gamma-1}} \quad (3.1)$$

Here, ρ_o is the density for a fluid at rest, while ρ is the local fluid density which has changed as a result of compressibility, γ is the ratio of specific heats which is equal to 1.4 for air e.g. Now consider *Figure 3.8* which shows the variation in local fluid density given in equation (3.1) as a function of the Mach number for an ideal gas. Observe that for a Mach number greater than 0.03 in *Figures 3.6* and *3.7*, the density variation is approximately 1.5% for the respective lighter phases. Comparing this density variation, with that due to compressibility effects alone, we observe in *Figure 3.8* that a 1.5% density variation would not occur until the Mach number is 0.18. Therefore, the traditional notion of a Mach number in the LBM formulation may not be appropriate, since its magnitude significantly under predicts the compressibility variation that would be experienced at that Mach number. Rather, a more appropriate Mach number may be estimated empirically *a posteriori* as the effective Mach number (Ma_{eff}), as could be defined

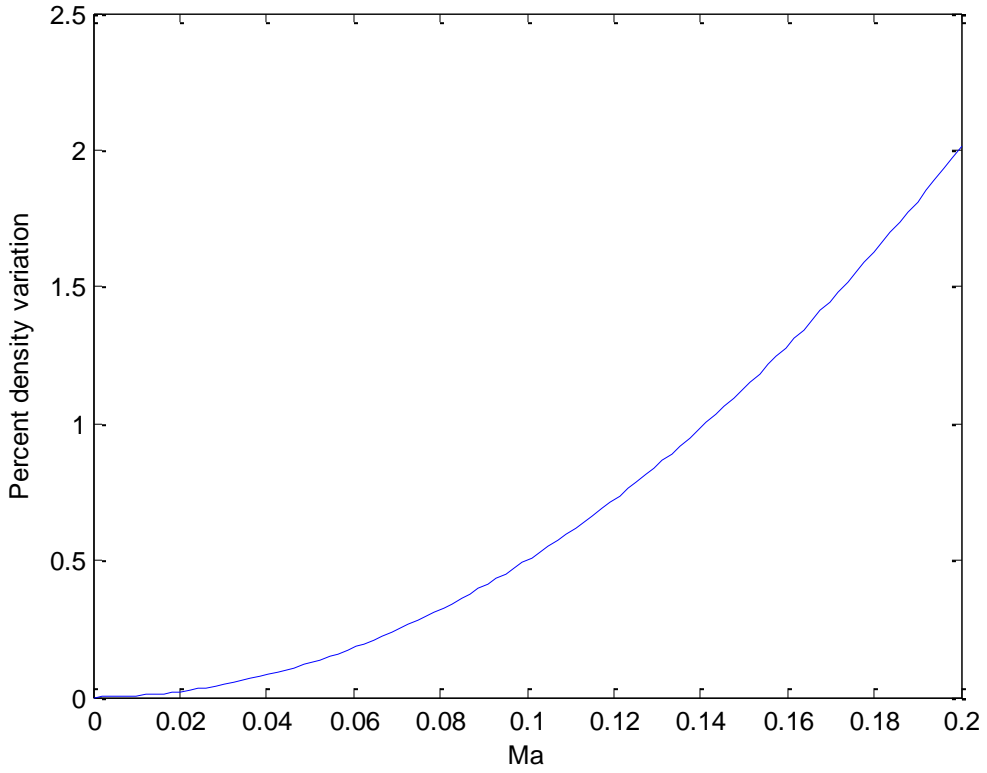


Figure 3.8: Density variation compared with static conditions as a function of Mach number for an ideal gas.

through equation (3.1), that is the Mach number that would be required to generate the density variation observed. We have not performed a systematic study to quantify the density variation at higher Mach number. However, we can remark anecdotally based on observations from computations at higher Mach number that the density variation tends to grow as the Mach number increases. Alternatively, we may say that the traditional assumption of low Mach number as a sufficient criterion for incompressible flow is not necessarily valid since the effective Mach number may be substantially larger than the LBM Mach number. For completeness, it is important to note that the variation in density as a result of LBM Mach number cannot be explained by the difference in definition of LBM Mach number vs. effective Mach number.

The LBM Mach number is typically taken as:

$$Ma = u/c_s \quad (3.2)$$

Where the speed of sound, $c_s = \sqrt{RT}$, so that there is a factor of the square-root of gamma missing from the definition of the LBM Mach number compared with the effective Mach number. The notion of specific heat ratio is not typically found in the LBM context since it may be difficult to measure a specific heat ratio for an arbitrary non-ideal gas (or a liquid modeled as a non-ideal gas). If we assume the fluid behaves approximately like air, with $\gamma = 1.4$, it is not possible to explain the discrepancy between LBM and effective Mach numbers, where the variation, as estimated from the above results is a factor of approximately six.

3.2.4 Reynolds Number Study (Cases 24-29)

We examine the effect of Reynolds number on system density variation while holding density ratio, Mach number, and surface tension magnitude constant. Consider *Figures 3.9* and *3.10*. When the secondary phase is a light droplet, its density variation is observed to increase monotonically and approximately linearly as the Reynolds number is increased while the carrier fluid's density variation appears to be independent of Reynolds number. When the secondary phase is a heavy droplet as in *Figure 3.10*, the density variation appears to increase linearly in both the droplet and carrier phase. As has been observed in previous cases, the lighter fluid experiences the greatest density variation. The dependence of density variation on Reynolds number is relatively modest compared with the dependence on density ratio or surface tension, at least within the range of investigation of the respective parameters.

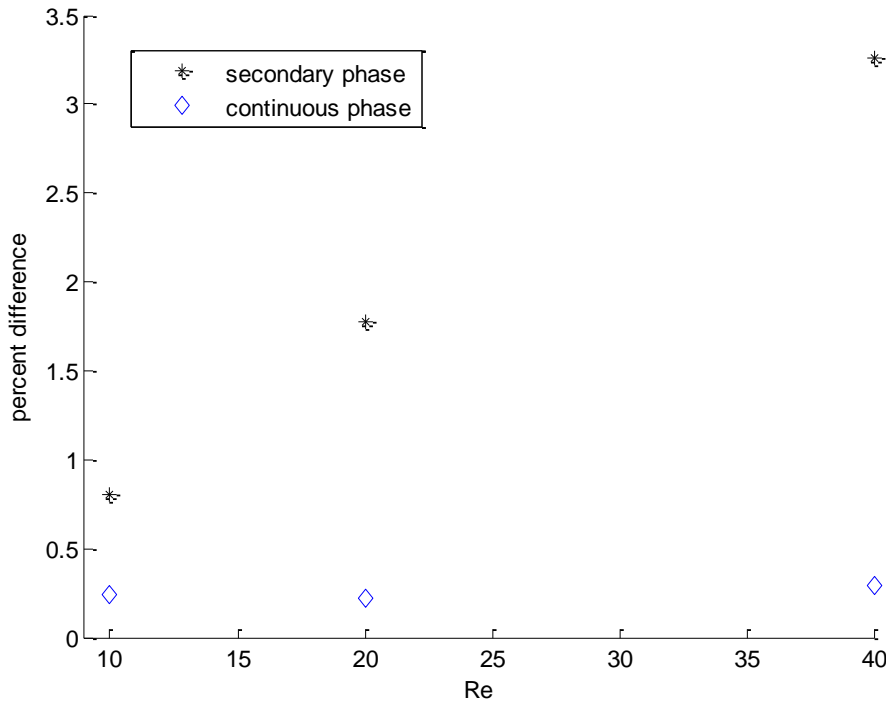


Figure 3.9: Reynolds Number Study, $\text{Ma} = 0.0115$, $\rho_1/\rho_2 = 2.0$, $k = 0.1$.

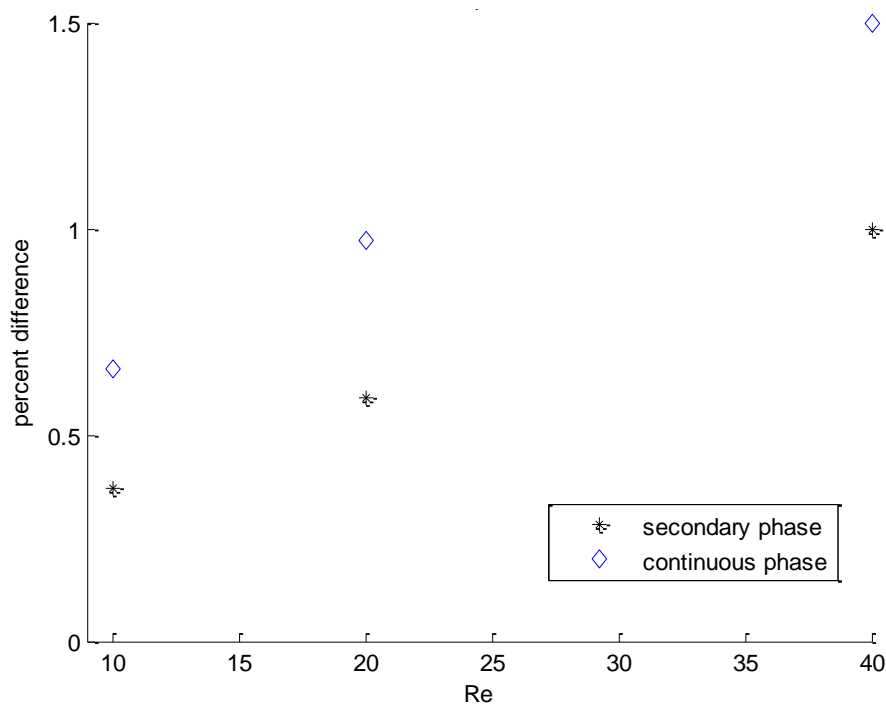


Figure 3.10: Reynolds Number Study, $\text{Ma} = 0.0115$, $\rho_1/\rho_2 = 0.5$, $k = 0.1$.

3.2.5 Density Contours for Surface Tension Study (Cases 8-15)

To conclude Chapter 3, we present a series of density contours to demonstrate the effect of surface tension on system dynamics. *Figures 3.11-3.14* show the evolution of droplet density contours in time as the surface tension parameter is increased. Similar results are presented in *Figures 3.15-3.18*, except the secondary phase in these cases are heavier droplets. Observe in *Figure 3.11* that at a small value of k (surface tension magnitude), the light droplet experiences significant deformation. As the surface tension is increased to $k = 0.1$ in *Figure 3.12*, we observe reduced deformation. Higher values of surface tension were also considered in *Figures 3.13* and *3.14*. However, in these cases, the surface tension caused the system to become increasingly unstable. Regarding *Figures 3.13* and *3.14*, we note the light droplet increases in size with time. This is not a result of deformation but rather the density variation likely generated by spurious currents as discussed previously. However, as we observed earlier, the surface tension seems to have a much smaller effect on density variation in the heavy droplet compared with the light droplet. Over a wide range of k (surface tension) values, we observe both little density variation and volume change in the heavy droplet.²⁹

Finally, we emphasize in *Figure 3.19* that the addition of a PPE, while having a significant effect on the system's density variation, also strongly affects the system's dynamics. In *Figure 3.19*, we note that without the PPE, the light droplet, while significantly deformed, has not broken up. With the addition of the PPE, the light droplet does break up³⁰.

²⁹ Of course, we would expect the greatest density variation to occur in the lighter carrier phase for the heavier droplet cases, but in this phase also, no density variation is apparent.

³⁰ The reason for this is not clear and the following explanation is only speculation. It can be observed that the pressure correction has re-distributed “energy” from some form of system compressibility, and transformed that into shear work on the droplet interface. The increased effective shear (or Capillary number alternatively) deformed the droplet interface enough to cause break-up. For this reason, it is possible that an LBM simulation at *non-unity* density ratio may under-predict the system Capillary number, that is, the relative importance of viscous and interfacial stresses.

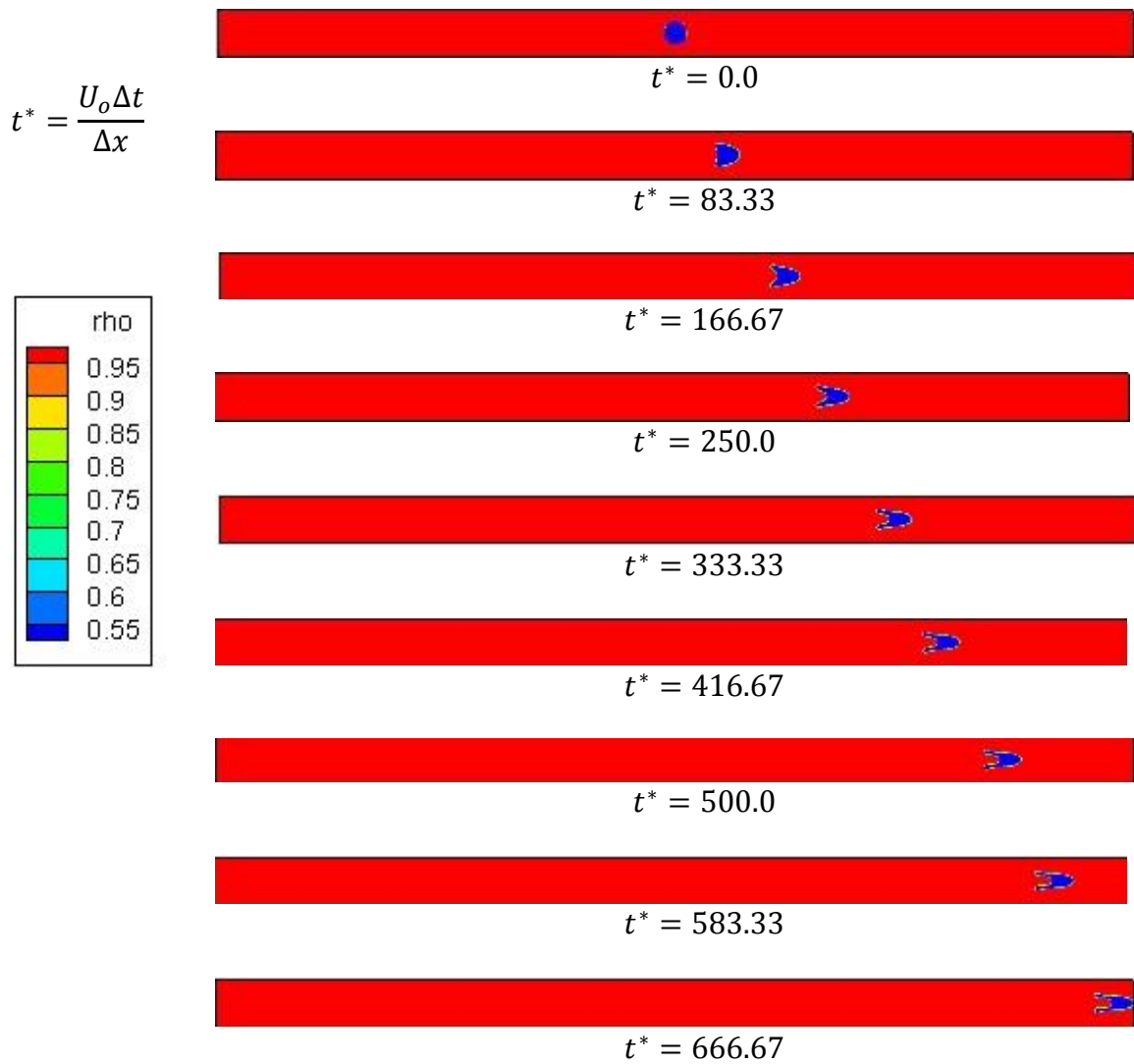


Figure 3.11: Case 8a: $\text{Re} = 10$, $\text{Ma} = 0.00577$, $\rho_1/\rho_2 = 2.0$, $k = 0.01$.

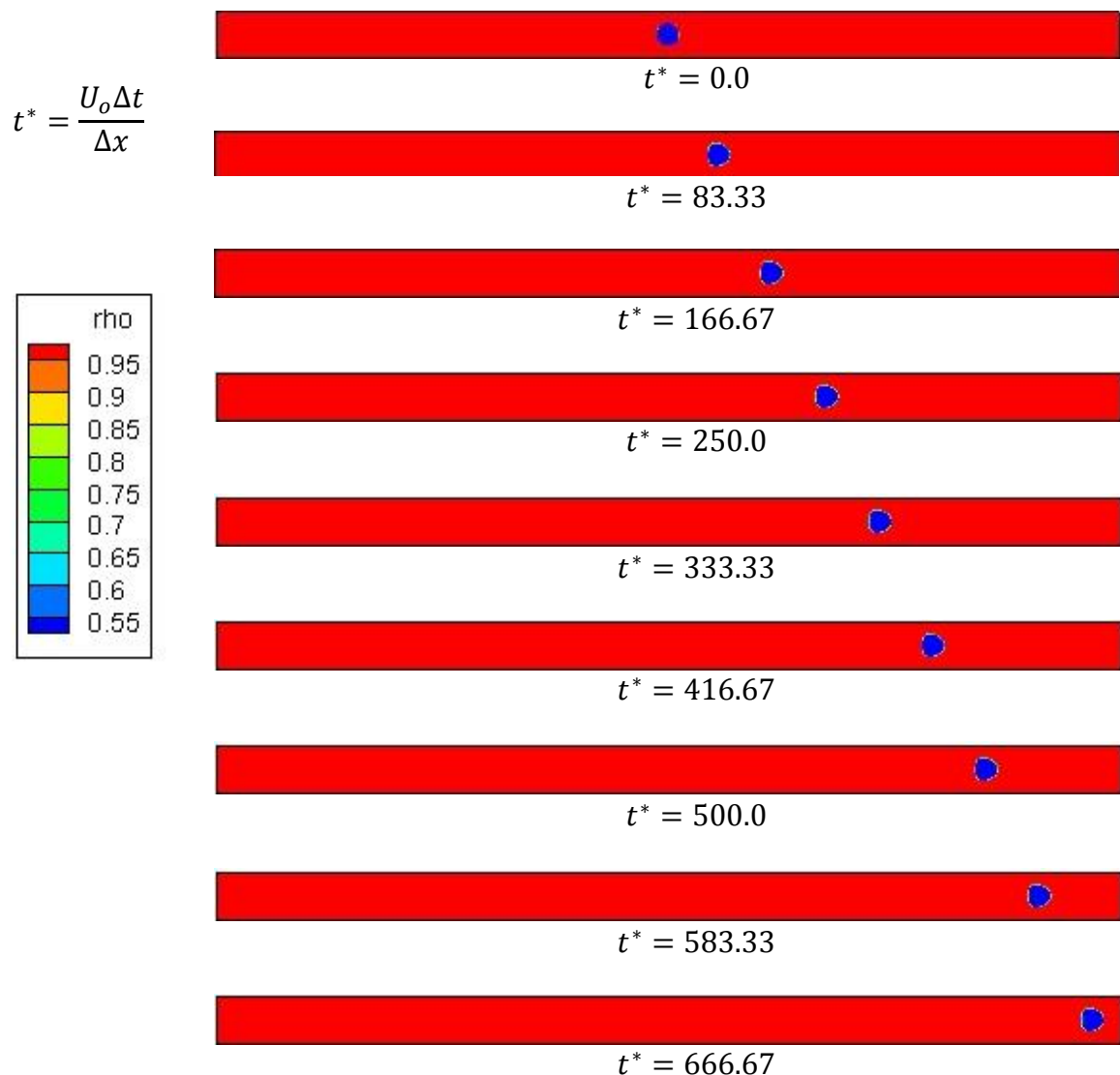


Figure 3.12: Case 9a: $\text{Re} = 10$, $\text{Ma} = 0.00577$, $\rho_1/\rho_2 = 2.0$, $k = 0.1$.

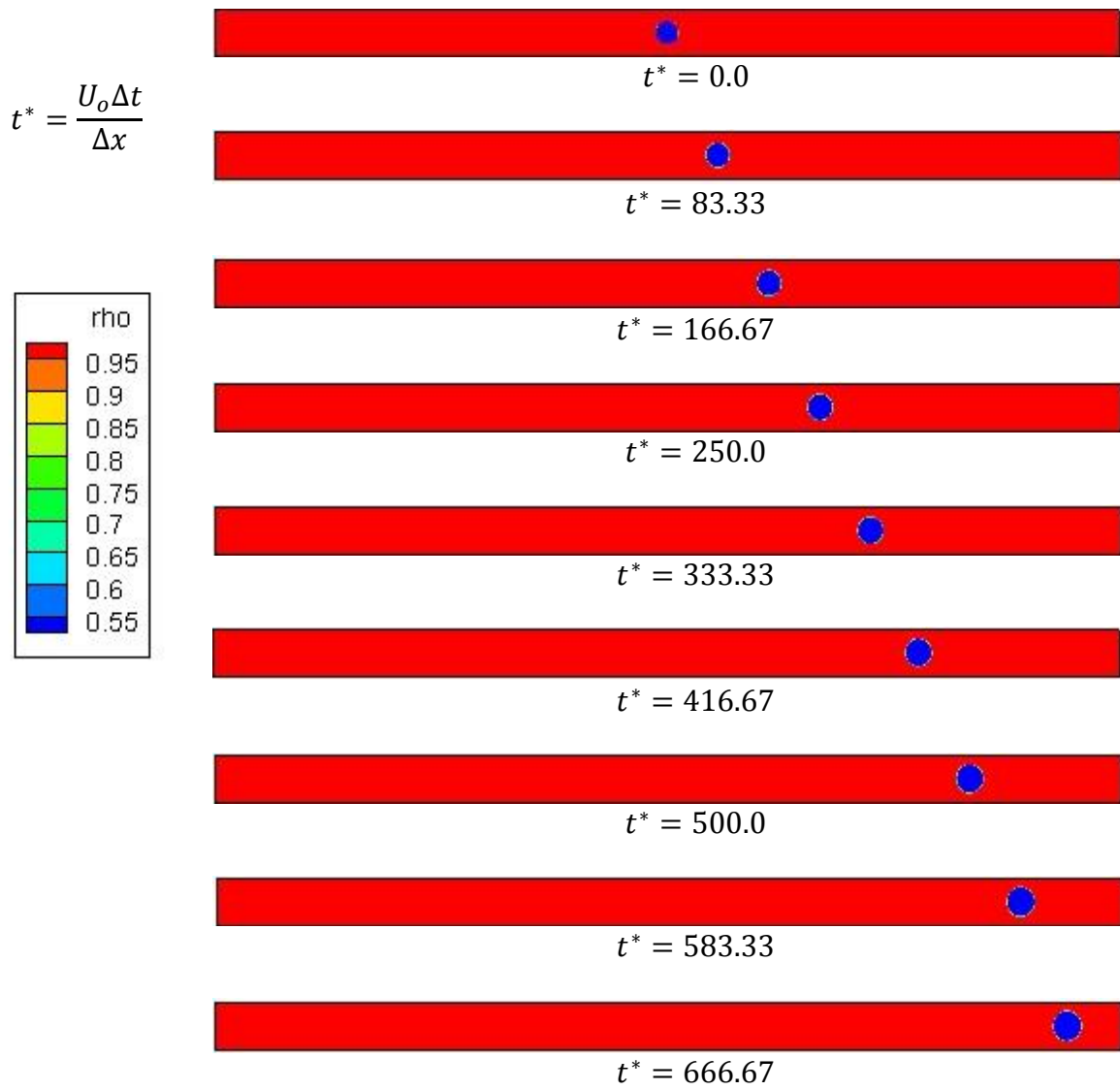


Figure 3.13: Case 10a: $Re = 10$, $Ma = 0.00577$, $\rho_1/\rho_2 = 2.0$, $k = 1.0$.

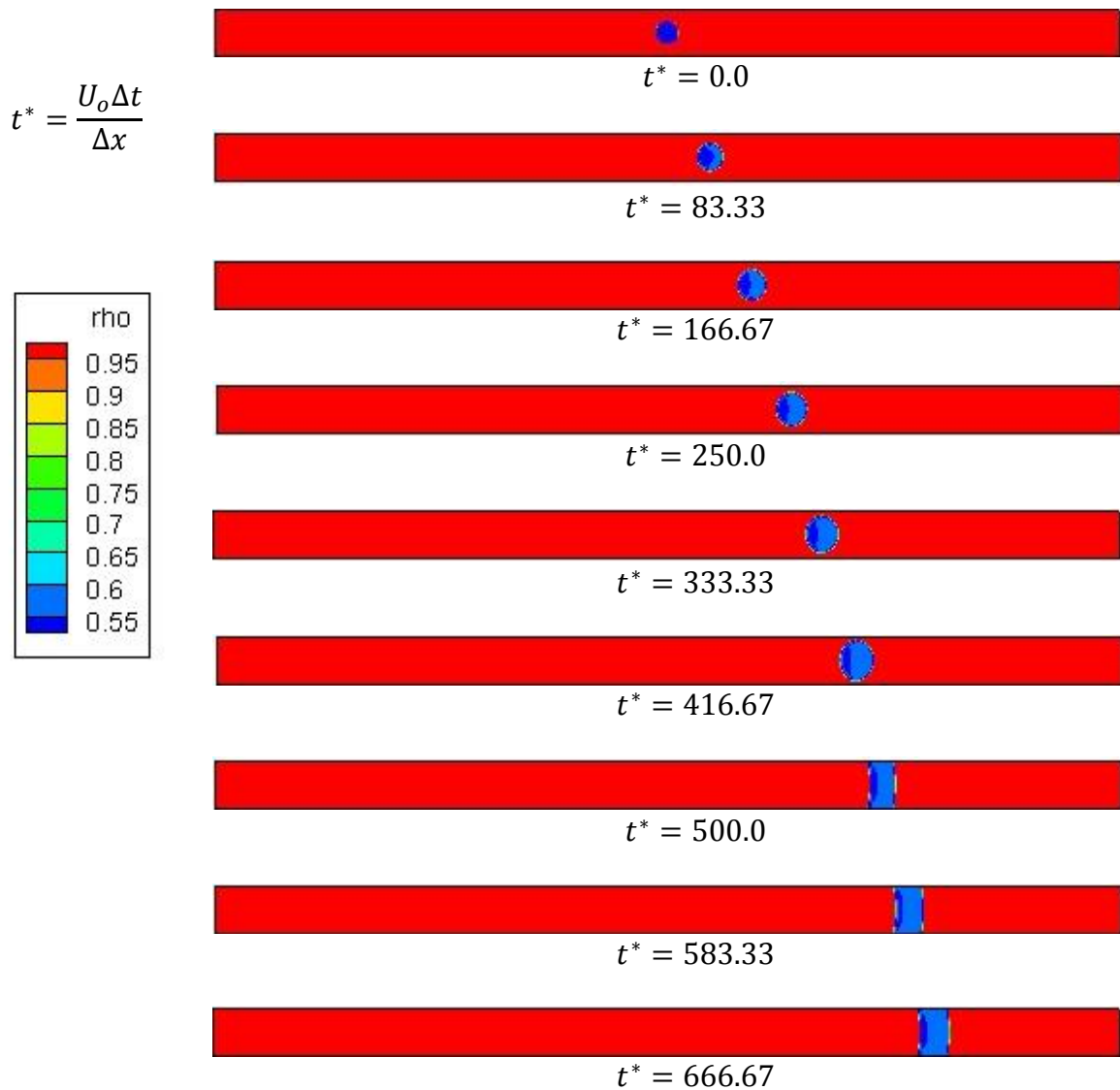


Figure 3.14: Case 11a: $\text{Re} = 10$, $\text{Ma} = 0.00577$, $\rho_1/\rho_2 = 2.0$, $k = 2.0$.

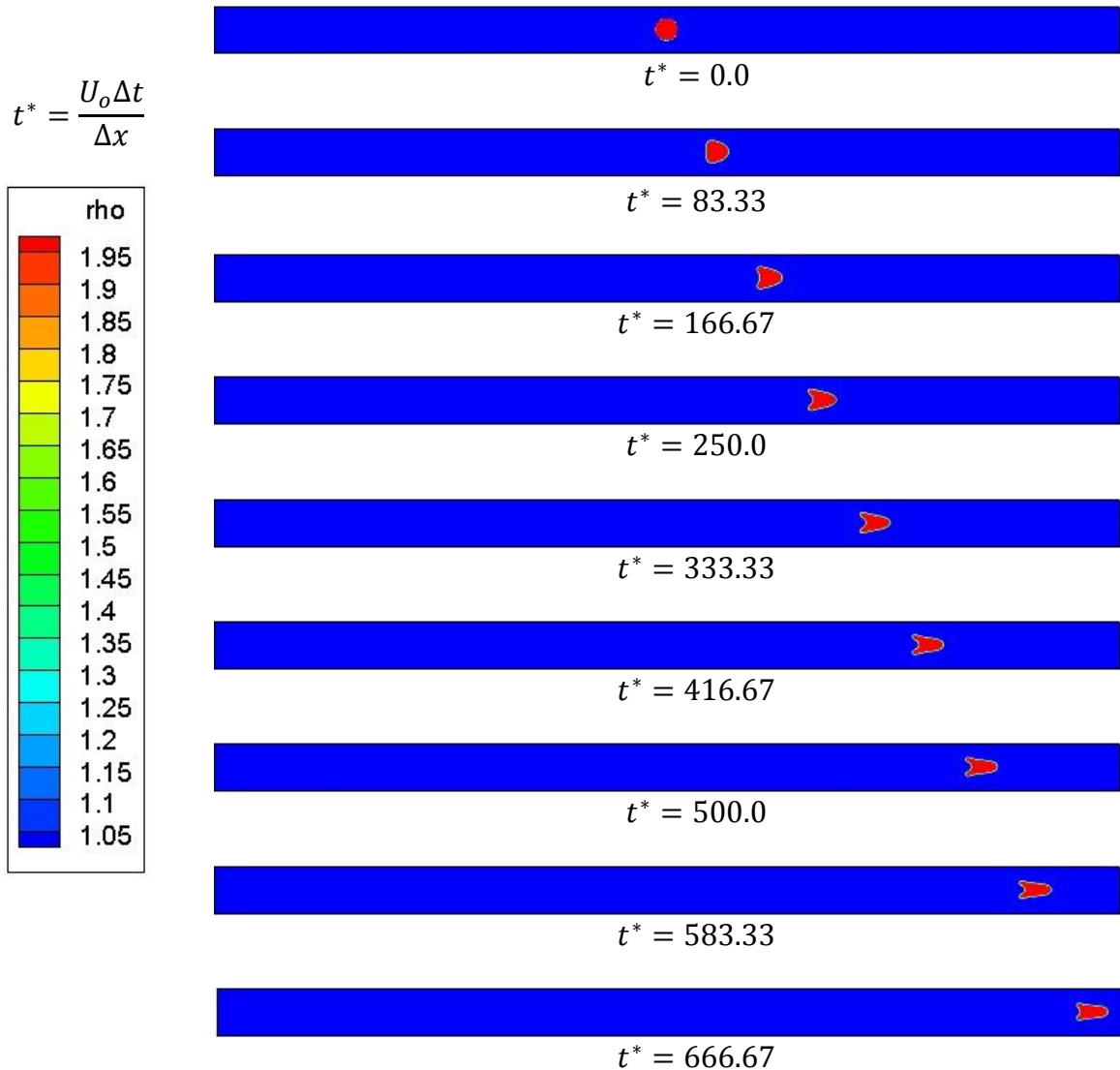


Figure 3.15: Case 12a: $\text{Re} = 10$, $\text{Ma} = 0.00577$, $\rho_1/\rho_2 = 0.5$, $k = 0.01$.

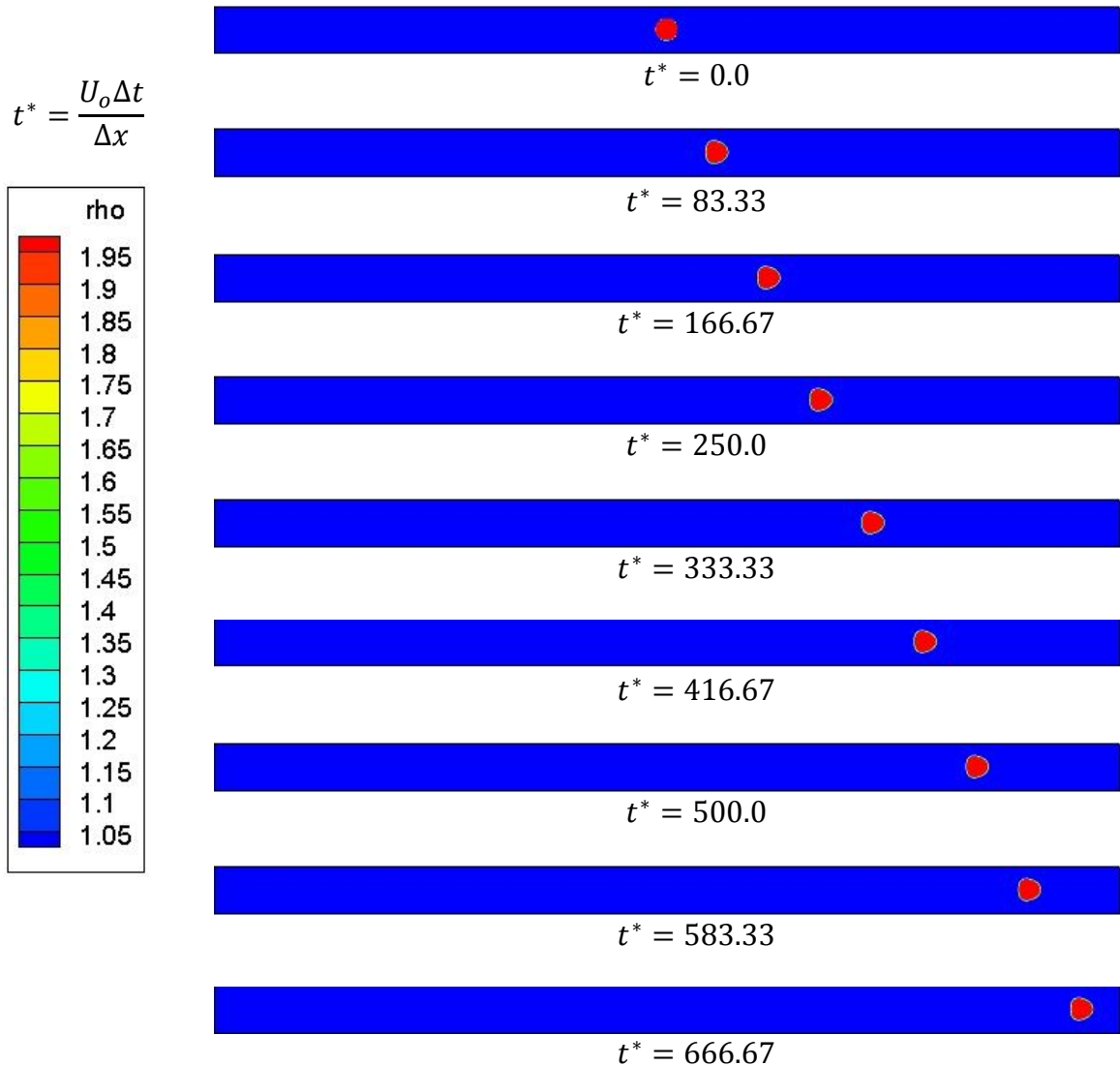


Figure 3.16: Case 13a: $\text{Re} = 10$, $\text{Ma} = 0.00577$, $\rho_1/\rho_2 = 0.5$, $k = 0.1$.

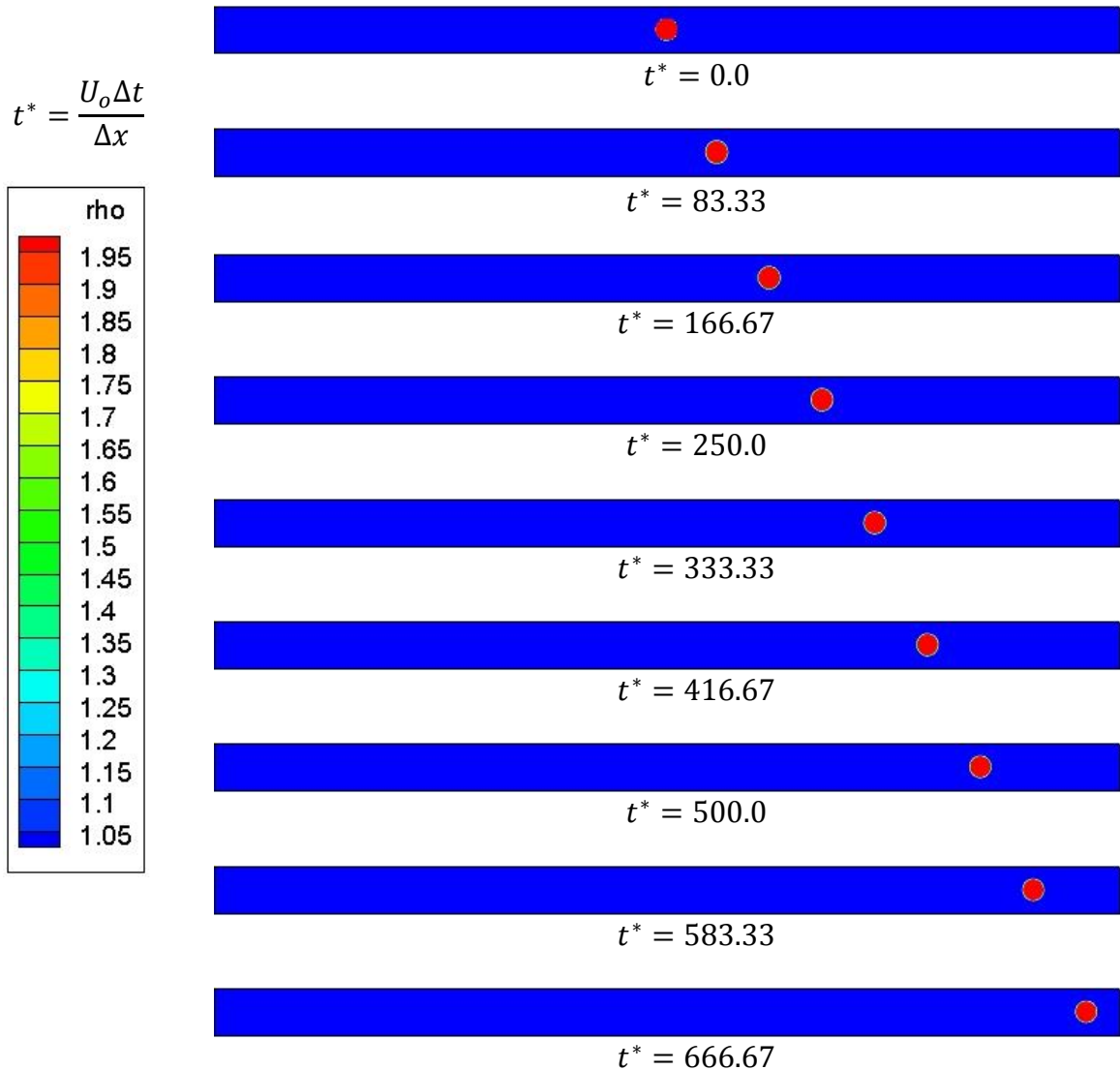


Figure 3.17: Case 14a: $\text{Re} = 10$, $\text{Ma} = 0.00577$, $\rho_1/\rho_2 = 0.5$, $k = 1.0$.

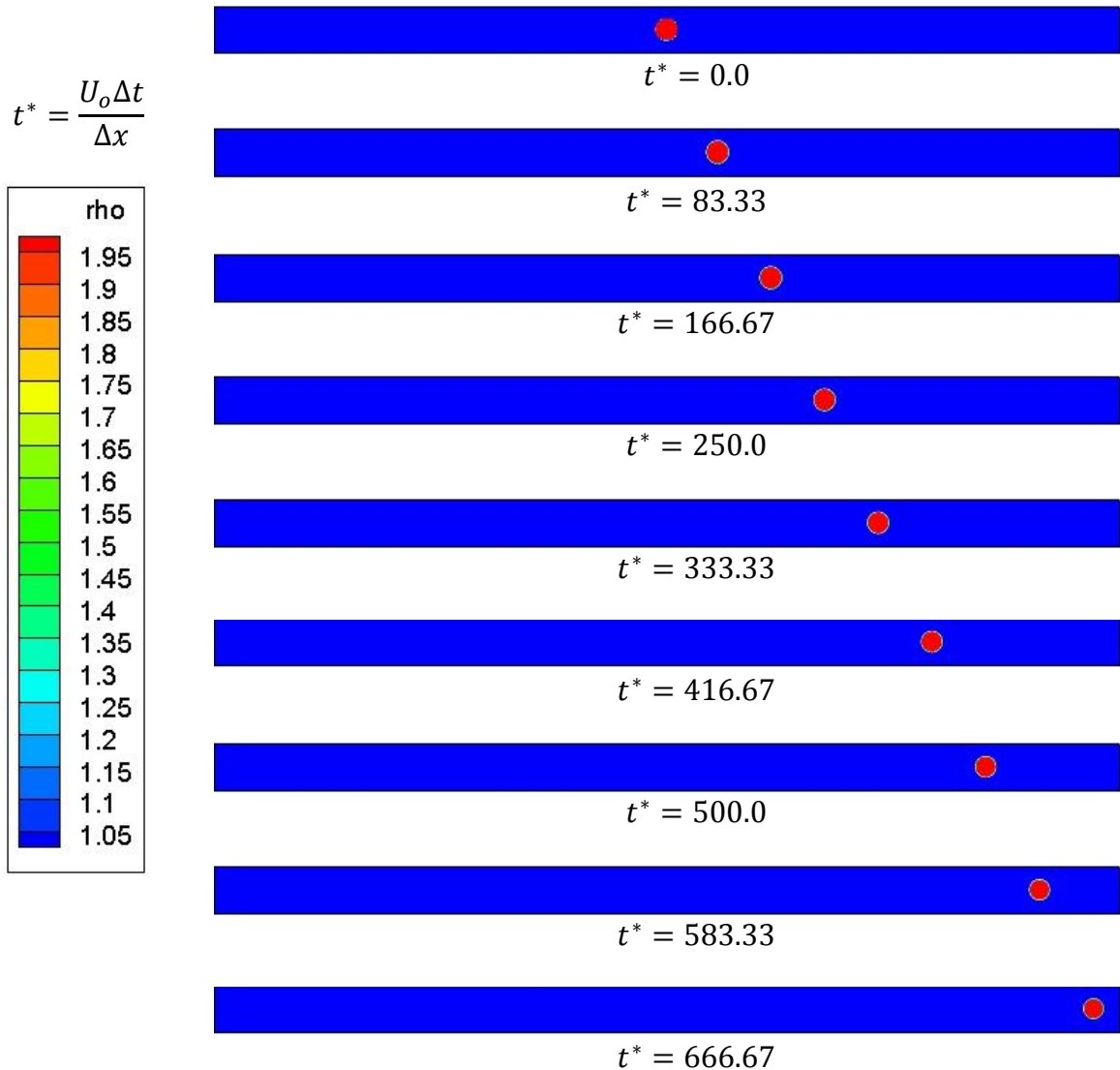


Figure 3.18: Case 15a: $\text{Re} = 10$, $\text{Ma} = 0.00577$, $\rho_1/\rho_2 = 0.5$, $k = 2.0$.

$$t^* = \frac{U_o \Delta t}{\Delta x}$$

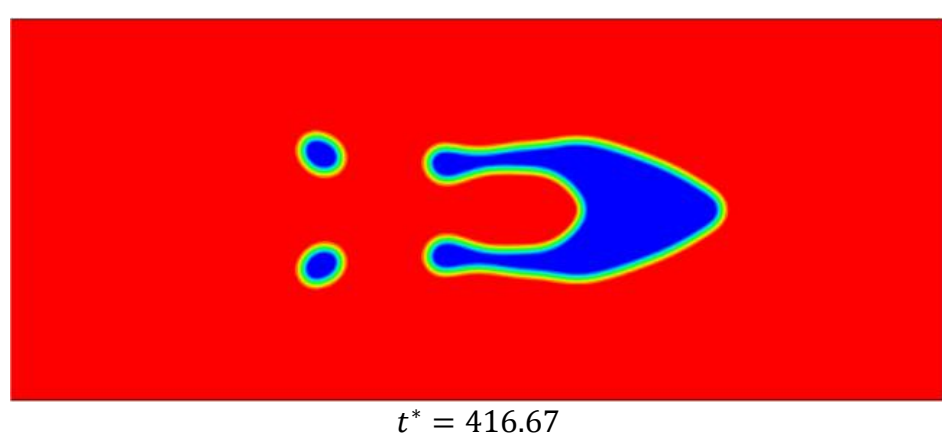
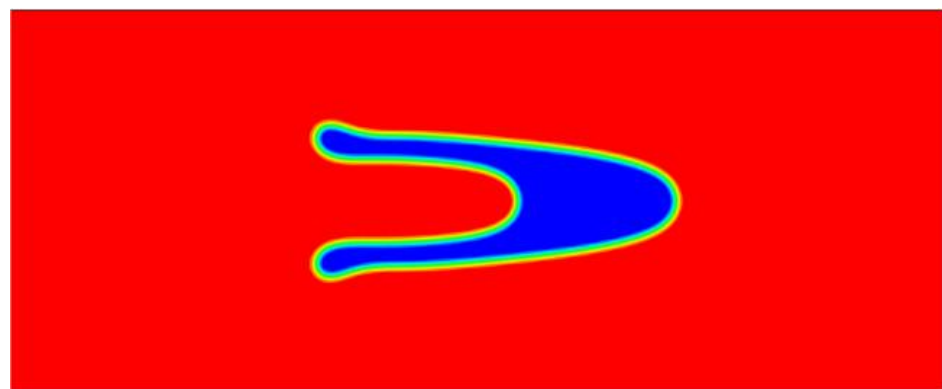
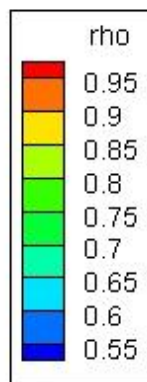


Figure 3.19: Case 8a: $Re = 10$, $Ma = 0.00577$, $\rho_1/\rho_2 = 2.0$, $k = 0.01$, top: without PPE equation, bottom: with PPE equation.

4. SIMULATION OF DROPLET IMPINGEMENT AND COLLISION

4.1 Problem Description

The problem of a droplet interacting with one or multiple droplets in an unbounded or semi-bounded domain is encountered in a number of applications ranging from fuel injection and atomization in an internal combustion engine to condensation on surfaces of varying material properties. In a heat exchanger, saturated water vapor may condense into liquid water droplets which may collect on the walls of the channels within the apparatus. Local accretion of liquid water may then alter the boundary conditions locally, since the boundary, as seen by the global flow, is some mixture of a solid which mandates a no-slip Dirichlet condition, and a liquid surface which imposes a constraint on the tangential velocity gradient (a Neumann condition). Since multiphase flows in these settings are inherently unsteady and often turbulent, local changes in boundary conditions may have dramatic consequences for the flow regime as a whole.

When two or more droplets interact in the absence of a boundary, the interaction is typically referred to as collision.³¹ When one or more droplets, travels a non-zero distance and strikes a surface, the interaction is described as impingement³². There exists a vast literature regarding these topics and our purpose here is not to present a comprehensive review. Rather, we mention a few papers relevant to these topics with the purpose of evincing some of the key physics present in these problems.

³¹ Of course two droplets in an un-bounded domain may interact without colliding, where lubrication pressure keeps them apart, for instance, or in the presence of a charge gradient where Coulomb forces become important. In this investigation, we assume the conditions are appropriate for a collision to occur.

³² We investigate only smooth, solid, regular surfaces. By smooth, we mean no roughness. By solid, we mean non-porous so the no-slip condition is assumed valid. By regular, we mean simple geometries, typically flat. Of course, it is possible to explore arbitrarily complex boundaries. We attempt to capture some of the salient physics even with the constraints on surfaces we investigate.

We begin our brief review of droplet impingement work with a seminal study done by Chandra and Avedisian [54] in 1991. Chandra and Avedisian presented a thorough investigation of impingement of liquid n-heptane droplets onto flat stainless steel surfaces. Surfaces that were both dry and covered by a thin film of liquid were investigated. The key parameter varied was the surface temperature. Chandra and Avedisian also identify the Weber number (We), (i.e. the ratio of inertial to interfacial stresses) as an important parameter, although We was not varied in this study. Droplet spreading rate was independent of temperature for small times, but for larger times, droplets impacting on cool surfaces experienced greater spreading than droplets on warmer surfaces. Chandra and Avedisian capture the evolution of droplet impact, subsequent spreading, and in many cases break-up of the liquid droplets. Dynamic fluid-solid contact angle



Figure 4.1: Definition of Contact Angle.

is evident in these photos, where the contact angle, which describes a droplet's wetting properties, is defined in *Figure 4.1*. Zero contact angle corresponds to complete wetting of a liquid droplet, while contact angles greater than 180 degrees correspond to non-wetting droplets. Typically, droplets with contact angles less than 90 degrees are termed hydrophilic since they are relatively more wetting than the surrounding fluid. Droplets with contact angles greater than 90 degrees are referred to as hydrophobic. That static contact angle may be described analytically by Young's equation [69]:

$$\cos(\theta) = \frac{\sigma_{sg} - \sigma_{sl}}{\sigma_{lg}} \quad (4.1)$$

Here, σ_{sg} , σ_{sl} , and σ_{lg} , are respectively the solid-gas, solid-liquid, and liquid-gas interfacial tensions. Gu, Gupta, and Kumar [69] and Gupta and Kumar [2, 5] performed lattice Boltzmann simulations of droplet impingement over a range Reynolds and Weber numbers. Droplet spreading was independent of both of these parameters for short times, but significant variation in spreading was observed at later times as these parameters were independently varied. Gu et al. [69] also found a spreading dependence on contact angle. For a fixed Weber and Reynolds number, Gupta and Kumar [5] showed an impinging droplet may or not break-up depending on the contact angle. At a Weber number of 114, and a Reynolds number of 152, a hydrophilic droplet did not break-up, but the neutrally wetting ($\theta = 90^\circ$) and hydrophobic droplets did break-up. Additional work was carried out by Lee and Lin [65] who used a modified LBM scheme to examine droplet impingement on a liquid film for a liquid to surrounding gas density ratio of 1000.

Gu et al. [69] also studied droplet collisions and identified the Weber number, the Reynolds number, and an impact parameter (representing relative droplet positions in the case of oblique collisions). Inamuro et al. [64] performed lattice Boltzmann simulations of droplet collisions and explored an Impact Parameter-Weber Number parameter space. Different types of collisions were classified and mapped into this space. Inamuro et al. [64] identified three collision regimes: coalescence, where no break-up occurred after collision, reflexive separation, where break-up occurs post coalescence during a relaxation stage, and stretching separation, where break-up occurs post coalescence and the majority of the total mass is moving away from the center of mass. In mapping these types of collisions into the parameter space, Inamuro et al. [64] found good agreement with theoretical boundaries of these different collision regimes. In a later study, Inamuro et al. [63] explore binary droplet collisions and examine the mixing rate

using tracer particles. Mixing rate (a percentage) is defined as the fraction of the each droplet's mass that has been transferred to the other once droplets separate following collision and coalescence. For a Weber number of 80, no mixing is observed for zero or high impact parameter (level of collision obliqueness), but for intermediate impact factor, as much as 30% mixing was observed. Later, Sakakibara and Inamuro [14] showed that in the case of unequal size droplets, the mixing may occur even at zero impact factor, and that the rate of mixing carries a Weber number dependence. Remarkably, for Weber numbers of 40 and 50, the smaller droplet experienced zero mixing rate, that is, it received no mass from the larger droplet. However, at these values of Weber number, the larger droplet did receive mass from the smaller one.

4.2 Results

4.2.1 Droplet Impingement Results

We explore several model problems to assess the ability of LBM in simulating droplet impingement. Because droplet contact angle is critical to impact dynamics, we have chosen the S-C algorithm to simulate the impingement problems since no forcing term has been proposed (to the best of our knowledge) that models the effect of relative wettability within the context of the H-C scheme.

The effect of contact angle can be discernible by examining *Figure 4.2*. A liquid droplet surrounded by a lighter liquid impinges on a smooth surface. The density ratio ρ_2/ρ_1 and viscosity ratio $\lambda = \mu_2/\mu_1$ between the droplet and surrounding liquid are both 2. The domain is 600x1000 l.u. The initial droplet height is two l.u. above the solid boundary and the initial droplet velocity is 0.10 l.u./s. Fluid-solid interaction forces (i.e. $G_{n\bar{n}}$) were varied to yield different static contact angles. Both simulations depicted in *Figure 4.2* are identical with the exception of the prescribed contact angle. The droplet-surface contact angle in the left panel is smaller than that in the right panel indicating the droplet in the former case is relatively more wetting than the droplet in the latter case. At each time step, the left droplet has experienced more spreading compared with the right droplet. This is indicative of each droplet's own proclivity to spread based on its own wettability, as determined by the contact angle. The droplet-solid attraction is relatively high between the droplet and solid surface shown in the left panel which causes more droplet mass to stay in the neighborhood of the surface and less to be reflected into the outstretched fingers. In contrast, large bulbs form for the case in the right panel. The droplet in this case is relatively less attracted to the solid boundary; therefore, less mass will stay close to the solid surface. This mass is then available to accumulate in the fingers as shown in *Fig. 4.2(l)*.

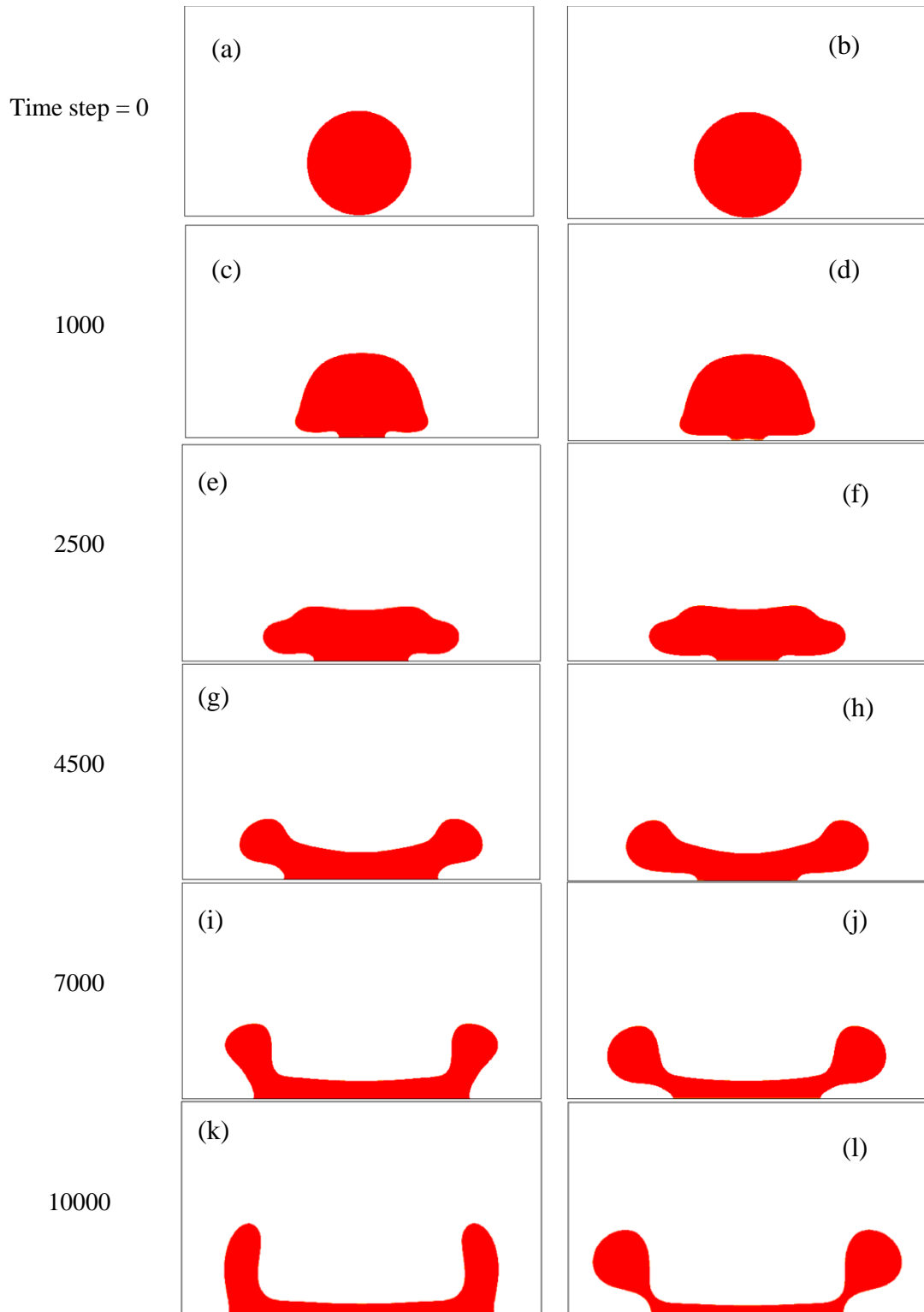


Figure 4.2: Droplet impingement on a smooth surface, $\theta = 27^\circ$ (left) and $\theta = 82^\circ$ (right).

We have also explored the effect of introducing a textured surface into our simulations to study the effect of surface roughness of impingement and wetting dynamics. Rahman and Jacobi [34] showed that by introducing micro-grooves into a smooth aluminum surface, it was possible to significantly increase the contact angle for a liquid water droplet. Kim et al. [76] performed LBM simulations of droplets on textured surfaces and found a variation in contact angle as the texture spacing was varied. Above a critical distance between pillars, the droplet rest state transitioned from a Cassie-Baxter state [1], where in regions devoid of pillars the droplet mass does not rest within the void space, to the opposite case referred to as the Wenzel state [51], where part of the droplet mass fills the void space between subsequent pillars.

Now consider *Figure 4.3*, where a liquid droplet surrounded by a lighter liquid impinges onto a textured surface. The droplet to surrounding fluid density and viscosity ratios are both 2. The domain is 300x500 l.u. Fluid-solid interaction forces were varied such that each solid boundary, including the textured grooves were hydrophilic surfaces. The droplet moves downward with an initial velocity of 0.20 l.u./s corresponding to a Reynolds number of 180 for a distance of two l.u. before striking the textured surface. The impact of the droplet results in significant spreading and ultimately break-up of the droplet. Observe the dome regions *Figure 4.3c*. This may be attributed to large lubrication pressure built up in these small gaps. Following break-up, the droplet continues to spread wet much of the textured and surrounding flat surfaces. The center daughter comes to rest in a Cassie-Baxter state.

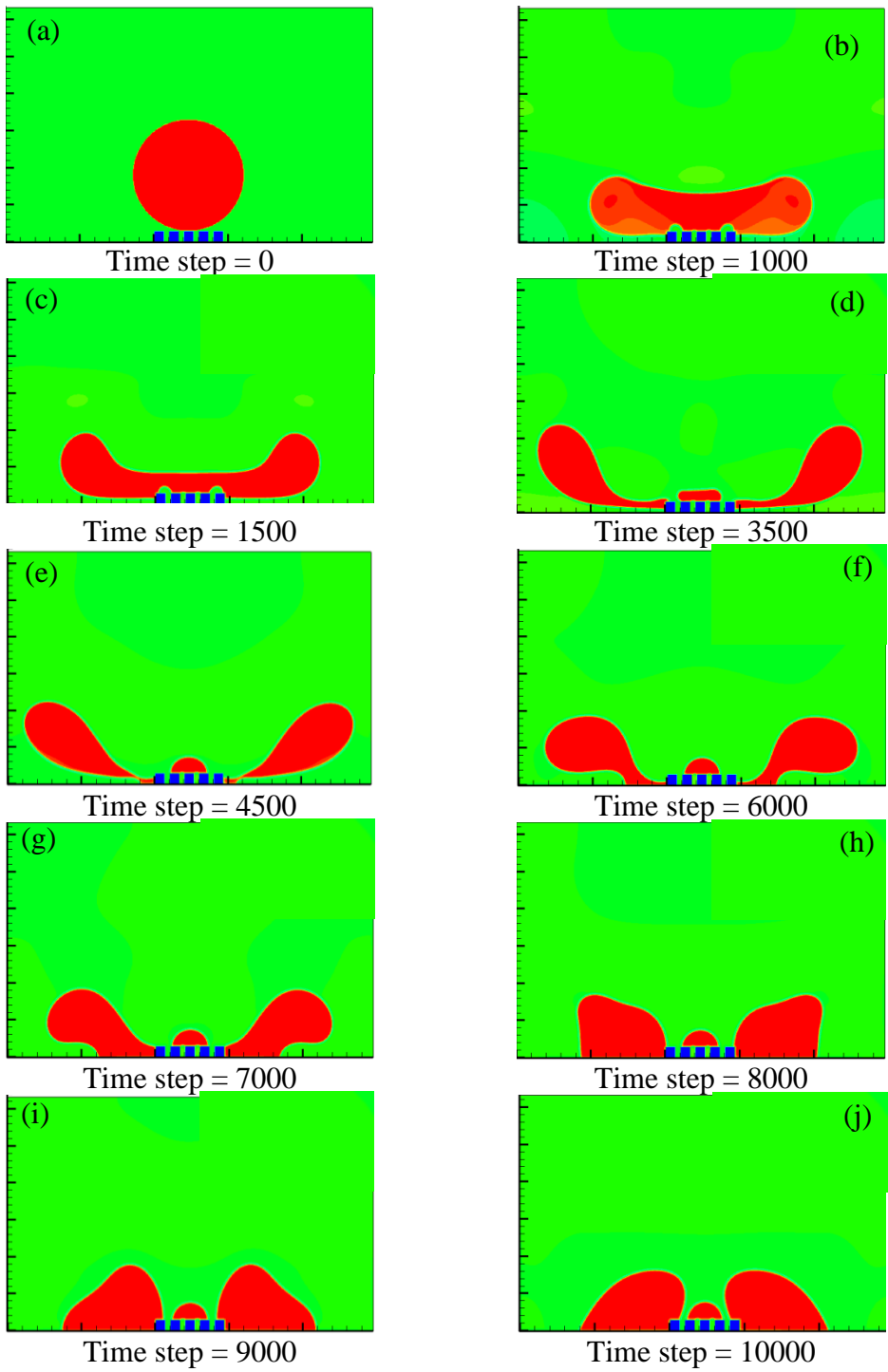


Figure 4.3: Droplet impingement on a textured surface, $\rho_h/\rho_l = \lambda = 2.0$, $Re = 180$.

In *Figure 4.4*, we compare the dynamics of between impingement on a smooth surface and a liquid film. The liquid to vapor density and viscosity ratios are the same in both cases and are equal to 60 and 120 respectively. Each droplet begins with a downward velocity of 0.05 l.u./s. The simulation domain is 200x400 for the smooth surface case and 400x800 for liquid film case. Fluid-surface forces have not been considered for these cases so that the static contact angle will be 90 degrees. As the droplet makes contact with the smooth surface, vertical translating kinetic energy is transferred to lateral spreading. The amount of spreading is finite since the relatively high droplet viscosity resists its own deformation. Eventually, the droplet retracts back and oscillates towards an equilibrium hemispherical shape. The relaxation toward a hemispherical shape is attributed to surface tension, which was present in these simulations, but not directly calculated. Its value however may be estimated by calculating the Laplace pressure difference in and outside a static droplet of the same material properties. We see a similar transfer of energy from the droplet to the liquid. In this case, the droplet Reynolds and Weber numbers are low enough such that splashing does not occur. As the wave resulting from impingement spreads, its amplitude decreases as a result of viscosity. After long times (greater than that depicted in *Figure 4.4h*) the liquid film slowly retracts towards a level height.

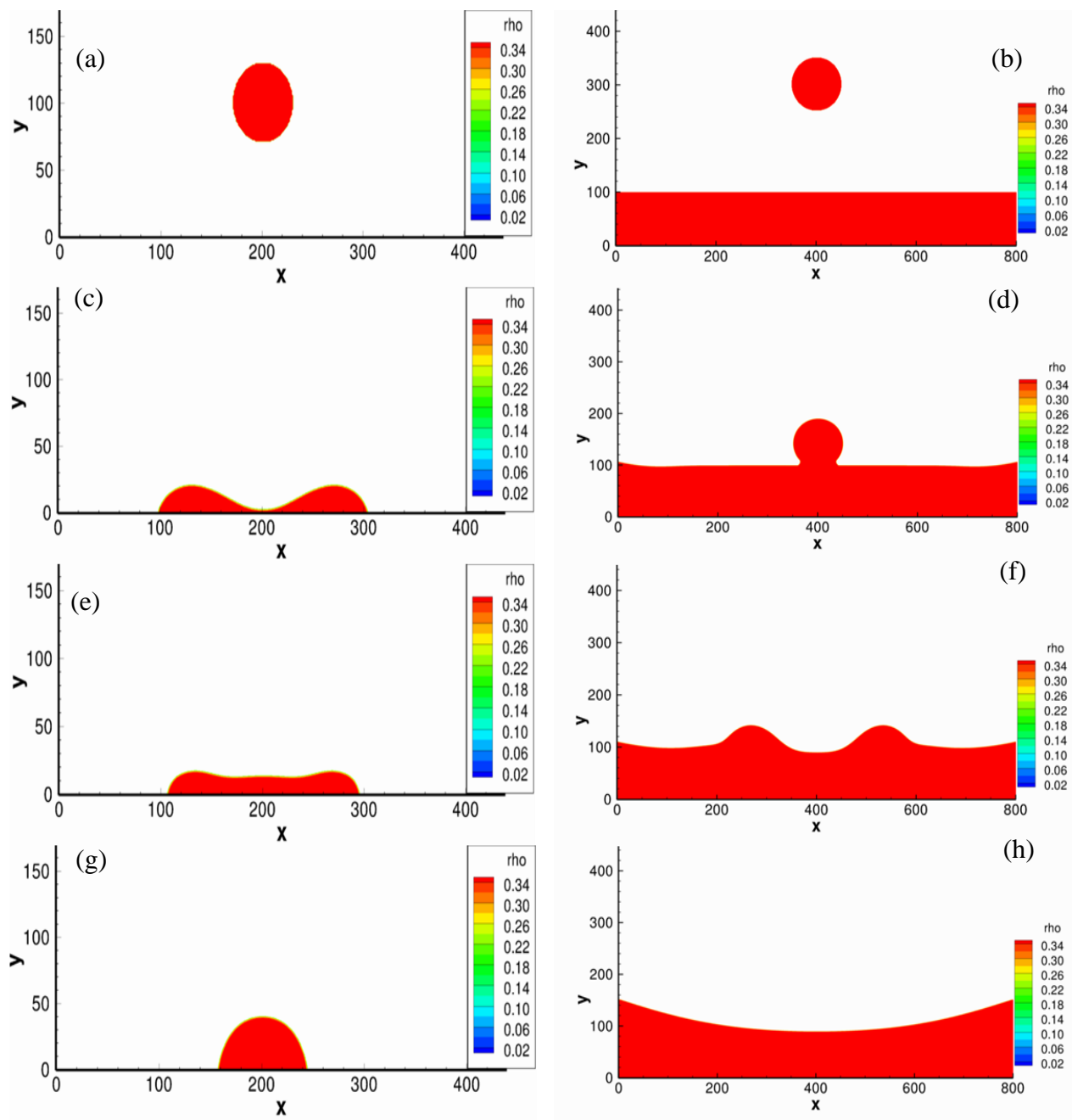


Figure 4.4: Droplet impingement on a solid surface (left), and liquid pool (right)
 $\rho_h/\rho_l = 60$, $\lambda = 100$, droplet velocity = 0.05 l.u./s.³³

³³ Results obtained jointly with Purushotam Kumar.

A similar study of droplet impingement on a smooth surface is shown in *Figure 4.5*. The liquid and gas have the same density ratio as the fluids in the cases presented in *Figure 4.4*. However, the viscosity ratio is 120 for the case shown in *Figure 4.5*. The domain is 200x200x200 l.u. The droplet begins with a downward velocity of 0.05 l.u./s. The droplet undergoes moderate spreading following impingement, however no necking is observed near its center. Following damped spreading, the droplet relaxes toward an equilibrium shape due to interfacial tension. Because the material properties and initial conditions were identical between the smooth impingements in *Figures 4.4* and *4.5*, this suggests that impingements in two and three-dimensions are fundamentally different processes. The lack of necking may also be attributed to a higher viscosity ratio in the three-dimensional impingement case.

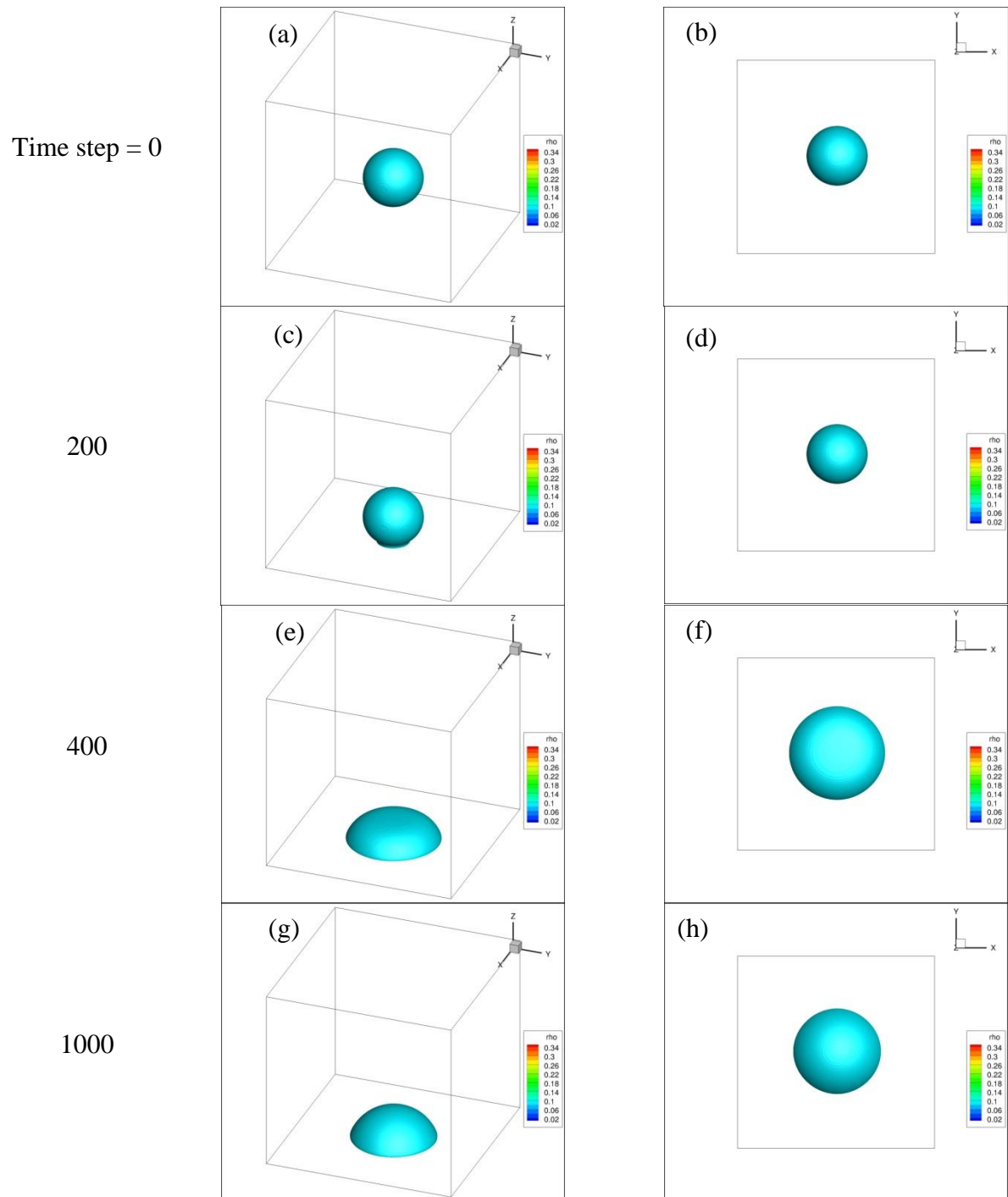


Figure 4.5: Droplet impingement on a smooth surface, isometric (left) and top view (right), $\rho_h/\rho_l = 60$, $\lambda = 120$, droplet velocity = 0.05 l.u./s.³⁴

³⁴ Results obtained jointly with Purushotam Kumar.

4.2.2 Droplet Collision Results

In *Figure 4.6*, we examine two binary droplet collisions, in the absence of gravity, where the viscosity ratio is varied between the two cases. Simulations are performed using the S-C method. The liquid to vapor viscosity ratio is 100 for the case shown in the left panel of *Figure 4.6*, while the viscosity ratio is 120 for the case in the right panel. The liquid to vapor density ratio is 60 in both cases. The simulation domain is 400x800 in both cases. The initial relative approach velocity of the droplets is 0.05 l.u./s. In both cases, the vertical kinetic energy is transferred into lateral kinetic energy following the collision. A period of necking ensues in both cases. The necking period is finite and damped due to viscosity, and the budded masses eventually relax towards each other. Interestingly, in the lower viscosity ratio case, the buds briefly break up before colliding again. This type of break-up was referred to as reflexive separation by Inamuro et al. [64]. The resulting mass following the second collision oscillates with decreasing amplitude toward a steady spherical shape. In the higher viscosity case, there is also significant necking observed. However, the increased viscosity of the droplets relatively to the surrounding fluid apparently resists deformation just enough to avoid a secondary break-up and subsequent collision. In this case, necking and relaxation lead to a damped oscillation toward a steady spherical shape.

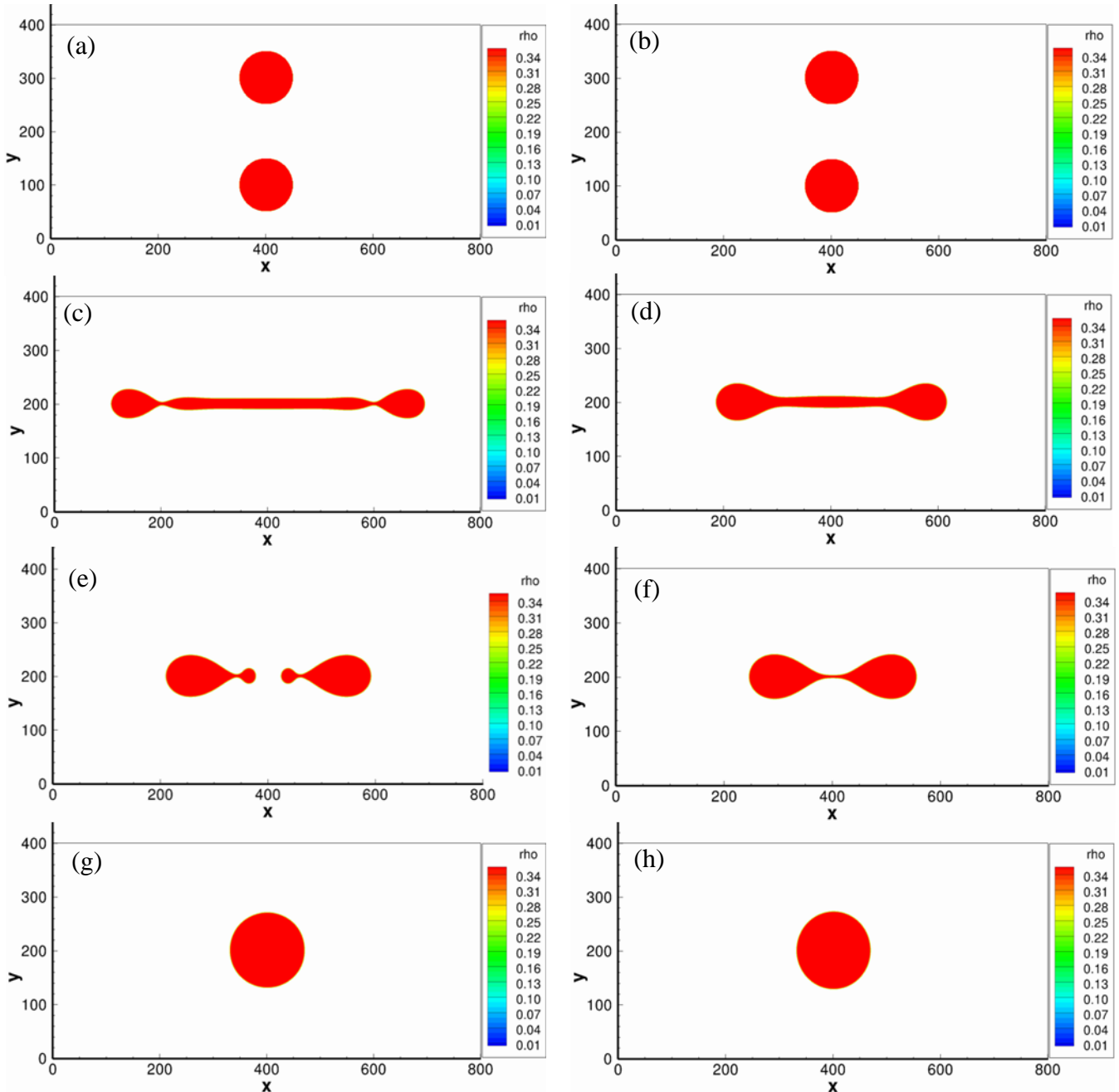


Figure 4.6: Two droplets approach with identical velocity, collide and coalesce. density ratio = 60, viscosity ratio = 100 (left) and 120 (right), droplet velocity = 0.05 l.u./s.³⁵

³⁵ Results obtained jointly with Purushotam Kumar.

We also explore the case of oblique droplet collision in *Figure 4.7*. Each droplet begins with a vertical velocity magnitude of 0.20 l.u./s. The direction of each droplet's initial velocity vector is oriented in a direction pointing toward the other droplet. The diameter of each droplet is 80 l.u. The liquid to vapor density and viscosity ratios are both 70. The domain is 300x300x300 l.u periodic cube. In the case presented in the left panel of *Figure 4.7*, the azimuthal angle is 0° and the polar angle is 73.3°. Following collision, both droplets coalesce and begin rotating clockwise w.r.t. the x-axis. In the second case, the azimuthal angle is varied to 45°, while the polar angle is fixed. The resulting collision is comparatively glancing and results in temporary coalescence followed by a period of necking and break-up. While the resulting buds eventually impinge on the domain boundaries and interact with each other due to the periodic conditions, in an ideal unbounded domain, we expect these droplets to continue traveling away from each other and to have no interaction following the initial collision event.

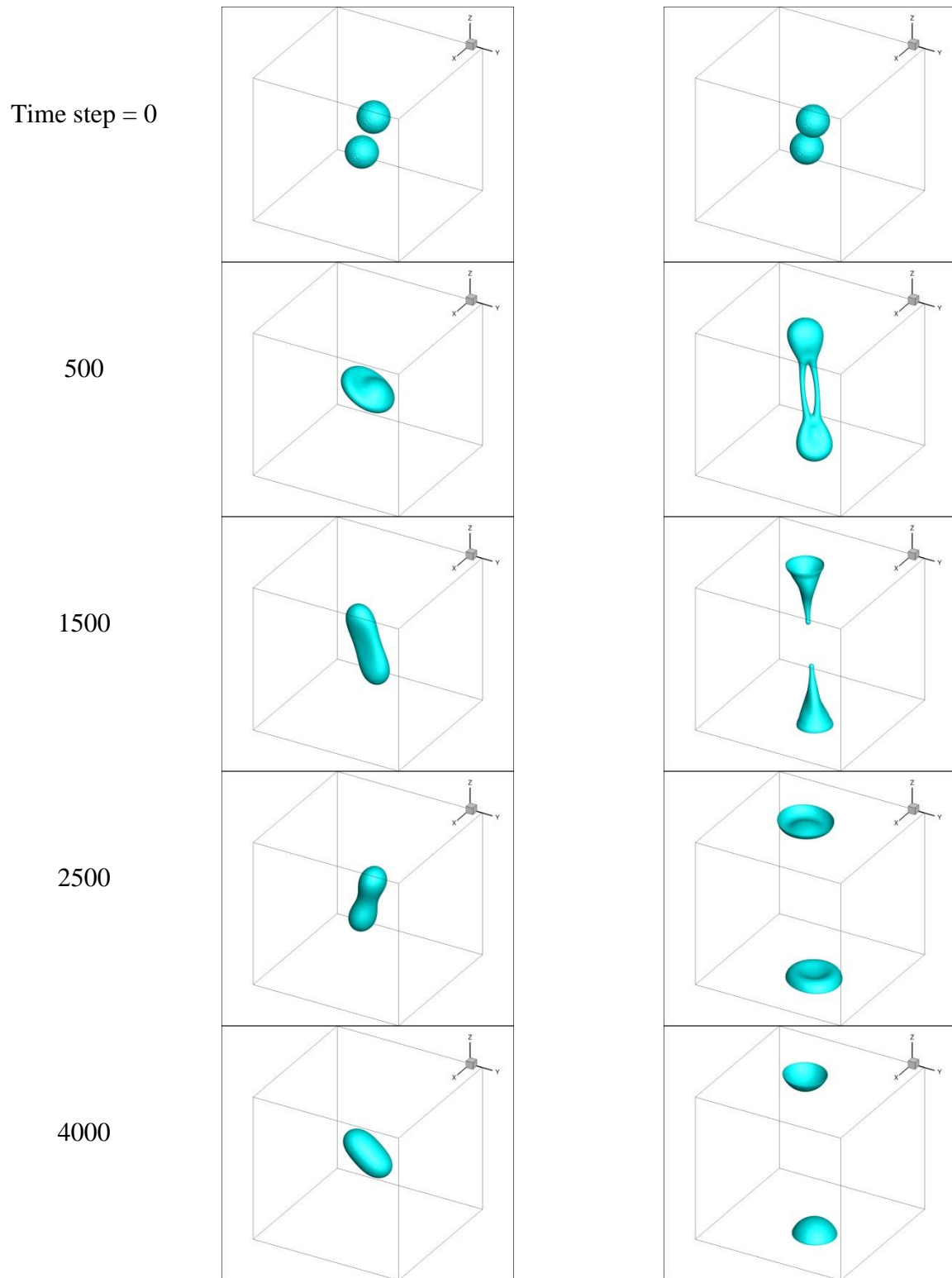


Figure 4.7: Oblique binary droplet collision, $\zeta = 0^\circ, \varphi = 73.3^\circ$ (left), $\zeta = 45^\circ, \varphi = 73.3^\circ$ (right).³⁶

³⁶ Results obtained jointly with Purushotam Kumar.

5. SIMULATION OF FLOW IN MICRO-CHANNELS

5.1 Problem Description

Multiphase flow in micro-channels has many applications to air conditioning and refrigeration including phase mixing or separation in T-junctions and distributor headers. The distribution of phases within the micro-channels of a shell and tube heat exchanger could have a substantial effect on the efficiency of heat transfer, that is, the effective heat transfer coefficient. In many of these applications, multiple fluids (water, oil, refrigerant, air), or phases of the same fluid (liquid water and water vapor) are present which may significantly increase the complexity of the flow regimes encountered.

In this chapter, we explore a variety of multiphase micro-channel problems including two-dimensional displacement flows as well as droplet formation in complex micro-channels. There is an extensive literature with regard to these problems which allows a careful assessment of LBM to be made with regard to simulating these types of flows. Upon evaluating LBM's performance, it will be possible in the future to examine more complicated flows including three-dimensional geometries, and phase change.³⁷

Recently, following a similar study of buoyancy-induced mixing by Sahu and Vanka [31], Redapangu et al. [48] studied immiscible displacement flow in channels using the H-C method. More recently, Mishra et al. [37] simulated miscible displacement flow in a channel and examined the dependence of flow stability properties on double-diffusive effects. In [48], channel inclination was varied to examine the dependence of gravitational effects on the types of fingering behavior observed. The other key parameters investigated were the Capillary number and the viscosity ratio between the two fluids. As the angle of inclination was increased from

³⁷ LBM can be naturally extended to allow phase change by incorporating an energy equation coupled with an EOS.

zero (a horizontal channel) to nearly vertical, the interface between the displacing fluid finger and the displaced fluid became increasingly corrugated. The finger experienced very jagged edges at high capillary numbers and relatively smooth edges for low Capillary numbers. This was in agreement with the findings of Sahu and Vanka [31] that observed a decrease in interfacial mixing as the capillary number decreased. Returning to Redapangu et al.'s study [48], as the displaced fluid's dynamic viscosity was increased relative to the displacing fluid, high frequency interfacial instabilities were suppressed, which revealed lower frequency corrugations independent of viscosity ratio.

The problem of droplet flow in micro-channels, specifically of droplet formation in T-junctions has been studied by many authors. Several authors including [4, 3, 6, 68, 32] simulated droplet formation in a T-junction using LBM. The case of droplet formation in cross-junctions was considered by Yu et al. [79]. Recent seminal investigations include work by Garstecki et al. [44] and De Menech and Garstecki et al. [36]. Omebere-Iyari and Azzopardi [42] developed a flow regime map for two-phase flow in micro T-junctions and found that flow regimes could be demarcated when plotted as function of both the liquid and gas superficial velocities. This observation suggests an important non-dimensional parameter in studying droplet formation in T-junctions is the flow rate ratio, that is the ratio of flow rates of two single phase fluids entering two respective branches of a T-junction may be correlated with the two-phase flow regime that results in the third branch of the T-junction. Garstecki et al. [44] showed that the length of droplets formed in T-junctions scaled linearly with the flow rate ratio. This observation was in agreement with simulations performed by Gupta and Kumar [3]. Gupta and Kumar [4] also showed that the gas to liquid viscosity ratio as well as the ratio cross-sectional area between inlet and outlet branches may vary the flow regime in the outlet branch from jetting to slug formation

depending on the flow rate. For low viscosity ratios ($\lambda < 1/30$), [3] observed slug formation independent of the flow rate ratio, while for a viscosity ratio 1/10, jetting was observed as the flow rate of the dispersed phase became comparable to the continuous phase flow rate. Gupta and Kumar [6] observed nominal variation in normalized droplet volume for capillary numbers greater 0.3 independent of the flow rate ratio, however, for capillary numbers less than or equal to 0.1, normalized droplet volume varied inversely with the capillary number independent of the flow rate ratio. In addition, the flow rate ratio has a more pronounced effect on droplet size for low capillary numbers, and a comparatively modest effect as the capillary number was increased. Qian et al. [16] found a moderate effect of liquid-surface contact angle on droplet length. In an alternating liquid-gas slug flow, when the liquid contact angle was greater than 120 degrees, liquid and gas slug lengths were nearly identical, while for smaller contact angles, gas slug lengths were longer than liquid slugs, with the difference in length increasing as the liquid contact angle was decreased.

5.2 Results

5.2.1 Displacement Flow Results

We present results for displacement flow in a two-dimensional channel in *Figures 5.1* and *5.2*. Simulations were performed using the H-C method (no PPE). We examine the effect of Atwood number ($At = \frac{\rho_1 - \rho_2}{\rho_1 + \rho_2}$) on displacement flow dynamics in *Figure 5.1*. Only horizontal (gravity-less) channels are considered in the following cases. Following [48], we use a simulation domain of 4608x98 nodes. Lighter liquid enters from the left and pushes a heavier liquid already present in the channel. The Atwood number in the first case (left panel) is 0.5 while the Atwood number in the second case is 0.85. The viscosity ratio of the heavier to lighter fluid is equal to 20 in both cases. The inlet is prescribed a fully developed velocity profile with an average velocity of 0.025 l.u./s. As the displacing fluid pushes the displaced fluid from the channel, corrugations are observed at the finger interface. However, the corrugations are more pronounced for the lower At number case (left panel) compared with the higher Atwood number case (right panel). However, despite small amount of displaced fluid entrained in the light viscous finger of the $At = 0.5$ case, the corrugations in both cases are relatively low frequency, which may be attributed to the high viscosity ratio as discussed in [48]. Interestingly however, there exist no discernible corrugations for the case shown in *Figure 5.2* despite the relatively low Atwood number and viscosity ratio. However, these results are in good agreement with a similar case presented in Fig. 6a of [48]. Interestingly, Sahu and Vanka [48] show that for the case of $At = 0$, increasing the viscosity serves to introduce corrugations, albeit low frequency ones.

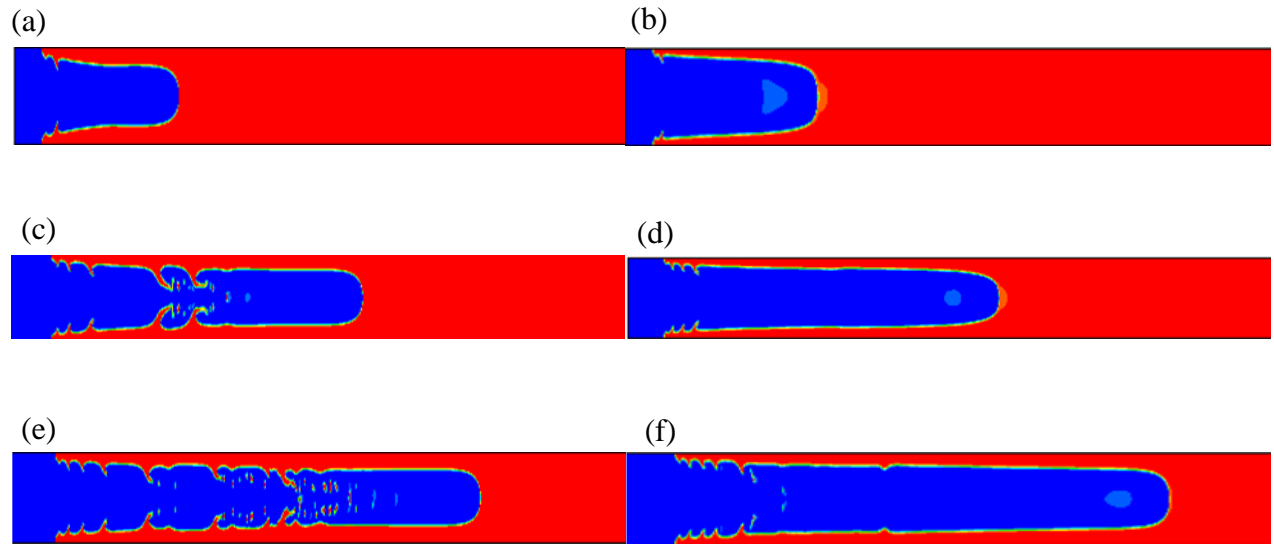


Figure 5.1: Displacement flow in a channel. Contours of index function. Case 1: At = 0.5 (left), Case 2: At = 0.85 (right). $\lambda = 20$ for both cases.

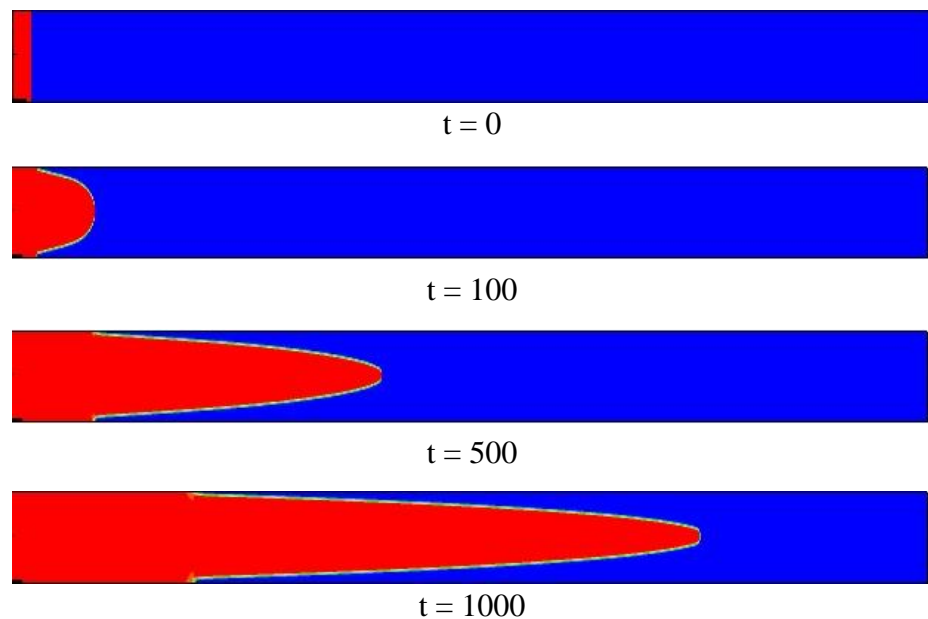


Figure 5.2: Displacement flow in a channel. At = 0, $\lambda = 0.9$. Contours of index function.

5.2.2 Results for flow in multi-branched channels

We next examine droplet formation in a T-junction in *Figures 5.3-5.5* using the S-C method. The effects of gravity are neglected in all cases in this section. The case in *Figure 5.3* corresponds to two fluids of equal density and viscosity. The inlet velocity of the dispersed phase is 0.015 l.u./s and the inlet velocity of the continuous phase is 0.20 l.u./s. This corresponds to a flow rate ratio of 1/13.3. The predicted regime is a discrete droplet flow [29]. As the dispersed phase (red fluid) enters the main branch, the continuous phase fluid (blue) imparts a substantial shear to the dispersed stream. Nonetheless, dispersed fluid must continue to enter the main branch. The relatively low flow rate of the dispersed phase gives it little time to fill the main branch before it necks and ultimately shears off by the continuous phase.

In *Figure 5.4*, the effect of channel geometry is explored. In *Figure 5.4a*, the ratio of the dispersed phase channel height to the main branch width is unity, while the ratio is $\frac{1}{2}$ in *Figure 5.4b*. The material properties are the same in both cases. The density and viscosity ratio of the dispersed to continuous phase are both 5, and the flow rate ratio of the dispersed to the continuous phase is 8. In *Figure 5.4a*, we observe the formation of slugs that occupy the entire main branch channel width. In this case, break-up of the dispersed phase stream (slug formation) is governed by pressure build-up upstream of a forming slug and not as a result of the shear [44]. At this flow rate ratio, the continuous stream does not have sufficient time to exert a stress capable of breaking the dispersed stream. In the case of *Figure 5.4b* however, the shear imparted by the continuous stream on the dispersed stream, combined with the larger main-branch width are sufficient to keep the dispersed fluid away from the right-most wall. The shear stress however is not capable of breaking up the dispersed phase stream. The observed flow regime is a jet or stratified flow. In *Figure 5.5*, the effect of viscosity ratio is studied. Here, *Figure 5.5a* is the same case presented in *Figure 5.4a* and *Figure 5.5b* is the same case except the viscosity

ratio has been increased to 10. In *Figure 5.5b*, it is observed that liquid slugs do eventually form but there now exists a significant dispersed phase jet extending into the main-branch. Because the downstream regime is slug flow, we suspect that pressure is ultimately the dominant stress responsible for break-up for this case.

The remaining calculations were performed using the H-C method (without the PPE). A related study was performed by Yu et al. [79]. In *Figure 5.6a* and *5.6b*, we examine displacement flow in a cross-junction and multi-branch distributor header respectively. Light fluid enters from the left and displaces the heavier fluid already present in the domain. The Atwood number is 0.3 and the viscosity ratio is 0.9 for both cases. Viscous fingering is observed in both cases. The flow field in both cases may be thought of as geometrically perturbed version of the flows in *Figures 5.1* and *5.2*. In the absence of a junction, each finger would be symmetric about a line of action parallel to the mean flow direction in each branch of the geometry. However, different sides of the displacing fluid encounter the junction at different times (the leading edge arrives first and begins translating down the side branch walls before the trailing edge of the displacing fluid, which encounters the junction later). This leads to non-symmetric fingers in the outlet branches.

In *Figure 5.7*, we examine an array of droplets in a T-junction which has applications to phase separation. Flow is from left to right. The density and viscosity ratio are both 2 and the inlet Reynolds number is 9. We observe deformation and rotation of the droplets which are advected by the continuous phase. The droplets eventually coalesce and simultaneously entrain the carrier fluid material. The droplet streams continue into the side branches and ultimately exit the domain. This flow is remarkably complex despite the modest Re.

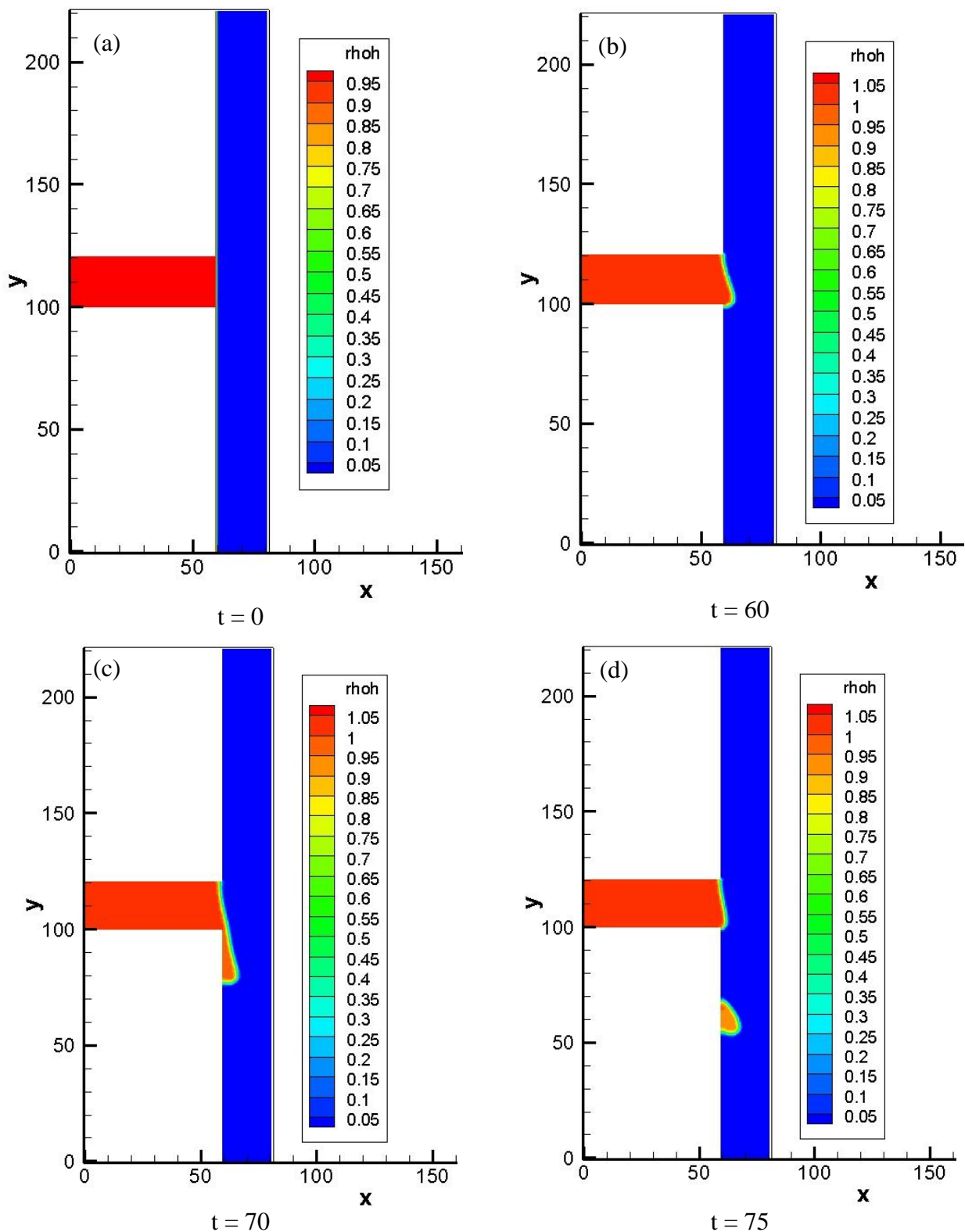


Figure 5.3: Droplet formation in a T-junction, density ratio = 1, viscosity ratio = 1, channel width ratio = 1.

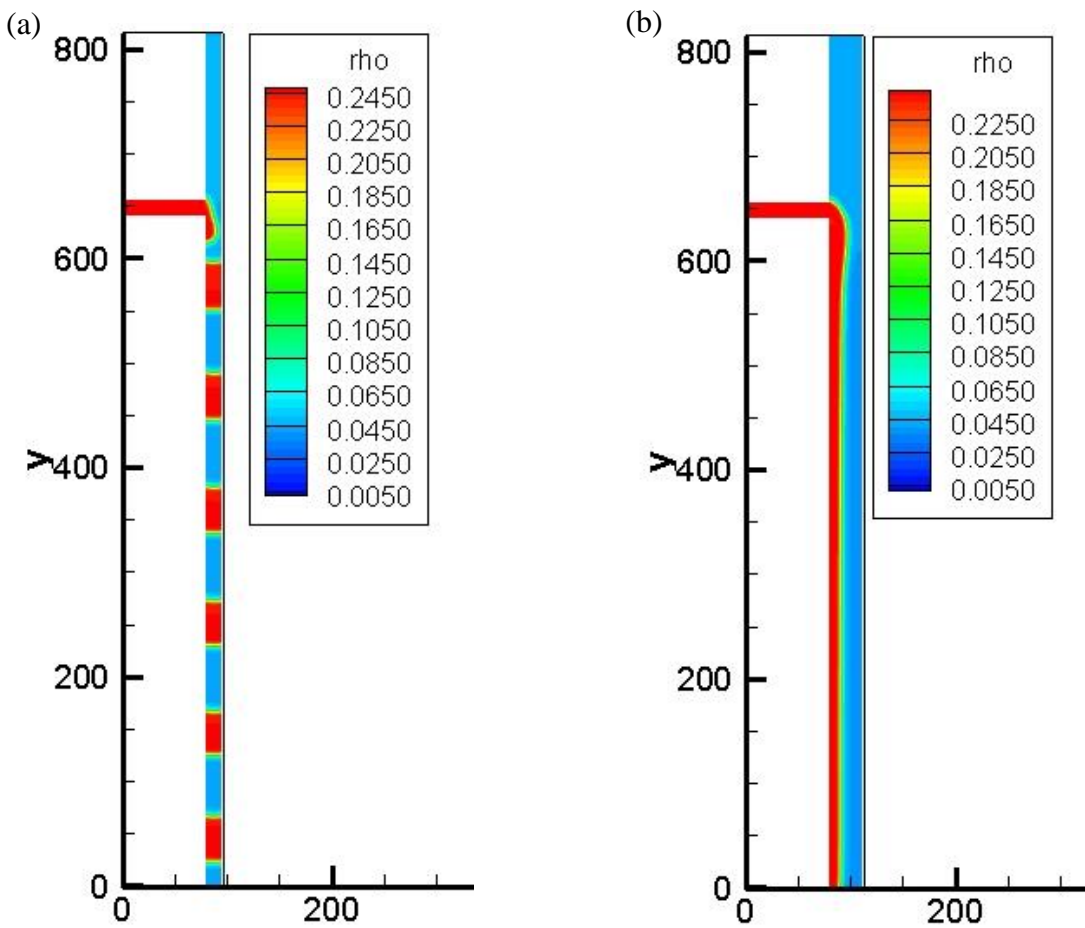


Figure 5.4: Liquid-vapor jetting and slug flow in a T-junction, geometric effect³⁸, density ratio = 5, viscosity ratio = 5, $Q = 8$, a) channel width ratio = 1, b) channel width ratio = $\frac{1}{2}$.

³⁸ Results obtained jointly with Purushotam Kumar.

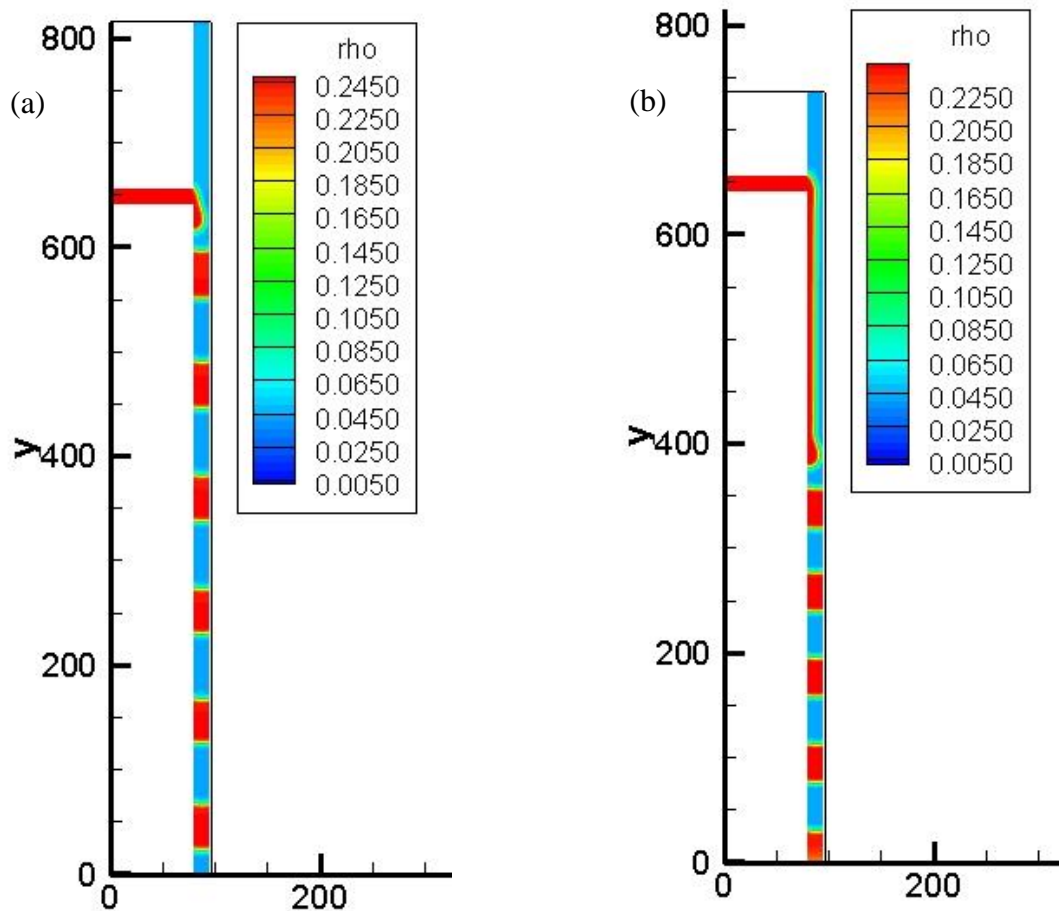


Figure 5.5: Liquid-vapor jetting and slug flow in a T-junction, effect of viscosity ratio,³⁹ density ratio = 5, flow rate ratio = 8 and channel width ratio = 1,
a) viscosity ratio = 5, b) viscosity ratio = 10.

³⁹ Results obtained jointly with Purushotam Kumar.

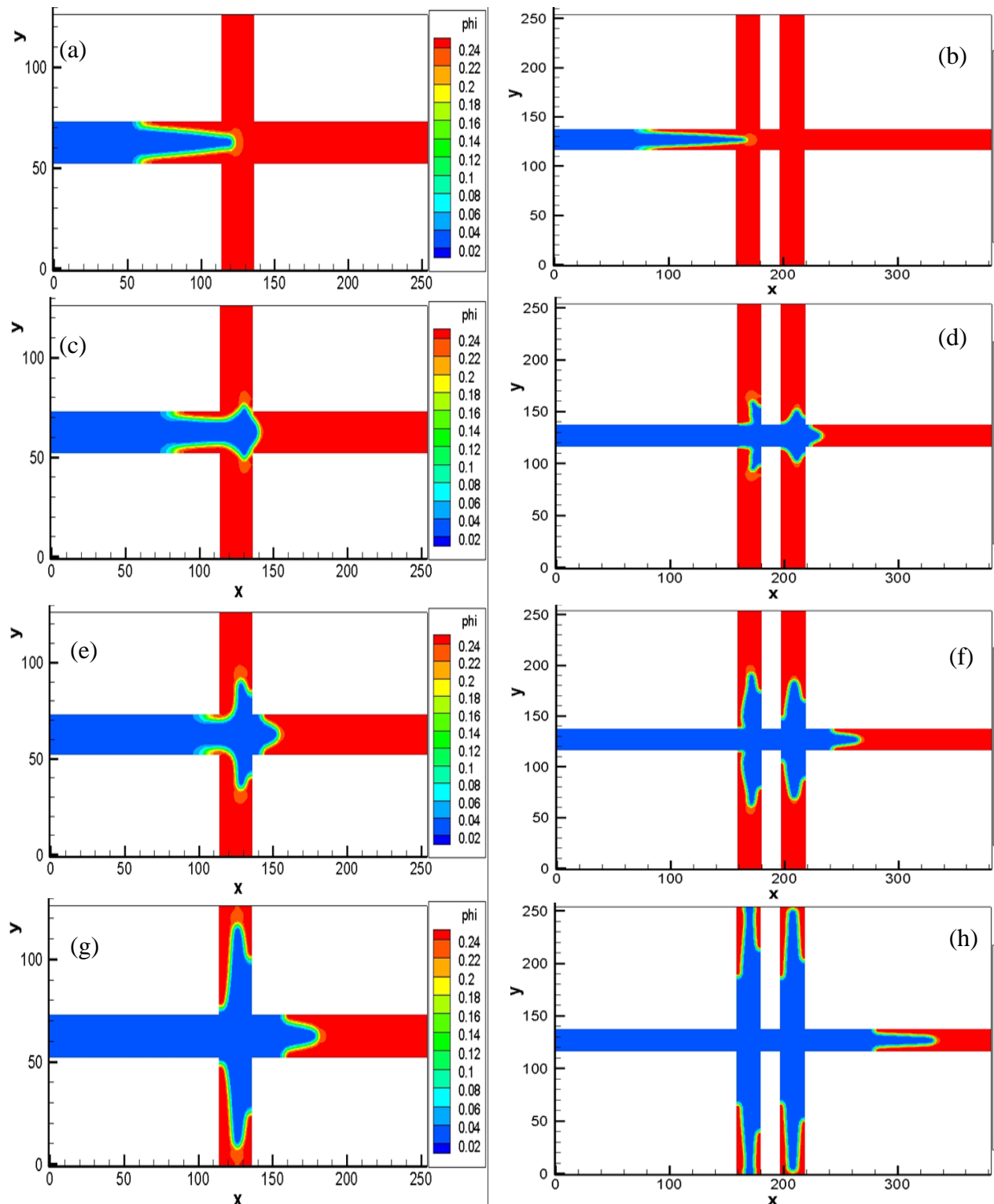


Figure 5.6: Displacement flow in complex geometries. Contours of index function.
Case 1: Flow in a cross-junction (left), Case 2: Flow in a distributor header (right). At = 0.3, and viscosity ratio = 0.9 for both cases.

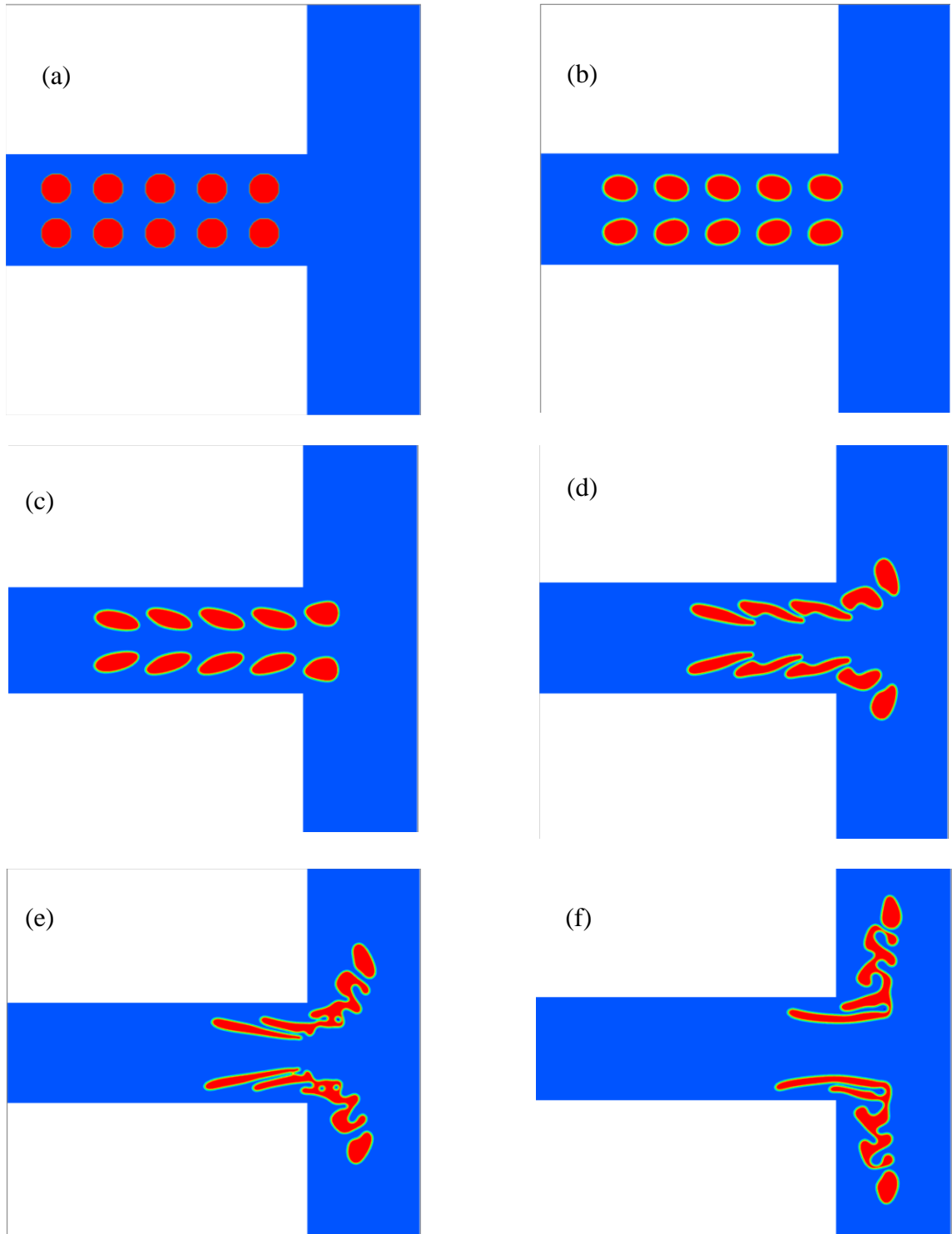


Figure 5.7: Array of droplets flowing in a T-junction⁴⁰, $\rho_h/\rho_l = 2$, $\lambda = 2$, $Re = 9$.

⁴⁰ Results presented at APS DFD 2012.

6. DEFORMATION OF A LIQUID DROPLET IN A SQUARE DUCT

6.1 Problem Description

The flow of liquid droplets in confined geometries is a problem of fundamental importance. Confined droplet flows are ubiquitous in ACRC applications. The study of droplet deformation began with the work of Taylor [23] who derived a deformation parameter assuming that the deformed droplet shape deviated only slightly from a spherical shape. Taylor showed the droplet deformation scaled linearly with the capillary number [23]. Hestrini and Haber [22] used the method of reflections to calculate the shape of a deformed droplet for the case of Stokes' flow in a pipe. Shapira and Haber [39] performed the same analysis for flow between parallel plates and later extended Taylor's work [23], obtaining an expression for the deformation parameter for a deformed droplet taking into account the presence of walls [40]. The case of a neutrally-buoyant axially translating droplet subject to an external flow is of particular interest. Goldsmith and Mason [27] performed separate low-Reynolds number pipe flow experiments where the carrier fluid contained rigid solid particles in one case, and deformable liquid droplets in the second. Contrary to the predictions of Jeffrey [20] that neutrally-buoyant particles would migrate to a region in the flow where the energy dissipation was minimum, Goldsmith and Mason observed that the droplets but not the particles migrated toward the pipe axis where shear was minimum [27]. Ho and Leal [13] examined creeping droplet motion in a pipe and also observed droplet migration toward the center axis independent of the initial position. This observation is consistent with the work of Kataoka and Inamuro [77] who observed that if the Weber number is above a critical value, the equilibrium droplet position will be axial independent of the initial position or of the Reynolds number. Nourbakhsh et al. [10] performed a 3D simulation of droplets in Poiseuille flow at finite Reynolds number and find the droplet

concentration along the channel center-line increases with increasing capillary number for capillary numbers in the range 0.05-0.8. A computational study by Mortazavi and Tryggvason [59] found that droplet migration may be toward or away from the axis depending on the viscosity ratio. Droplets of low viscosity compared with the carrier fluid tend to migrate toward the axis while highly viscous droplets tend to migrate toward walls. Migration toward the axis is also observed for high capillary numbers while migration away from the axis is observed for lower capillary numbers [59]. The extreme cases of low viscosity ratio and high capillary or high viscosity ratio and low capillary represent relative extremes with respect to droplet deformation. The former case is characteristic of high shear by the carrier fluid on the droplet which leads to deformation. A high capillary number indicates that the interfacial tension, which acts to maintain an equilibrium spherical droplet shape, is small in comparison with the shear stresses exerted on the surface of the droplet. In this regime, qualitative droplet deformation is high. In the latter case where the viscosity of the carrier fluid is small in comparison with the viscosity of the droplet, shear stresses exerted on the droplet surface are relatively small. At low capillary numbers, interfacial tension resists large deformation in the droplet interface.

In this chapter, we examine axial droplet deformation in a three-dimensional square-duct at finite Reynolds number. Special attention is given to both steady and transient deformation. This problem was chosen to study the fundamental issues relevant to transient droplet deformation. In addition, several facets of this problem have received less attention in literature. Much of the literature on confined droplet dynamics is concerned with droplet deformation in the Stokes' flow limit. A thorough review of droplet dynamics in the low-Reynolds number limit is given by Stone [25]. However, the role of inertia in droplet deformation may also be significant. In addition, the study of droplet deformation at finite-Reynolds number has received comparably

less attention. Singh and Sarkar [52] examine droplet deformation in a shear-flow between parallel plates for Reynolds numbers in the range 0.1-10. For low capillary numbers, droplet deformation appears to have little dependence on Reynolds number. However, at higher capillary numbers, a stronger dependence of deformation on Reynolds number is observed. Lan and Khismatullin [26] simulated droplet deformation in a micro-channel using the volume of fluid method for Reynolds numbers in the range 10-100. Equilibrium droplet deformation was observed to increase with increasing Reynolds number, although it's not clear whether this was a result of simultaneous increase in capillary number. Kataoka and Inamuro [77] explored Reynolds numbers up to 500, but droplet deformation was not considered.

While many authors have examined droplets subject to either Poissuile or linear-shear flow between parallel plates see [39, 40, 66, 46, 45, 7, 58, 18, 59, 33, 10, 52], most of the studies examining fully-confined droplet flows are restricted to circular geometries see [27, 13, 67]. Wang and Dimitrakopoulos [78] used a spectral boundary element method to simulate droplet flow in a square duct. However, their study considered flow at low-Reynolds number. Couvier et al. [21] examined droplet equilibrium shape for low-Reynolds number flow in rectangular ducts of varying aspect ratio cross-sections.

Finally, transient droplet deformation has been less well studied compared with steady-state deformation. Sibillo et al. [66] examines transient droplet elongation in a confined shear flow. Khan and Wang [33] performed simulations of transient droplet deformation in a 3D shear flow and calculated droplet elongation, spreading, and total deformation. Each of these scalars was found to increase monotonically as the capillary number was increased. Transient droplet deformation is also considered by [78, 12, 7, 58]. However, in each of these studies, the emphasis is placed on characteristics of droplet deformation in steady-state. The steady-state

droplet shape, elongation, spreading, and total deformation are strongly dependent on the Capillary number as will be shown in this section. The goal of this study is to elucidate aspects of both steady and transient droplet behavior which have more complicated capillary number dependence. We also examine the effect of Reynolds number and droplet to carrier fluid viscosity ratio. We show that inertial effects become less important as the Reynolds number is decreased, suggesting a convergence to the Stokes' limit. The viscosity ratio appears to have modest effects when it is close to unity. Further increase in the viscosity ratio however results in significant variation in the droplet's transient deformation history.

6.2 Results

6.2.1 Problem Statement

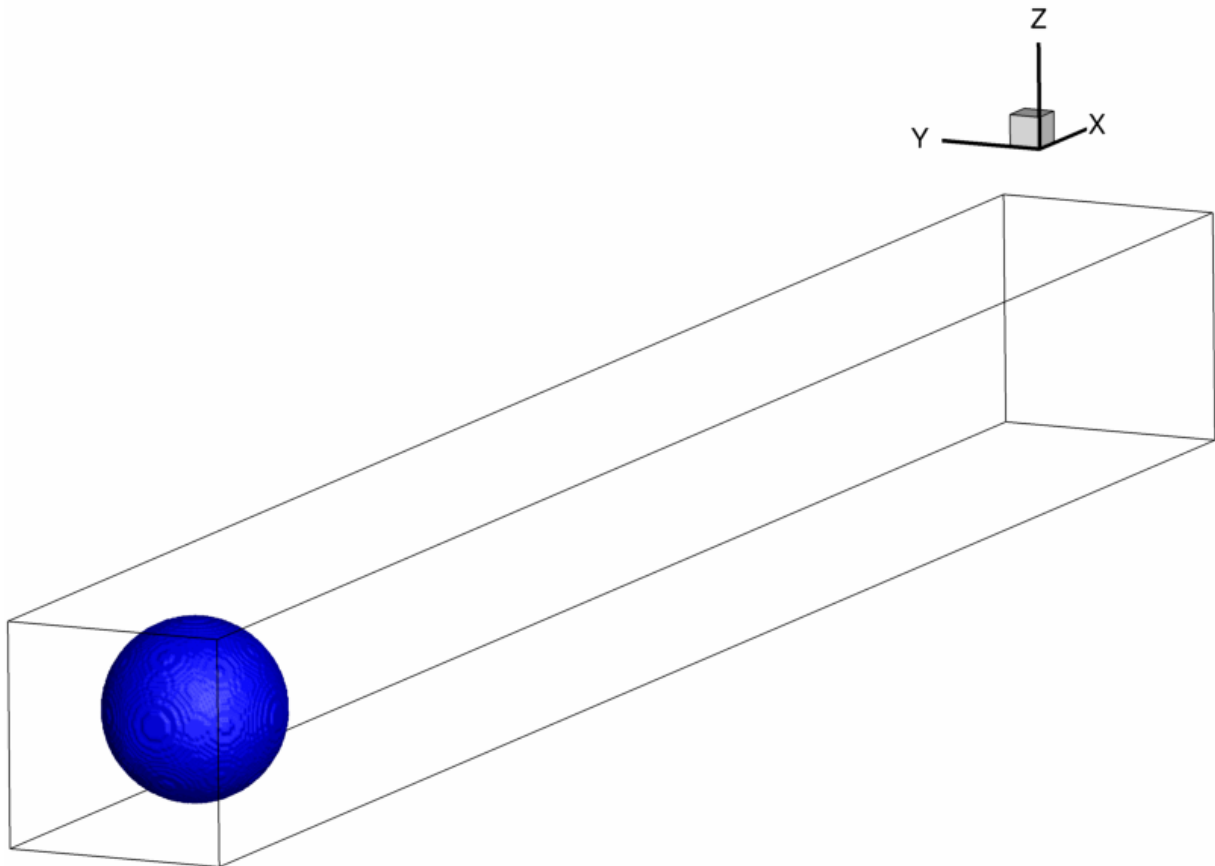


Figure 6.1: Simulation domain and droplet initial condition.

We simulate the case of an axially translating droplet in a square duct using the He and Chen method. The simulation domain is shown in *Figure 6.1*. In all cases, the droplet is neutrally buoyant (i.e. the droplet to carrier fluid density ratio is unity), so that the effects of gravity are neglected. No-slip, no-penetration conditions are prescribed at each wall using the Ghost-fluid method. The initial position (center of mass) of the droplet is one droplet diameter from the duct inlet. The initial condition everywhere is a fully developed unidirectional velocity profile.

Assuming a steady laminar flow, the single-phase solution satisfies the Poisson equation, given in Cartesian form as:

$$\nabla^2 u = \frac{\partial^2 u}{\partial y^2} + \frac{\partial^2 u}{\partial z^2} = \frac{1}{\mu} \frac{dp}{dx} \quad (6.1)$$

For an infinite-length duct of square cross-section with sides of length $2r$, the analytical solution is given by [19]:

$$u(y, z) = \frac{16r^2}{\mu\pi^3} \left(-\frac{dp}{dx} \right) \sum_{i=odd}^{\infty} (-1)^{(i-1)/2} \left[1 - \frac{\cosh\left(\frac{i\pi z}{2r}\right)}{\cosh\left(\frac{i\pi}{2}\right)} \right] \cdot \frac{\cos\left(\frac{i\pi y}{2r}\right)}{i^3} \quad (6.2)$$

And the cross-section averaged velocity:

$$u_b = \frac{r^2}{3\mu} \left(-\frac{dp}{dx} \right) \left[1 - \frac{192}{\pi^5} \sum_{i=odd}^{\infty} \frac{\tanh\left(\frac{i\pi}{2}\right)}{i^5} \right] \quad (6.3)$$

It is the velocity profile defined in (6.2) that is prescribed as the initial velocity everywhere in the simulation domain. The inlet is also prescribed fully developed conditions while the outlet velocity is constrained to have zero-gradient. To maintain a fully developed mean flow, an axial pressure gradient independent of position and consistent with (6.2) is prescribed so that the LBM calculated pressure will be interpreted as the pressure perturbation on the local mean pressure as

a result of the droplet's presence⁴¹. The mean velocity given in (6.3) allows us to define a Reynolds number:

$$Re = u_b H / \nu_1 \quad (6.4)$$

Where H is the duct height and ν_1 is the kinematic viscosity of the carrier fluid.⁴² In many previous studies which examined droplet deformation in the Stokes' limit, the Reynolds number was not considered a relevant dimensionless parameter. In the Stokes' limit the relative role of inertia compared with viscosity is small so that any effect of deformation on an inertial parameter (Re) is assumed to be negligible. In fact, our results will suggest that deformation at low Reynolds number likely does not carry a strong Reynolds number dependence, but rather the dependence at high Reynolds numbers cannot be ignored.

Another key parameter we study is the Capillary number:

$$Ca = \mu_1 u_b / \sigma \quad (6.5)$$

Where σ is the interfacial tension and calculated using (2.43). The capillary number represents the relative importance of viscous shear stresses of the carrier fluid on the droplet, and the

⁴¹ The pressure perturbation will be due to interfacial tension and non-unity viscosity ratio; no pressure perturbation is expected when the previous two conditions are not met since the result would be a single phase fully developed flow.

⁴² Note that each variable in (6.4) can be written in terms of lattice units (l.u.) and other dimensions. For example, the finest mesh we use is described by a height of 96 l.u. and the mean velocity in most simulations is 0.052083 l.u./s. Variables expressed in l.u. have no physical meaning and thus cannot be a basis of comparison. In defining non-dimensional parameters, we have made the usual assumption that is not the constituent variables, the magnitude of the non-dimensional group itself that matters. This case is no exception in that $Re = 100$ can be formed by a triply-infinite number of combinations of mean velocity, duct height, and carrier kinematic viscosity. Whatever the combination, we expect $Re = 100$ to have the same meaning as in any experiment or other computational setting according to the notion of dynamic similarity.

interfacial tension between the droplet and carrier fluids. In the limit of zero interfacial tension (infinite capillary number) there exists no elastic resistance to deformation. The droplet's own viscosity will resist deformation induced by the carrier fluid (and the droplet's own advection in a non-uniform velocity field), but without surface tension, the droplet does not have the preferred spherical shape. It will continuously deform as laminar sheets, where each point in the wall-normal direction at any axial location will define a different sheet. In other words the droplet deforms as each piece of droplet material is simply advected with the local fluid velocity, which remains steady and independent of stream-wise position. At the other extreme denoted by infinite interfacial viscosity or zero capillary number, the droplet remains perfectly spherical. The carrier fluid then flows around and pushes the droplet, as if it were a rigid body of finite Stokes number⁴³, but the droplet experiences no deformation. While there is no definite agreement in literature, capillary numbers greater than 1 are usually considered high, while capillary numbers below 0.01 say are considered low. In this study, we examine capillary numbers in the moderate range $Ca \in [0.1, 0.15, 0.2, 0.25]$.

The final non-dimensional parameter we consider is the droplet to carrier fluid viscosity ratio which is denoted by λ . We expect modest deformation dependence on the viscosity ratio when λ is close to unity, since, other things equal, a unity viscosity ratio would indicate a single-phase flow. In this study, we examine large viscosity ratios. In an infinite viscosity ratio limit, we expect the droplet to behave similarly to the zero capillary number case, that is we expect no droplet deformation.

A summary of the cases run in the droplet deformation study are presented in *Table 6.1*. In the next section, we first present a grid study using three meshes. GPU memory capacity

⁴³ The Stokes number is a non-dimensional representation of a mass's (typically a particle) response time relative to a characteristic fluid response time. Zero Stokes number means the mass is a fluid tracer while an infinite Stokes number indicates a mass that is unaffected by the surrounding fluid.

limited our finest calculation to a 10:1 square duct of dimensions 96x96x960. The droplet confinement, (i.e. the ratio of the initial droplet diameter to duct height) is 0.8125. This corresponds to droplets of 26 l.u., 52 l.u., and 78 l.u. for the 32x32x320, 64x64x640, and 96x96x960 grids respectively. However we will show that sufficient grid convergence was achieved. We then perform a series of calculations to examine parametric dependence of droplet deformation on Capillary number, Reynolds number, and viscosity ratio.

| Case | Re | Ca | λ | Grid |
|-----------------|-----------|-----------|-----------------------------|-------------|
| Grid Study | | | | |
| 1a | 100 | 0.25 | 1 | 32x32x960 |
| 1b | 100 | 0.25 | 1 | 64x64x960 |
| 1c | 100 | 0.25 | 1 | 96x96x960 |
| Ca Study | | | | |
| 1c/2a | 100 | 0.25 | 1 | 96x96x960 |
| 2b | 100 | 0.10 | 1 | 96x96x960 |
| 2c | 100 | 0.15 | 1 | 96x96x960 |
| 2d | 100 | 0.2 | 1 | 96x96x960 |
| Re Study | | | | |
| 1c/3a | 100 | 0.25 | 1 | 96x96x960 |
| 3b | 50 | 0.25 | 1 | 96x96x960 |
| 3c | 25 | 0.25 | 1 | 96x96x960 |
| 3d | 10 | 0.25 | 1 | 96x96x960 |
| λ Study | | | | |
| 1c/4a | 100 | 0.25 | 0.5 | 96x96x960 |
| 4b | 100 | 0.25 | 1 | 96x96x960 |
| 4c | 100 | 0.25 | 2 | 96x96x960 |
| 4d | 100 | 0.25 | 4 | 96x96x960 |
| 4e | 100 | 0.25 | 8 | 96x96x960 |
| 4f | 100 | 0.25 | 16 | 96x96x960 |
| 4g | 100 | 0.25 | 32 | 96x96x960 |

Table 6.1: List of cases for droplet deformation in a square duct study.

6.2.2 Verification and Validation

We first validate our multiphase LBM algorithm by simulating low Reynolds number droplet flow in square duct as investigated by Wang et al. [78] using a boundary integral formulation. The actual Reynolds number prescribed in [78] was not explicitly mentioned. In our formulation, $\text{Re} = 2$ was chosen to balance computation time and accuracy. However, as shown in section 6.4, substantial decrease in Reynolds number would likely not have affected the validation results. The flow is prescribed fully developed conditions and the magnitude of droplet deformation D , defined as the maximum stream-wise to wall-normal droplet lengths, is plotted vs. time for three different Capillary numbers in *Figure 6.2*.

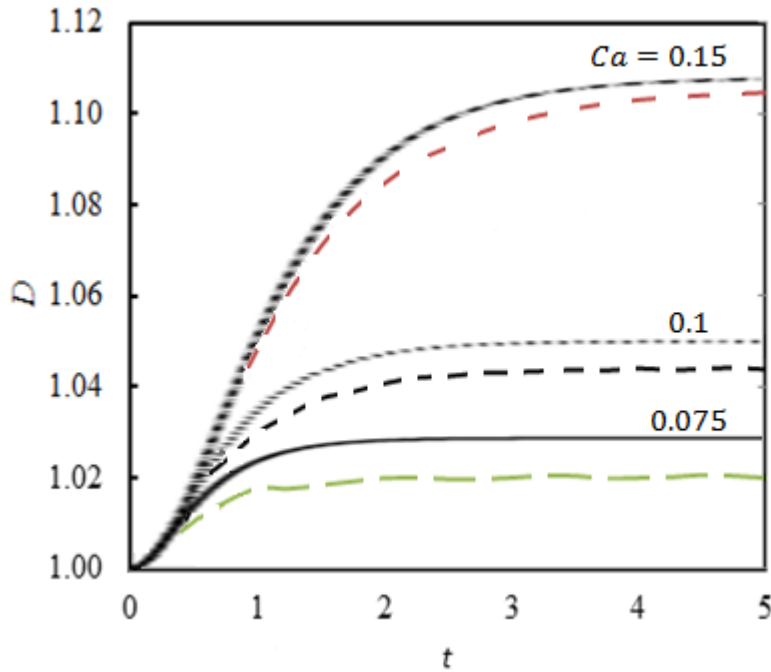


Figure 6.2: Algorithm validation with boundary element simulation of low Reynolds number droplet deformation in a square duct, $\lambda = 2.04$, confinement = 0.8, LBM results (dashes), results reproduced from [78] (solid and dotted lines).

The LBM predicted results are in good agreement with the results obtained by [78]. The steady-state LBM-predicted deformation parameters are slightly less than those predicted by [78] for each of the capillary numbers. The trends however match well between the two algorithms for each capillary number. We therefore conclude LBM is capable of simulating the problem of droplet deformation in a square-duct with good accuracy. Further, we expect LBM to be more accurate in the moderate Reynolds number cases discussed later. The boundary element method used in [78] and by other authors [46, 45, 12] has been used extensively to study confined droplet deformation. However, its use as a computational methodology is only valid in the low Reynolds number limit where the flow equations become linear, allowing a fundamental solution to be defined. Therefore, while the boundary element predictions are more accurate in the low Reynolds number case, we expect the LBM results to be more accurate in the moderate Reynolds cases, since the LBM algorithm makes no assumptions about the magnitude of the Reynolds number.

In the H-C method, two separate fluids are identified via an index function, which takes on a value of ϕ_1 in fluid 1 and ϕ_2 in fluid 2. In each of our simulations we take the definition of the interface to be the mean of ϕ_1 and ϕ_2 , or as defined in (6.6), $\beta = 0.5$:

$$\phi_{int} = \beta\phi_2 + (1 - \beta)\phi_1 \quad (6.6)$$

Where ϕ_{int} is the value of phi at the interface. $\beta = 0.5$ is consistent with the interfacial location chosen in the popular surface tension model derived in [29]. However, it is natural to wonder how sensitive the results are on the definition of the interface. That is, does the choice of interface location significantly influence droplet dimensions, or the deformation parameter for

instance? In *Figure 6.3*, we observe that the choice of interface location only has a small effect on the droplet deformation history.

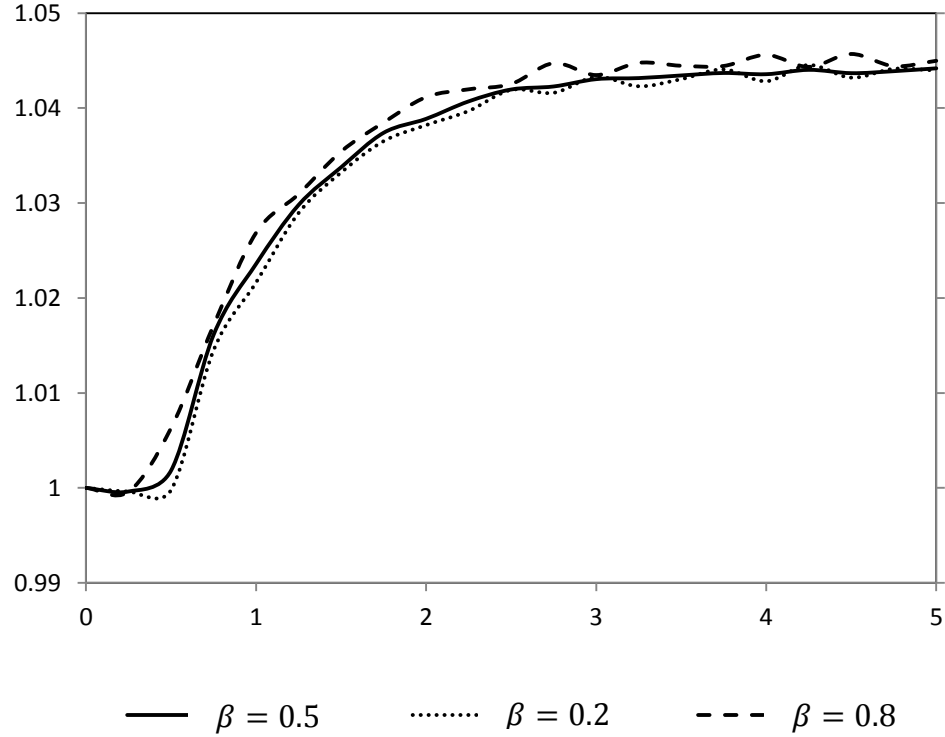


Figure 6.3: Effect of interface definition on deformation results,
 $\text{Ca} = 0.1$, Confinement = 0.8, $\text{Re} = 2$.

We believe this observation will remain true provided that the droplet is sufficiently resolved globally and locally. By global resolution, we mean that by changing the interface location in an ε -neighborhood around the droplet, the droplet deformation history and all other deformation characteristics are changed nominally at most. This is true provided the initial number of grid points used to resolve the droplet is not small. Typical 25 l.u. or more are preferred. By locally resolved, any local deformation on the droplet should not be the same order as the interfacial

thickness of ~ 3 l.u. Provided these conditions are met, the droplet will be considered sufficiently resolved.

We next perform a grid study to ensure the results we obtain are grid independent. In *Figure 6.4*, we illustrate droplet contours and define dimensions used to quantify droplet deformation. In all cases, droplet dimensions used to quantify deformation are taken in a horizontal slice through the droplet and co-planar with the duct center-plane oriented in the stream-wise direction. This corresponds to the plane of highest deformation. (The vertical center-plane in the stream-wise direction would yield the same results by symmetry of the problem.) The droplet shape begins as a sphere. Referring to *Figures 6.4c* and *d*, the initial droplet length and width are equal in magnitude to the droplet diameter and are denoted by L and W respectively. In *Figure 6.4d*, we define three characteristic dimensions for the deformed droplet, L_T , L_A , and W_T , which are respectively the deformed droplet's maximum stream-wise length, the droplet's length as measured axially from leading to trailing edges, and the maximum tip-to-tip droplet width in the wall-normal direction. Two length scales were required since the axial length may differ significantly with the maximum droplet length, however the maximum droplet width typically does not differ greatly from any other characteristic droplet width that could be defined. In *Figures 6.4e* and *f*, we show the finest grid overlaid with a highly deformed droplet contour. In examining *Figures 6.4f*, it is clear that the local region of high deformation is still resolved with many grid points so that the calculation for the highest deformation cases may be considered sufficiently resolved.

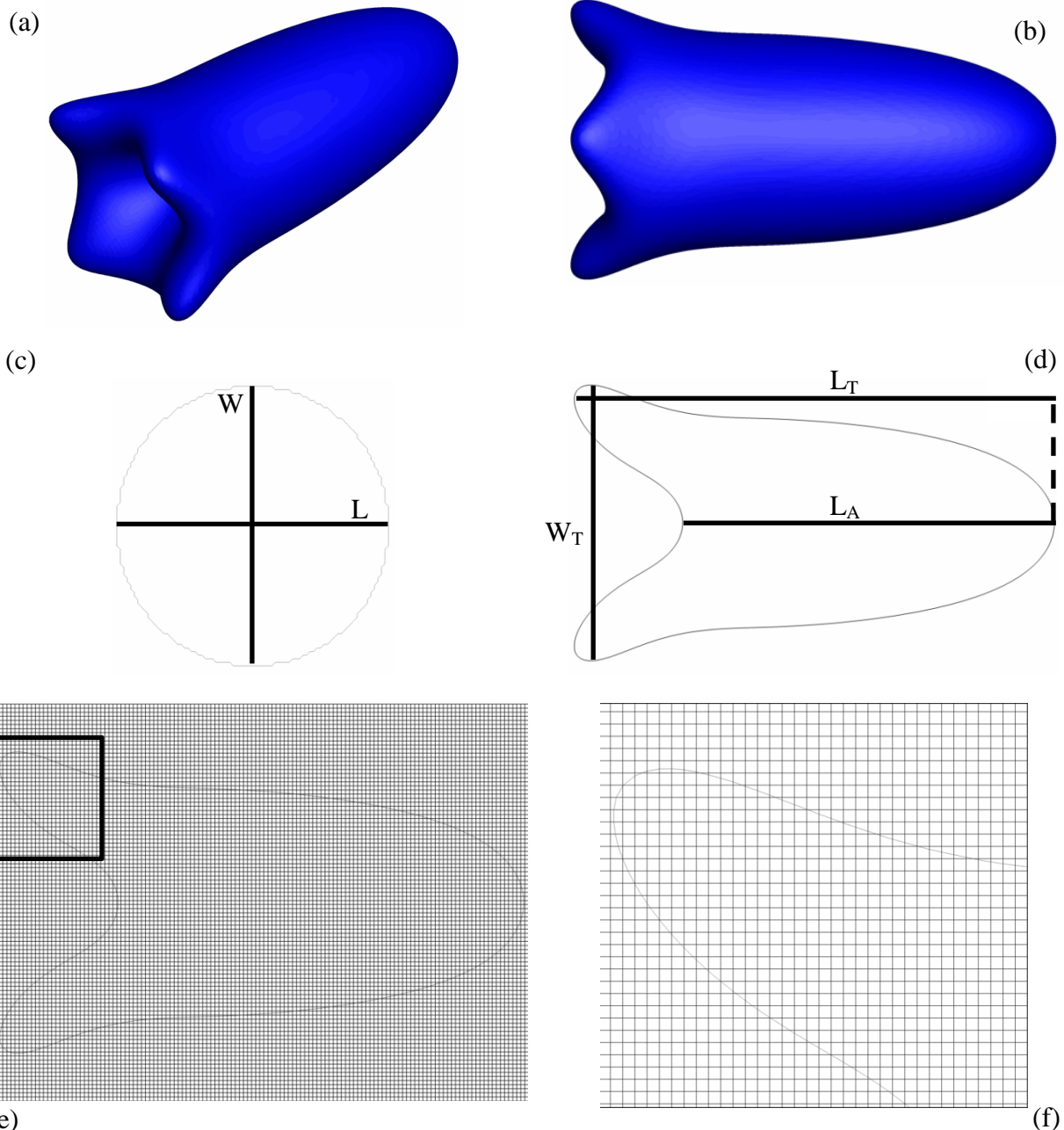


Figure 6.4: Droplet contours, geometric definitions, grid resolution (a) 3D droplet contour, isometric view, (b) side view, (c) 2D horizontal slice, initial droplet shape, (d) 2D horizontal slice, transient droplet shape, (e) 2D droplet contour overlaid with finest grid, (f) zoomed view of droplet contour overlaid with finest grid. $\text{Ca} = 0.25$, $\text{Re} = 100$, $\lambda = 1$.

With L_T , L_A , and W_T defined, we may introduce four non-dimensional groups used to characterize the droplet's deformation: the maximum elongation E_T , the axial elongation E_A , the spread factor S , and the deformation parameter D . Their respective definitions are given in (6.7)-(6.10):

$$E_T = (L_T - L)/L \quad (6.7)$$

$$E_A = (L_A - L)/L \quad (6.8)$$

$$S = (W_T - W)/W \quad (6.9)$$

$$D = L_T/W_T \quad (6.10)$$

Since (6.7)-(6.9) are strain-like parameters, a value of zero for these respective parameters is indicative of little or no-deformation while a deformation D of magnitude 1 indicates a spherical or approximately spherical droplet.⁴⁴ With these non-dimensional groups defined, we may examine the grid study presented in *Figure 6.5*, where E_T , E_A , and S are plotted vs. time for three grid cross-sectional grids.⁴⁵ The non-dimensional time-step in *Figure 6.5*, as in the subsequent results is defined according to (6.11):

$$t^* = \frac{750u_b\Delta t}{H} \quad (6.11)$$

⁴⁴ Deformation measurements are made in plane since this provides a reasonable basis for comparison in any physical experiment. However, it should be understood that out of plane deformation does exist. While the droplet deformation has a symmetry on account of the duct cross-sectional geometry, this should not be confused with axisymmetry. As can be observed *Figure 6.4a* and *b*, the droplet trailing edge has “corner” symmetry.

⁴⁵The dependence of droplet deformation history on grid was not investigated specifically since it is derivative from the previous non-dimensional groups. However, the deformation parameter has been explored ubiquitously in literature and remains as an important basis for describing droplet deformation and for comparing to other works.

Moderate variation in deformation histories are observed between the 32x32 and 64x64 grids, however little variation is observed between the 64x64 and 96x96 grids for E_T and E_A parameters. Small variation in the spreading history is observed between the 64x64 and 96x96 grids. Overall, it is clear the solution is converging as the grid is refined. The 96x96x960 grid was chosen as the basis for our subsequent calculations. This was in part limited by the memory resources or the GPU. However, the grid convergence is adequate so the droplet interface is sufficiently resolved. We therefore assert that the subsequent results are sufficiently grid-independent. The accuracy of the calculations will be sufficient for fundamental physics to be evinced from these simulations, where the precise magnitude of deformation could be investigated in the future with a more refined grid.

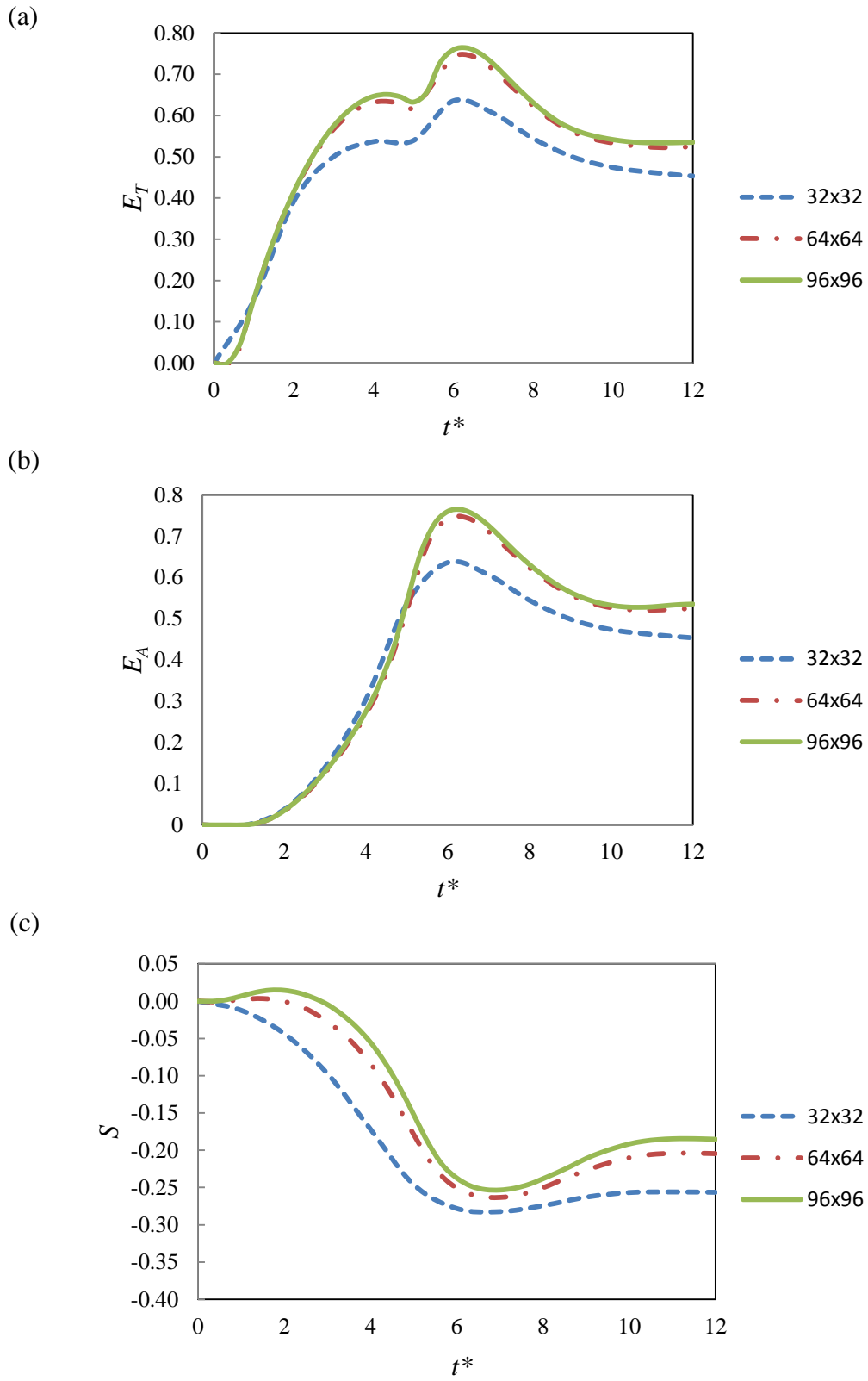


Figure 6.5: Grid study, legends correspond to duct cross-section. $\text{Ca} = 0.25$, $\text{Re} = 100$, $\lambda = 1$.

6.2.3 Effect of Capillary Number

We first examine the effect of capillary number on droplet deformation. Droplet contours for four capillary numbers at different characteristic times are shown in *Figure 6.6*. Characteristic deformation parameter histories are shown in *Figure 6.7* and *6.8* for different capillary numbers. We observe that total and axial droplet elongations increase with capillary number. The magnitude of spreading also increases with capillary number. Regarding the elongation history in *Figure 6.7a*, we may identify four distinct regimes which exist independent of capillary number. In regime (1), there exists an extended period of elongation as droplet

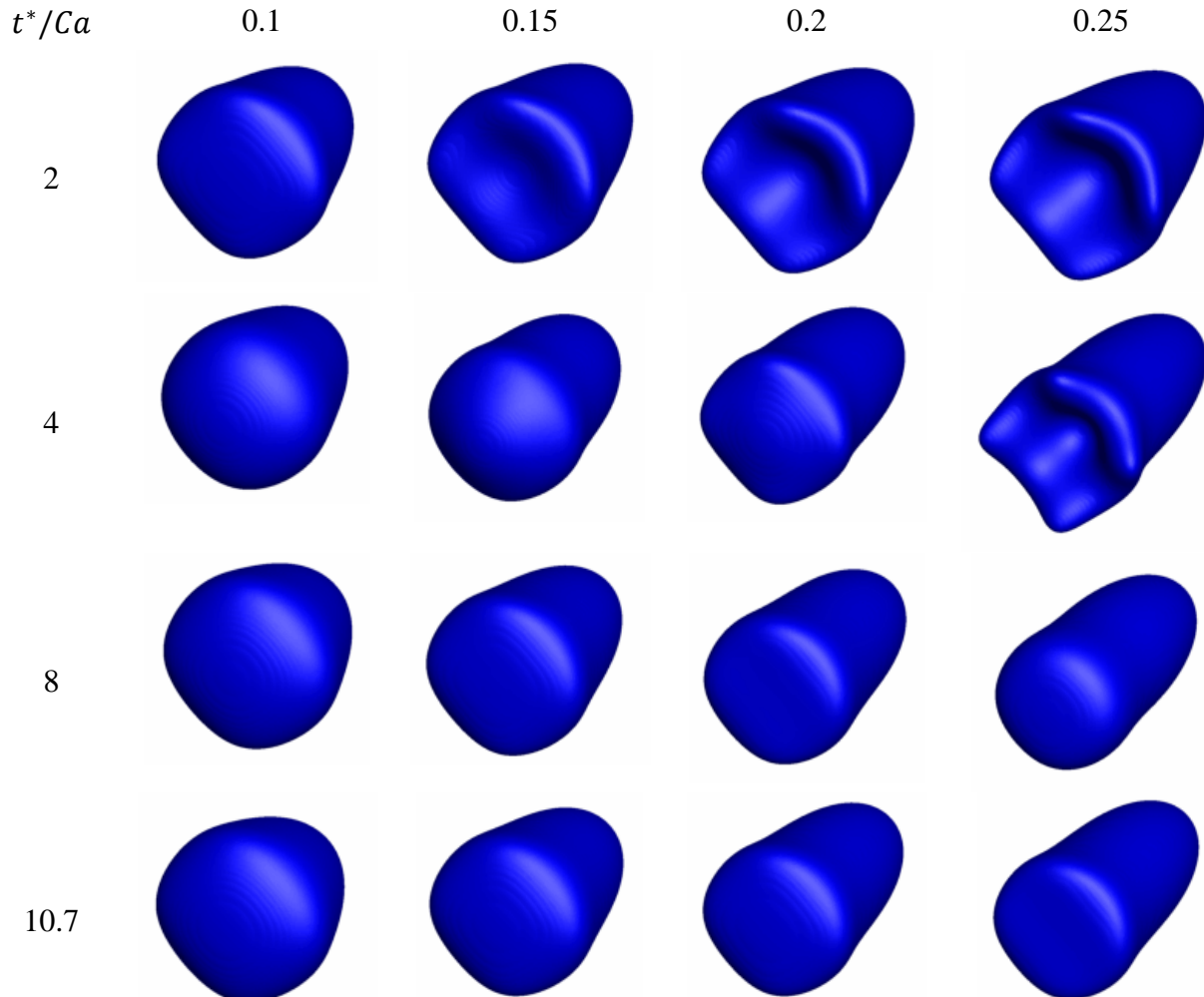


Figure 6.6: Droplet contour history for different capillary numbers, $Re = 100$, $\lambda = 1$.

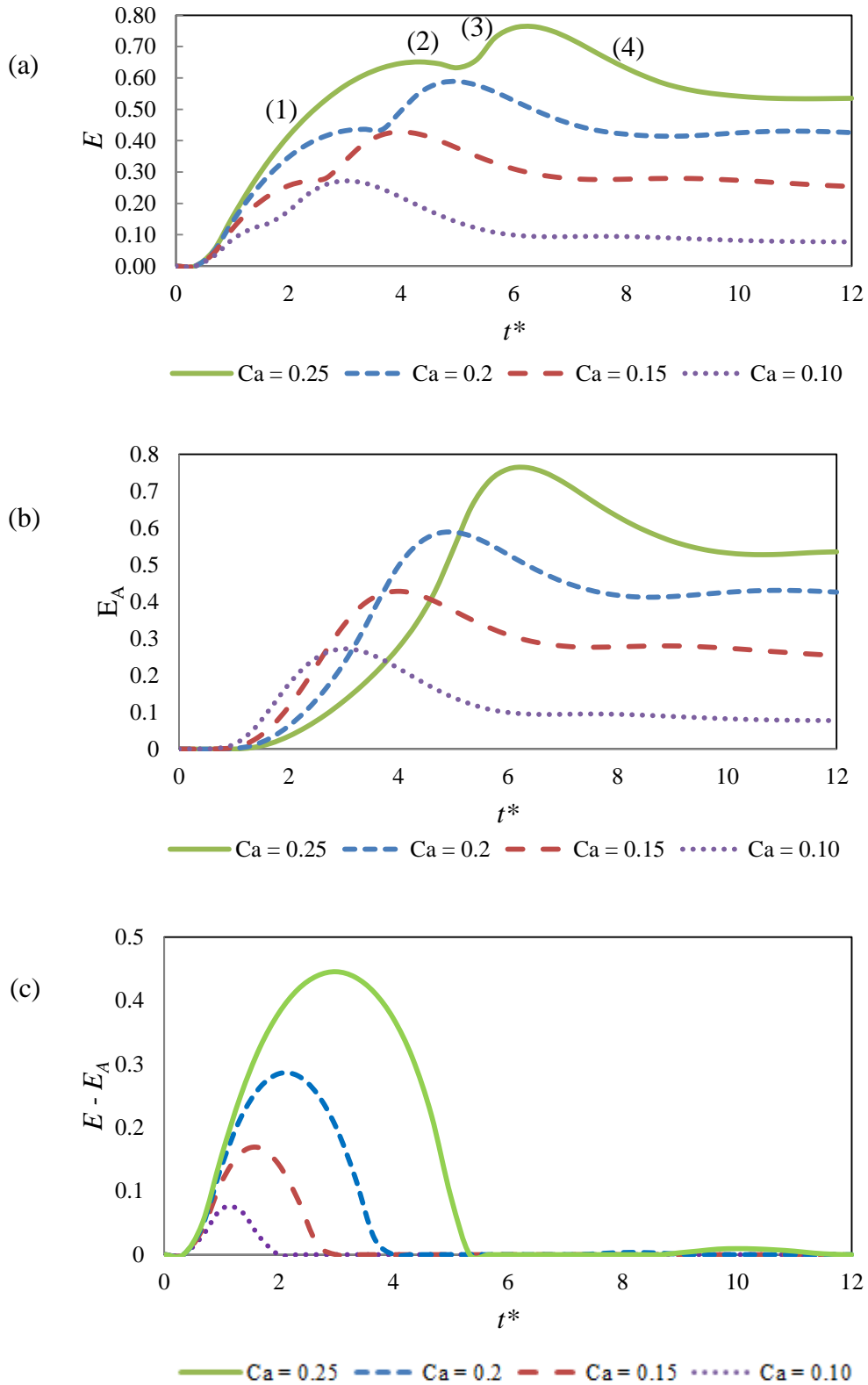


Figure 6.7: Capillary number study, elongation (a) maximum, (b) axial, (c) difference, $\text{Re} = 100$, $\lambda = 1$.

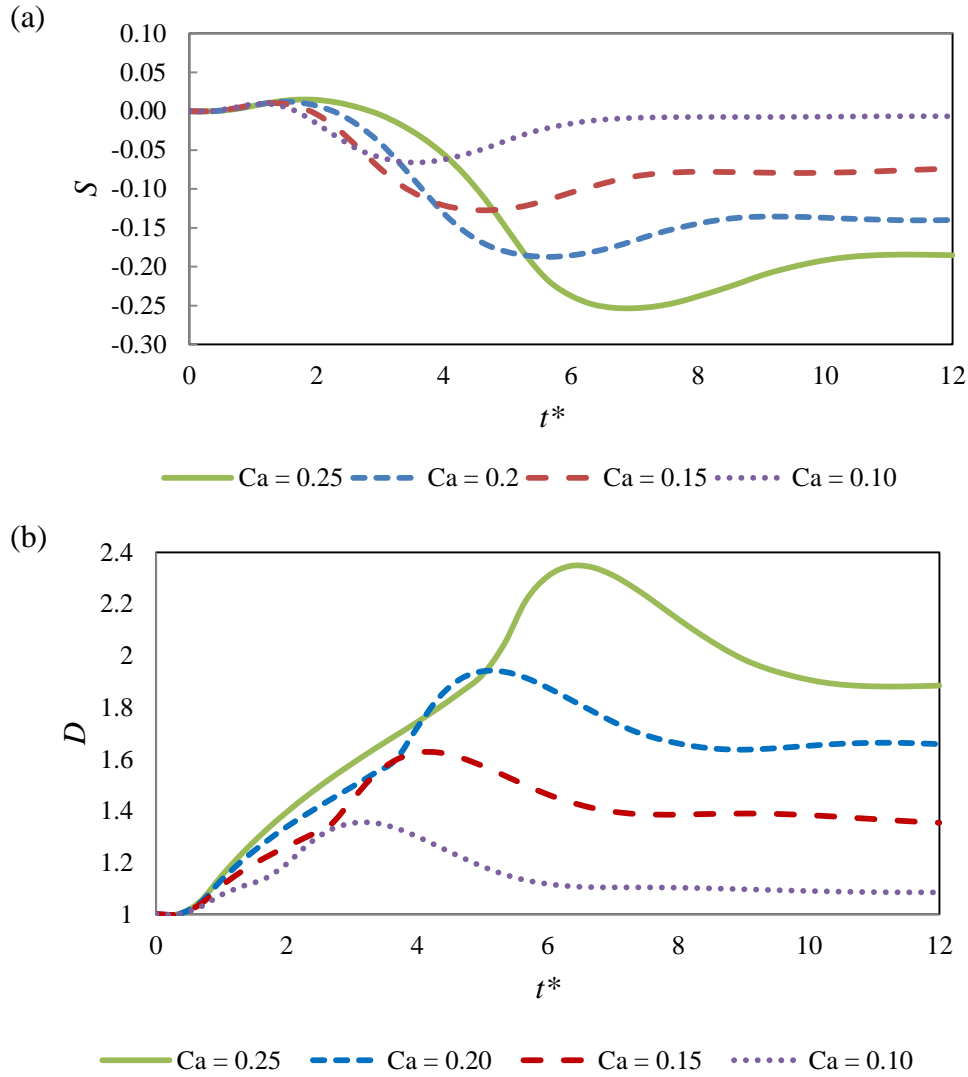


Figure 6.8: Capillary number study, (a) spreading, (b) deformation, $\text{Re} = 100$, $\lambda = 1$.

material away from the axis is held up by the no-slip condition at the wall. Droplet material near the duct axis is relatively un-constrained allowing the droplet leading edge to extend forward. The droplet's axial trailing edge moves slightly slower than the leading edge but the primary elongation is due to the difference in axial and near-wall stream-wise velocity. This can be observed in *Figure 6.9a*. The second regime is shown in *Figure 6.9b,c*. At the droplet axial trailing edge, a local region of high pressure and low stream-wise velocity develops. Whereas in

the first regime, viscous stresses may have been overcoming interfacial tension, it is perhaps in this regime where interfacial stresses begin to dominate as the interfacial curvature reaches a maximum. In examining *6.10b,c* showing wall-normal velocity contours, we observe a flux of droplet material towards the axis. The “ears” that had formed in regime (1) begin to dissipate as lateral mass is converted to axial mass. This observation is also evident in the steepness of the spreading history for $\text{Ca} = 0.25$, around $t^* = 5$ in *Figure 6.8a*. In regime (2), the total elongation of the droplet changes little. In regime (3), the mass flux from the wall towards the axis is converted from an lateral inward spread to a stream-wise elongation. This is represented in *Figure 6.9d*. This second burst of elongation is analogous to squeezing a putty-like substance where squeezing in one direction serves to elongate another direction. In the 3rd regime and beyond, the elongation is almost purely axial as is evident in *Figure 6.7c*. In the final regime, a period of relaxation occurs where droplet shape and therefore deformation parameters relax toward a steady state. There appear small oscillations during late times for the larger capillary number cases indicating the capillary number may be acting like a representative damping factor. The higher capillary number droplets may be thought of as under-damped.

Observing *Figure 6.7-6.8*, we observe apparent self-similarity in the droplet deformation histories, that is, the elongation history for one capillary number is a scaled version of an elongation history for a different capillary number. That is, it may be possible to relate the amplitude of elongation of one capillary number at one time, to the amplitude of elongation of another capillary number at an earlier time. This trend is most evident in *Figure 6.7c*, which shows the difference in total and axial elongation for different capillary numbers. At early times, the difference exists because the elongation curves are concave down while the axial elongation curves are concave up. This indicates that early deformation is not a result of the difference in

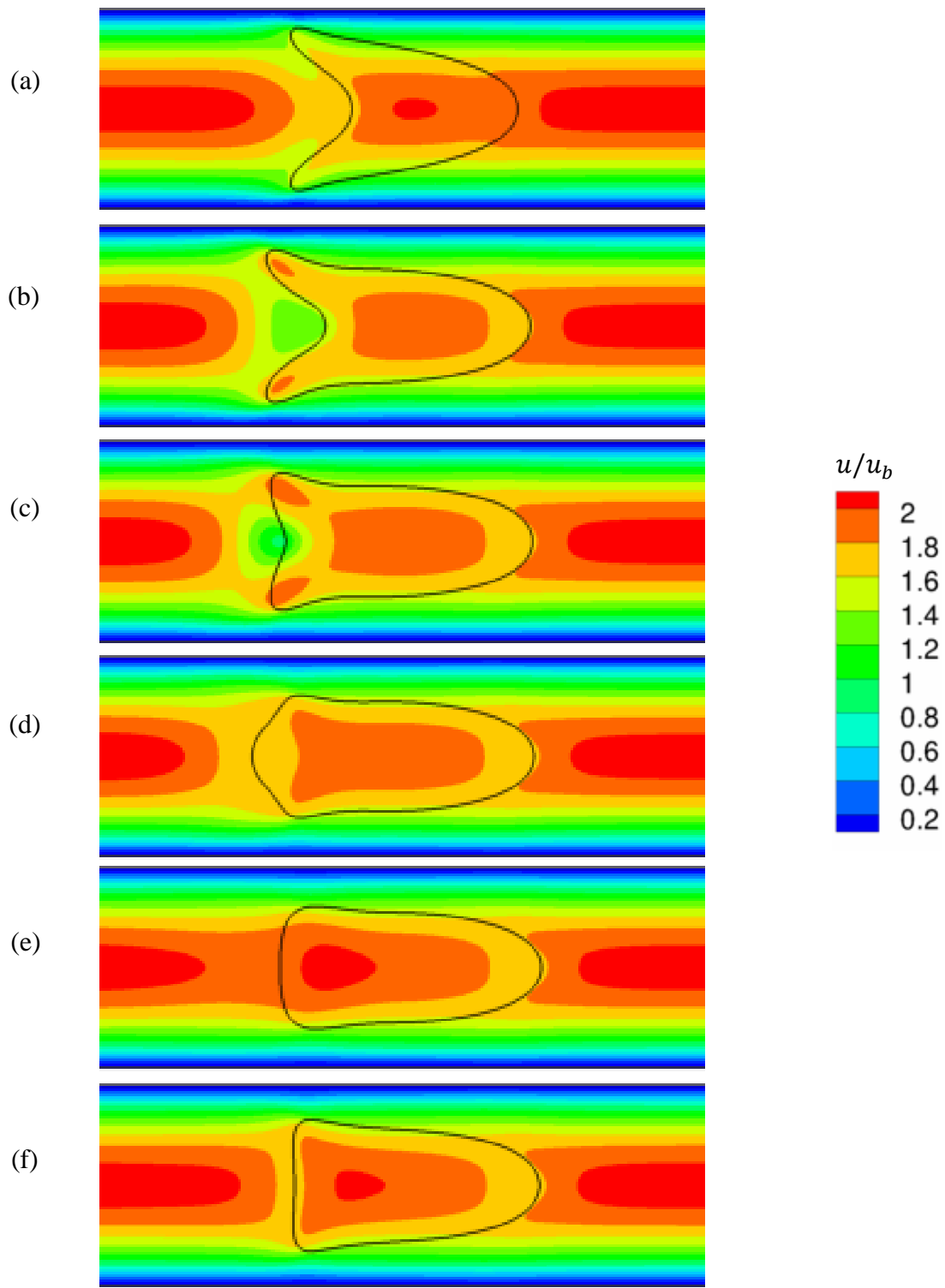


Figure 6.9: Duct center-plane stream-wise velocity contours overlaid with two-dimensional droplet shape, $\text{Ca} = 0.25$, $\lambda = 1$, $\text{Re} = 100$, (a) $t^* = 2$, (b) $t^* = 4$, (c) $t^* = 5$, (d) $t^* = 6$, (e) $t^* = 8$, (f) $t^* = 10.7$.

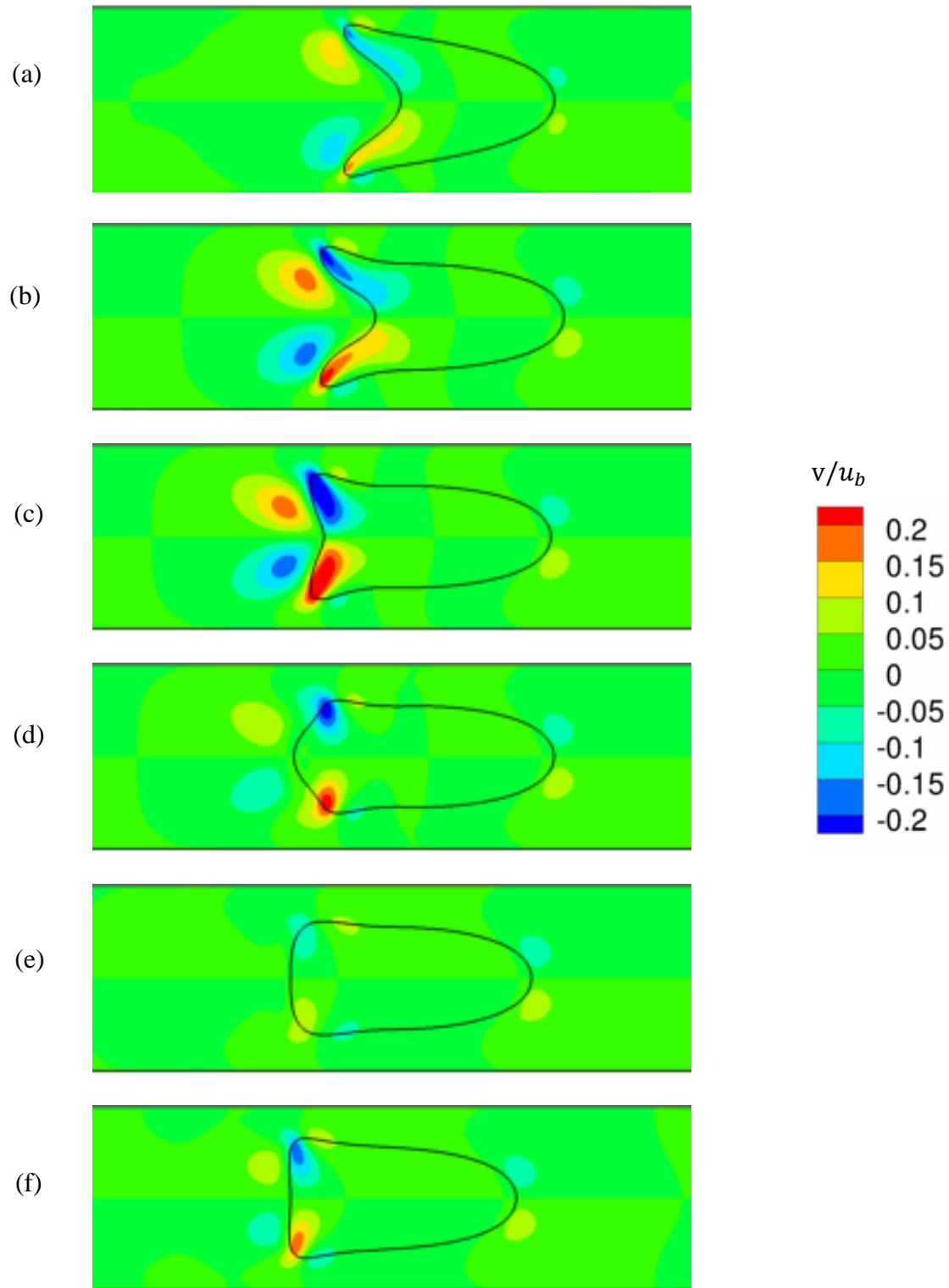


Figure 6.10: Duct center-plane wall-normal velocity contours overlaid with two-dimensional droplet shape, $\text{Ca} = 0.25$, $\lambda = 1$, $\text{Re} = 100$, (a) $t^* = 2$, (b) $t^* = 4$, (c) $t^* = 5$, (d) $t^* = 6$, (e) $t^* = 8$, (f) $t^* = 10.7$.

velocity at the axial leading and trailing edges, but as a result of the large difference in velocities for droplet material near the axis and droplet material near the wall.

To capture part of the self-similar behavior, we have plotted in *Figure 6.11* the successive characteristic times at which the difference in total and axial elongation occurs, for different capillary numbers. Such a correlation gives us a mapping between time-scales and stress parameters. In *Figure 6.11* we observe an approximately linear variation. That is the time at which the maximum difference occurs increases linearly with capillary number, within the range of capillary numbers investigated. The choice of relating the time-scale to the capillary number for this feature of deformation is arbitrary. However, we still may expect any other characteristic feature of deformation that is present at each of the capillary numbers (e.g. time at which minimum spreading occurs, period of oscillation in relaxation regime), to also scale linearly with the capillary number. The former observation assumes that all other parameters (Re , λ) remain constant, since variation of these parameters may result in new time scales, as we will see.

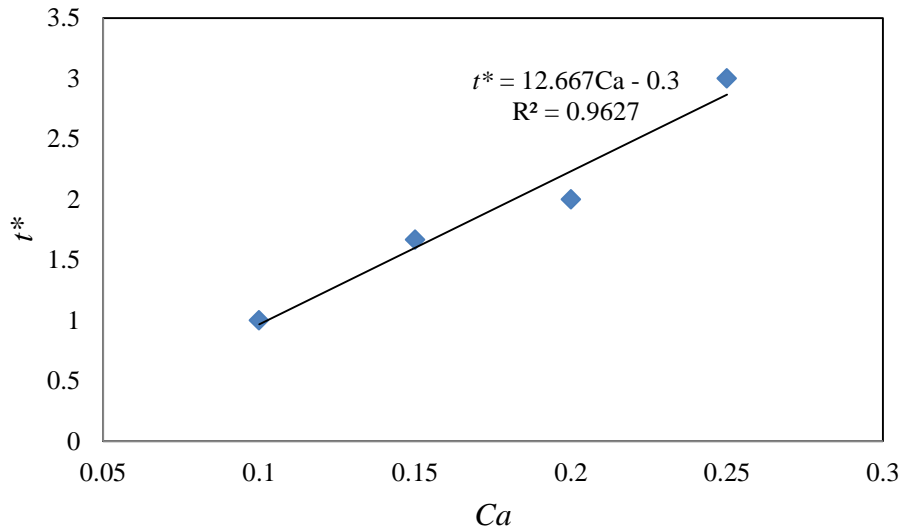


Figure 6.11: Characteristic time when $E - E_A$ is a maximum for different capillary numbers,
 $Re = 100, \lambda = 1$.

6.2.4 Effect of Reynolds Number

We now examine the effect of inertia on droplet deformation. Three-dimensional droplet contours are shown at different characteristic times in *Figure 6.12* for four duct-inlet Reynolds numbers. Characteristic deformation parameter histories are shown in *Figures 6.13, 6.14*. We observe that as the Reynolds number is decreased from a moderate value of 100 to a modest value of 10, its influence on deformation also decreases. We observe in *Figure 6.13a* and *Figure 6.14a* that the magnitudes of total elongation and spreading decrease as the Reynolds number decreases. Further, the change in the steady-state values of these deformation parameters

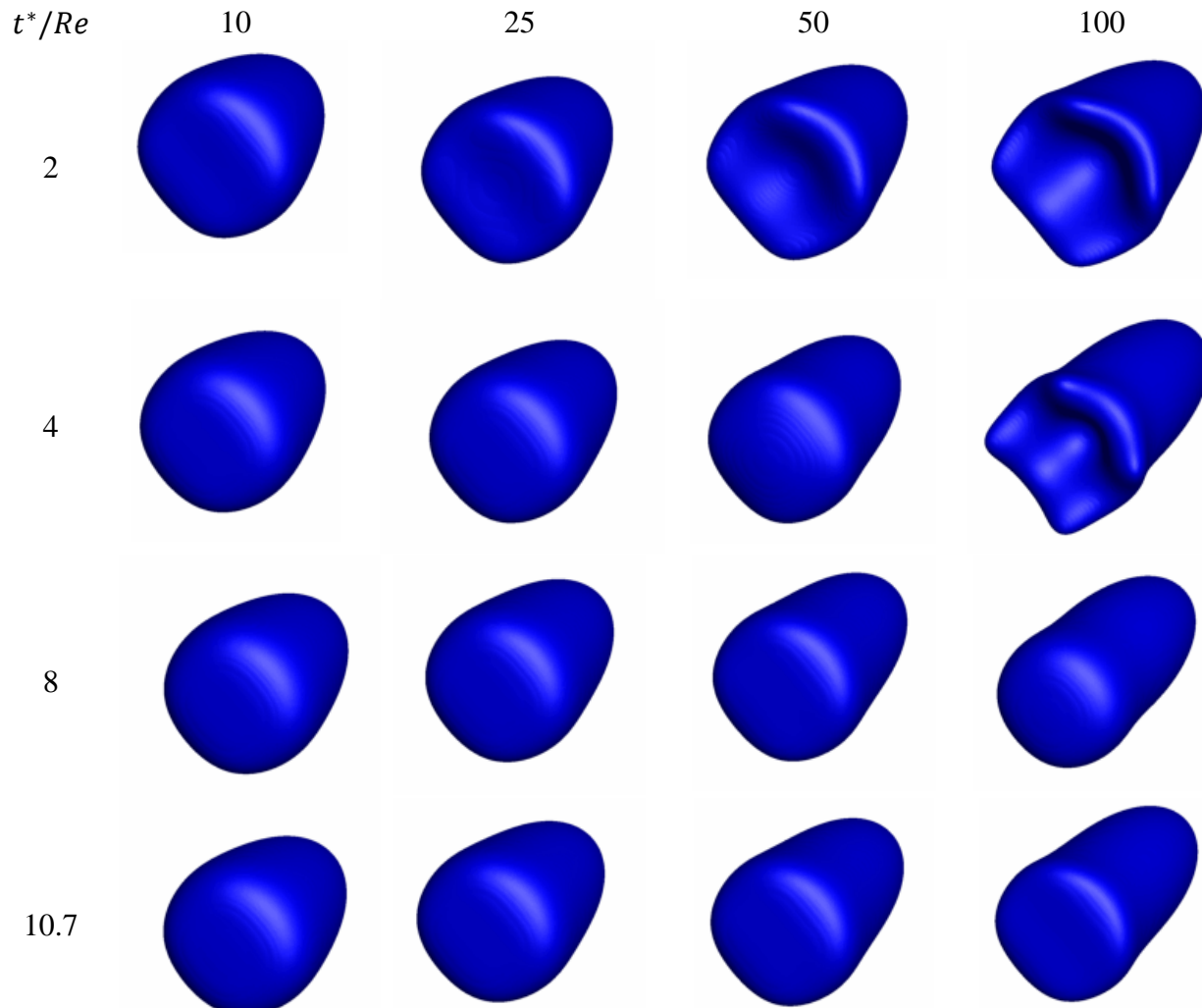


Figure 6.12: Droplet contour history for different Reynolds numbers, $\text{Ca} = 0.25, \lambda = 1$.

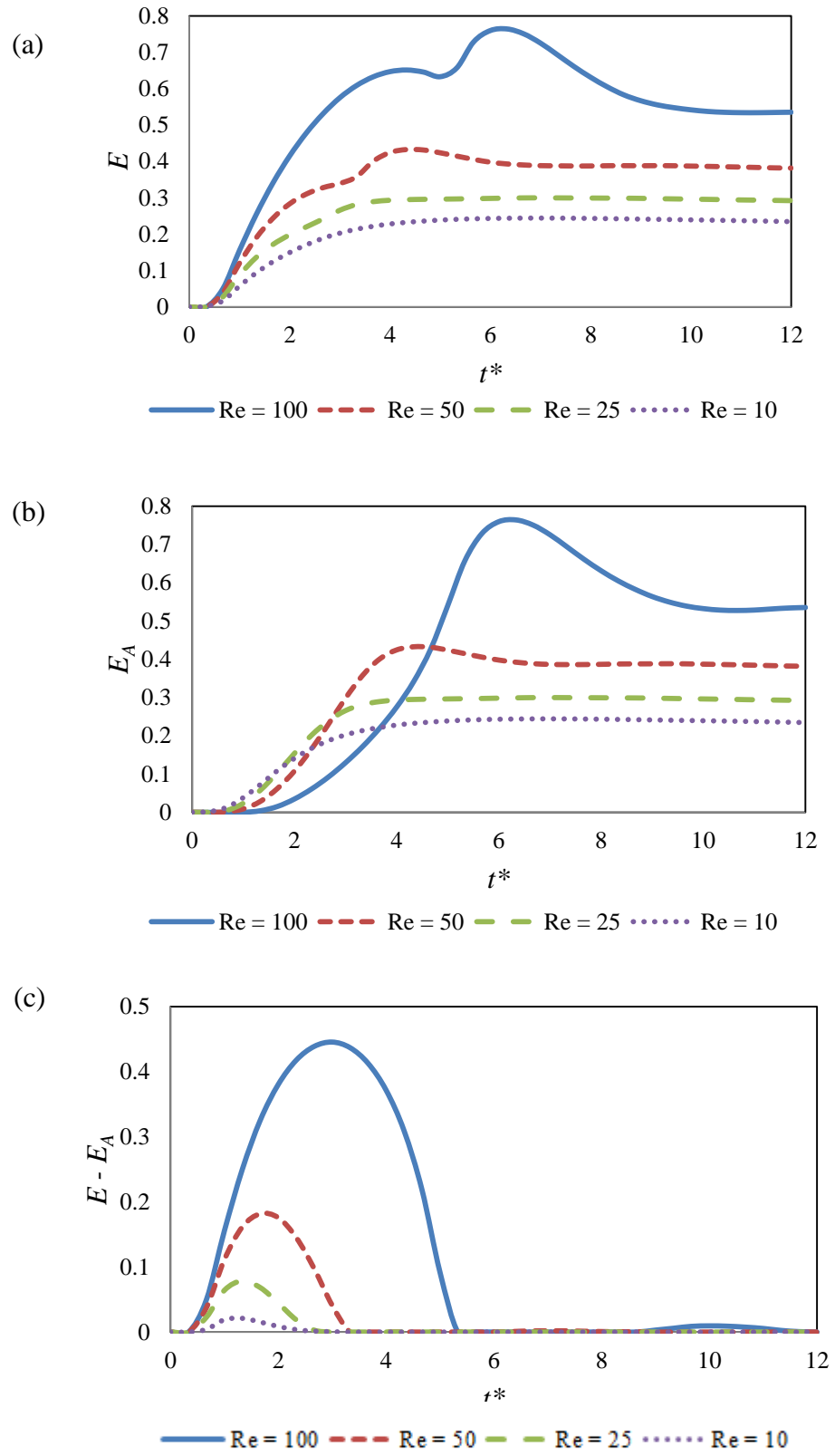


Figure 6.13: Reynolds number study, elongation (a) maximum, (b) axial, (c) difference, $\text{Ca} = 0.25, \lambda = 1$.

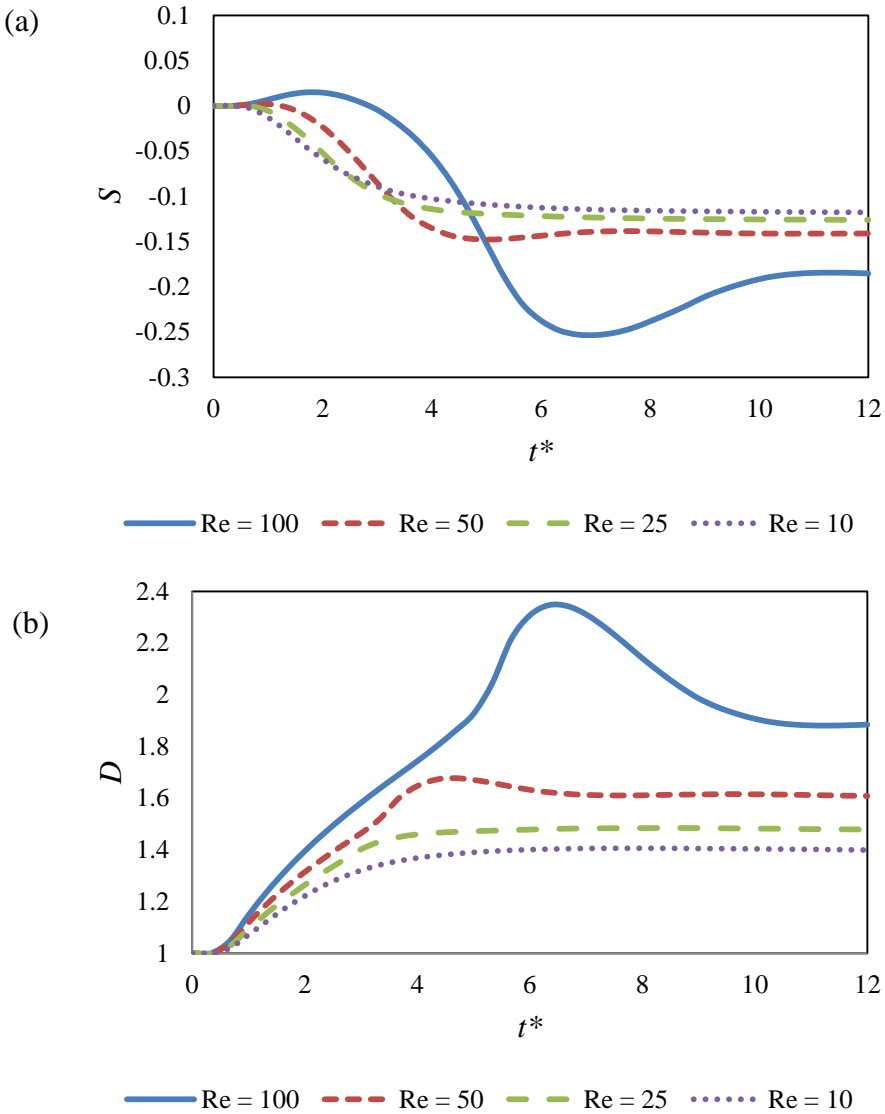


Figure 6.14: Reynolds number study, (a) spreading, (b) deformation, $\text{Ca} = 0.25, \lambda = 1$.

decreases even as the Reynolds number is decreased by a factor of 2 or greater between cases. Regarding the three-dimensional droplet contours in *Figure 6.12*, we observe little difference between the $\text{Re} = 10$, and $\text{Re} = 25$ cases. These observations suggest a convergence to the Stokes' limit, where droplet deformation becomes independent of Reynolds number. Certainly $\text{Re} = 10$ would not be considered the Stokes' limit in most practical regimes. However, as has been observed from the deformation parameter history, the decreasing influence of Reynolds

number as its own magnitude is decreased on both the steady and transient droplet deformation suggests a practical Stokes' limit may exist with regard to the inertial effect on deformation even for Re not much less than unity. In other words, $Re = O(1)$ or less may be sufficient to regard the droplet deformation as sufficiently Reynolds number independent.

Outside of the small Reynolds number limit however, it is clear the inertial parameter has a substantial effect on droplet deformation, both in the steady state magnitude and transient behavior. At early times for the $Re = 50$ and $Re = 100$ cases, a hollow cavity forms at the trailing edge of the droplet as near-wall droplet material is held-up and droplet material near the axis is relatively un-restrained. Regarding the deformation parameter in *Figure 6.14b* we observe that while the steady-state deformation varies approximately geometrically with the Reynolds number, the transient deformation may be increased by a greater amount as the Reynolds number is increased. For the $Re = 10$ and 25 cases, the deformation may be described as over-damped so that the steady-state deformation value is the maximum value. For $Re = 50$, the maximum overshoot in deformation is a magnitude of about 1.7 compared with the steady-state value of about 1.6. For $Re = 100$, the maximum transient deformation is almost 2.4 while the steady-state magnitude is approximately 1.9. This suggests that for moderate Reynolds numbers, the steady-state deformation magnitude may not be a fair representation of a droplet's deformation; an increasing Reynolds number underscores the importance of examining transient deformation behavior.

Finally, we seek a characteristic time that scales with the Reynolds number. In *Figure 6.15*, we plot the time at which the maximum difference in total vs. axial elongation occurs as a function of Reynolds number. The characteristic time's dependence on Reynolds number is clearer than in the case of varying capillary number. While the relationship may be described as

approximately linear, with an R^2 value greater than 0.9, we may also observe that little change in the characteristic time was observed between the $Re = 10$, and $Re = 25$ cases. Above these Reynolds numbers however, there was a significant increase in the time at which the maximum elongation difference occurred. This may suggest that there exists a critical Reynolds number below which the characteristic time is independent of Reynolds number (which may be indicative of a Stokes'-like limit) and a regime above the critical Reynolds number where the characteristic time is strongly influenced by Reynolds number. Recall a similar convergence was observed in the droplet deformation histories as the Reynolds number was decreased. A similar observation trend is observed in the next section.

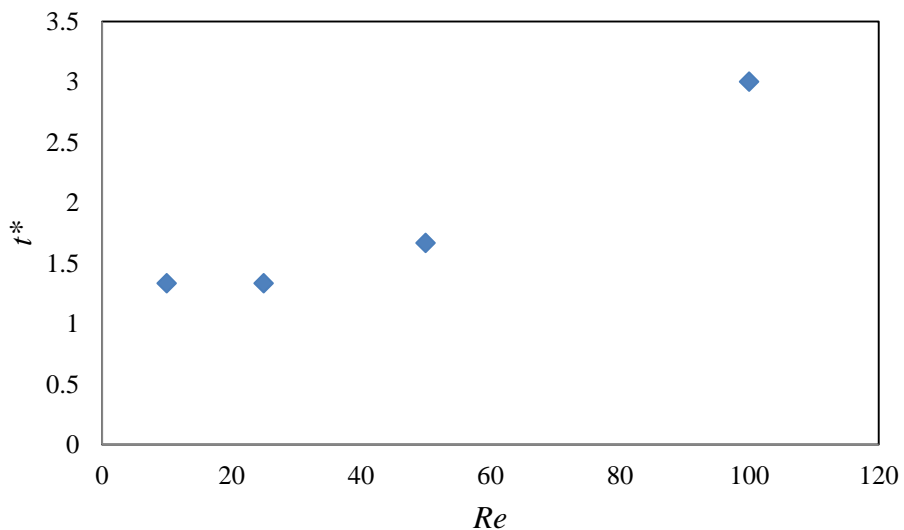


Figure 6.15: Characteristic time when $E - E_A$ is a maximum for different Reynolds numbers, $Ca = 0.25, \lambda = 1$.

6.2.5 Effect of Viscosity Ratio

Three-dimensional droplet contours for different viscosity ratios of order unity are shown in *Figure 6.16*. As is evident in these contours as well as the deformation histories in *Figures 6.17* and *6.18*, little difference in droplet shape is observed for small and intermediate times. The steady-state droplet elongation appears to have a moderate dependence on viscosity ratio while the spreading has a comparably modest dependence. The transient droplet elongation has a

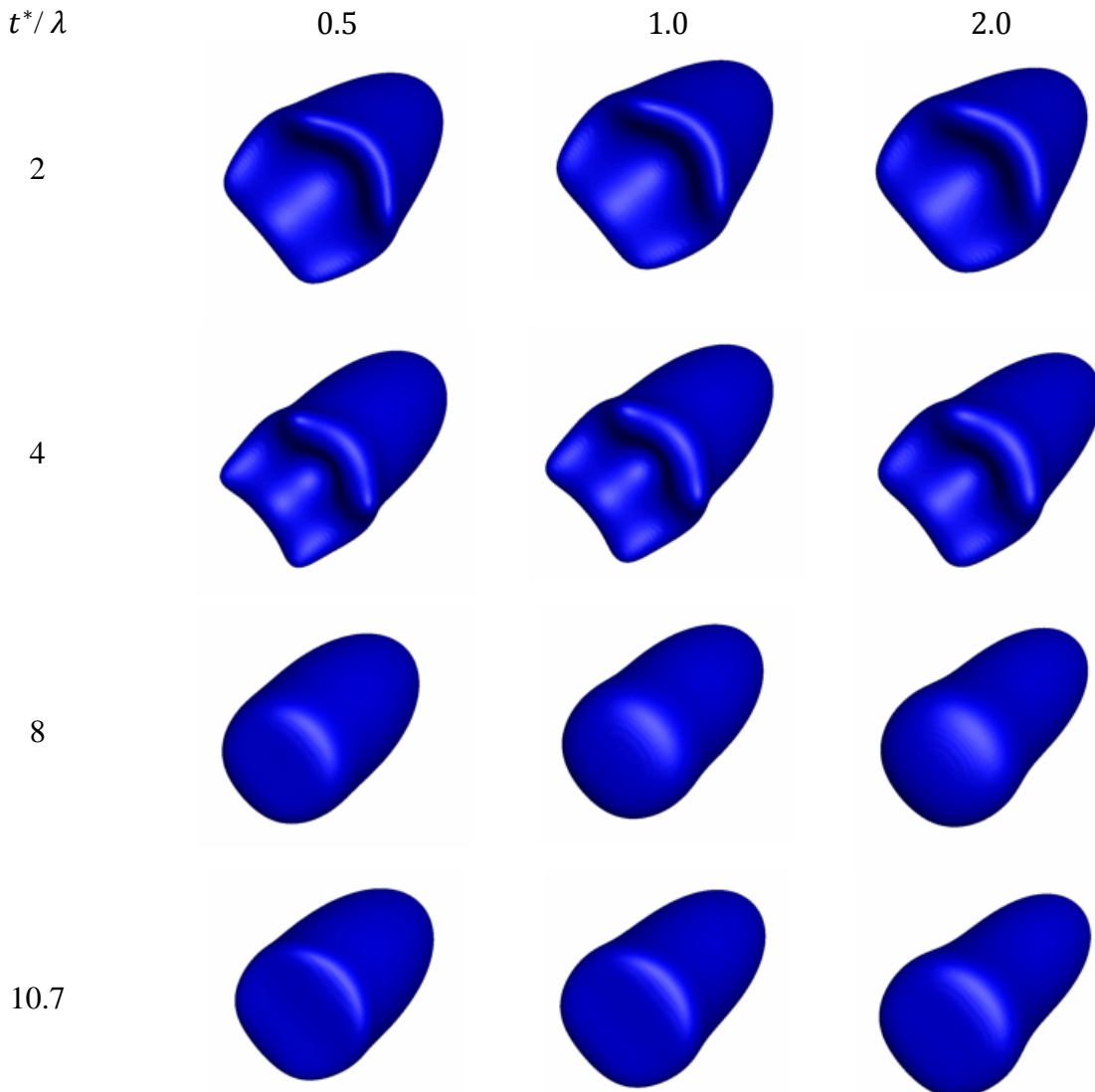


Figure 6.16: Droplet contour history for different viscosity ratios, $\text{Ca} = 0.25$, $Re = 100$.

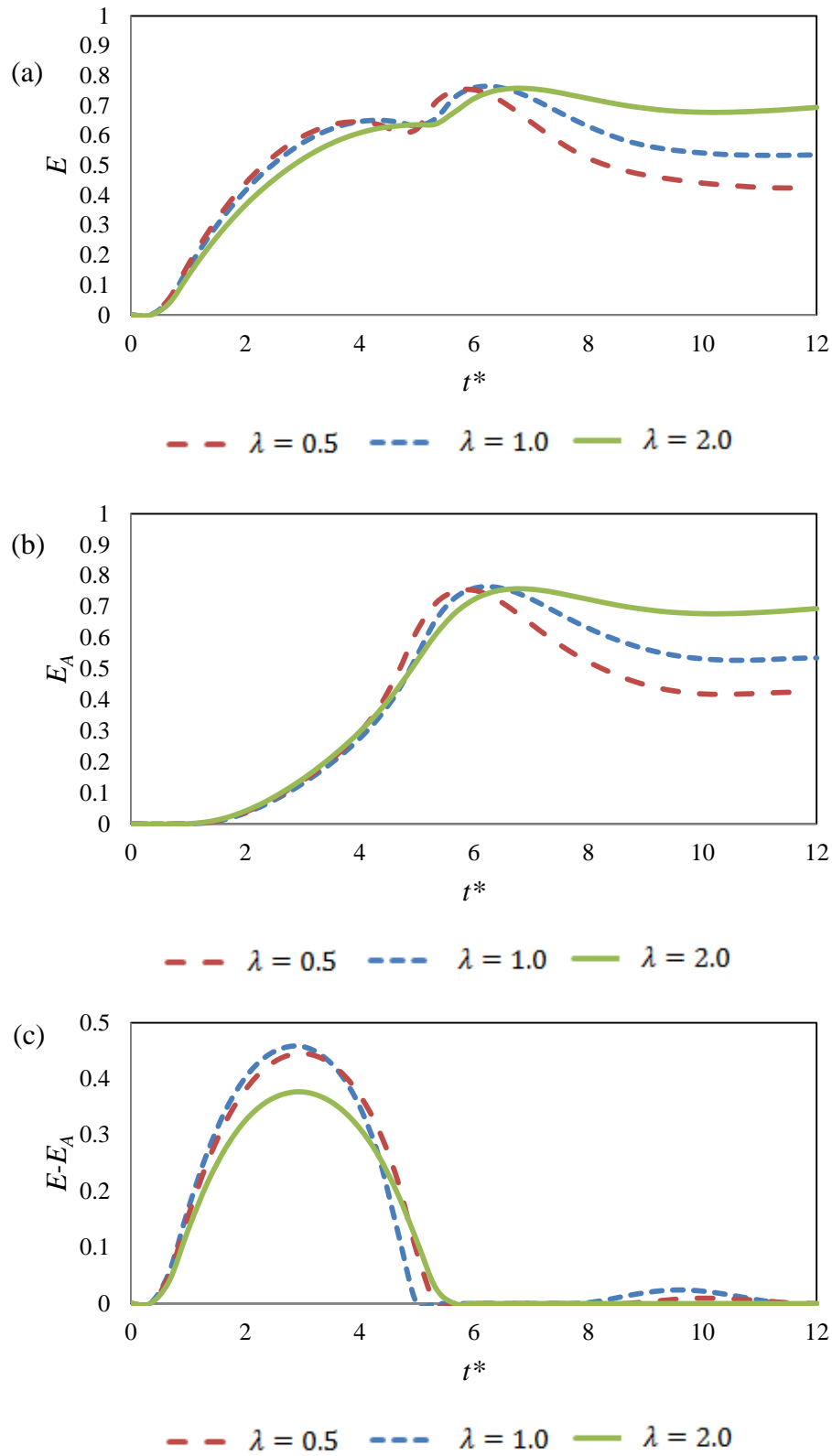


Figure 6.17: Viscosity Ratio study, elongation (a) maximum, (b) axial, (c) difference, $Ca = 0.25$, $Re = 100$.

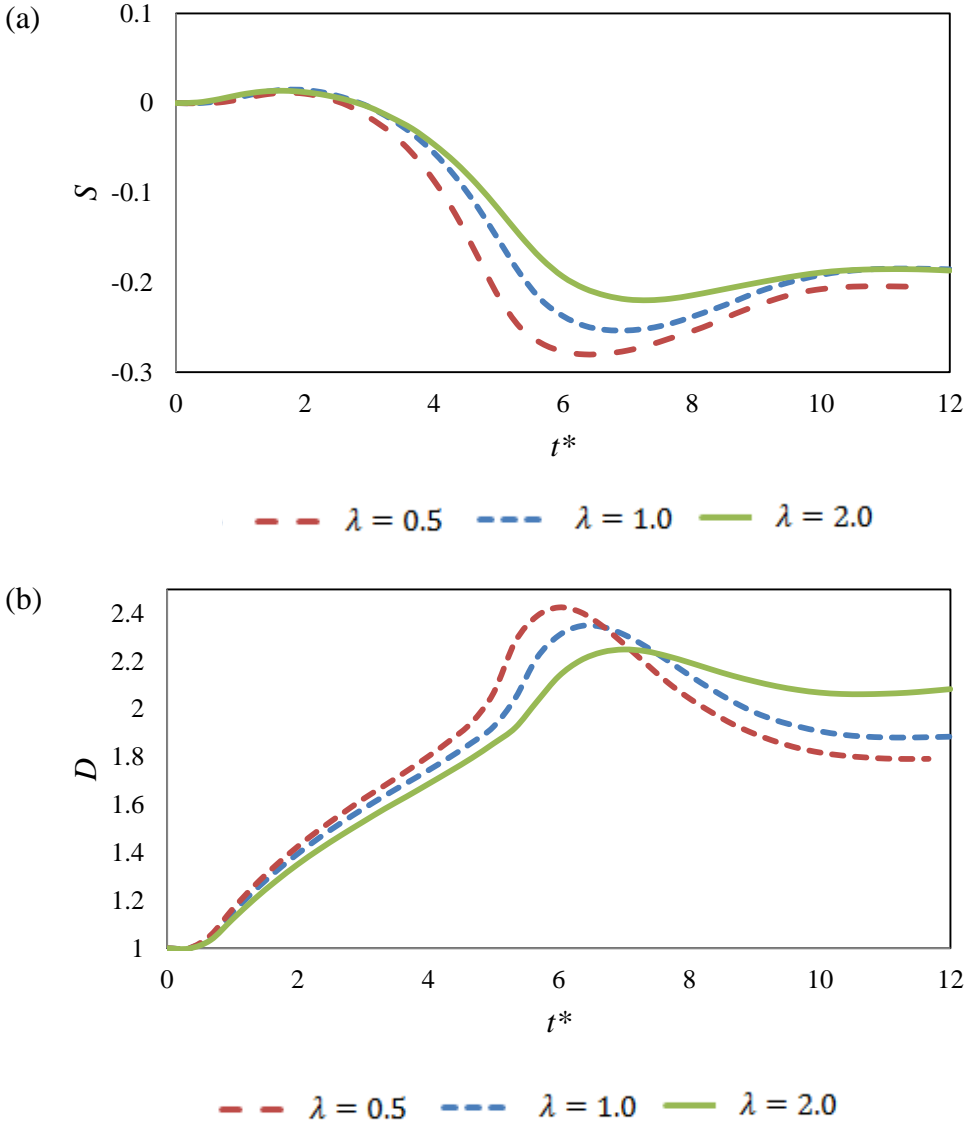


Figure 6.18: Viscosity ratio study, (a) spreading, (b) deformation, $\text{Ca} = 0.25$, $Re = 100$.⁴⁶

maximum that appears to be approximately independent of the viscosity ratio. However, the transient spreading magnitude appears to decrease as the viscosity ratio is increased. By conservation of mass (droplet volume), we expect there must exist an increasingly non-uniform droplet shape if the steady-state spreading decreases with viscosity ratio while the steady-state

⁴⁶ We were not able to observe the final data point in the $\lambda = 0.5$ case within the 10:1 duct length. When the droplet viscosity is less than the carrier fluid's, the droplet material represents a region of locally lower impedance to flow than the surrounding fluid. In this case, the mean droplet velocity is higher than that of the carrier fluid and therefore exits the domain in less time than more viscous droplets.

elongation increases with viscosity ratio. That is, the maximum wall-normal tip-to-tip droplet length is remaining close to its initial value even as the maximum stream-wise tip-to-tip distance is increasing. The only way this may occur is to have local region of high negative spread or wall-normal droplet squeezing. We may observe as the viscosity ratio is increased, the droplet's interface-to-wall distance becomes increasingly non-uniform over the length of the droplet. Regarding *Figure 6.16* at $t^* = 10.7$, the $\lambda = 0.5$ droplet has a roughly uniform thickness over its entire length except near its leading edge, while the $\lambda = 2.0$ steady-state shape is non-uniform, with a bulbous trailing edge, and a skinnier paraboloid-shaped leading edge that extends over a large length of the droplet. The trailing edge wall-normal tip-to-tip distance is approximately equal in each of these cases indicating that the wall-normal tip-to-tip distance is increasingly narrower, moving in the positive stream-wise direction, as the viscosity ratio is increased. Regarding *Figure 6.18b*, it is interesting to note that the maximum transient droplet deformation decreases with increase in the viscosity ratio. Evidently, the trade-off of increased elongation is a comparatively substantial reduction in negative spreading. However, the steady-state droplet deformation does increase as the viscosity ratio is increased. The preceding observations were relevant for viscosity ratios near unity, however in the next section we observe different deformation dynamics as the droplet viscosity is increased relative to the carrier fluid's.

We observe qualitatively different behavior for viscosity ratios increasingly greater than unity. Regarding *Figure 6.19*, as the viscosity ratio increases, the cavity region at the droplet trailing edge begins to disappear. For $\lambda = 16$ and 32 , little or no cavity region is discernible in the droplet contour plots. A small cavity may only be inferred by inspection of *6.20c* which suggests there is a difference in axial tip-to-tip and maximum stream-wise tip-to-tip distances,

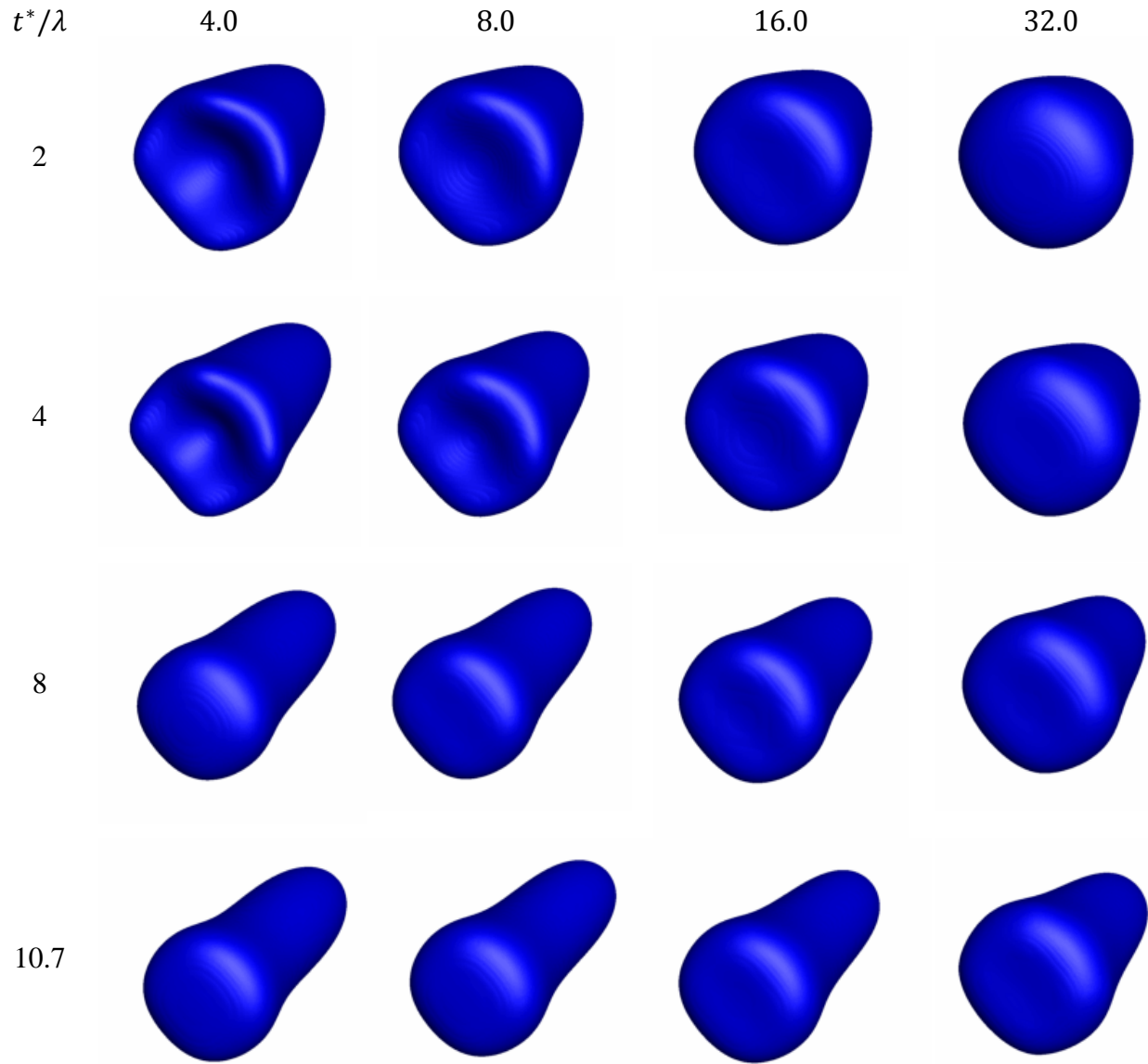


*Figure 6.19: Droplet contour history for different viscosity ratios (continued),
 $\text{Ca} = 0.25, \text{Re} = 100$.*

which implies the presence of a droplet trailing edge cavity. Clearly however the depth of the cavity, as quantified by the difference in total and axial elongations is much larger in the lower viscosity ratio cases.

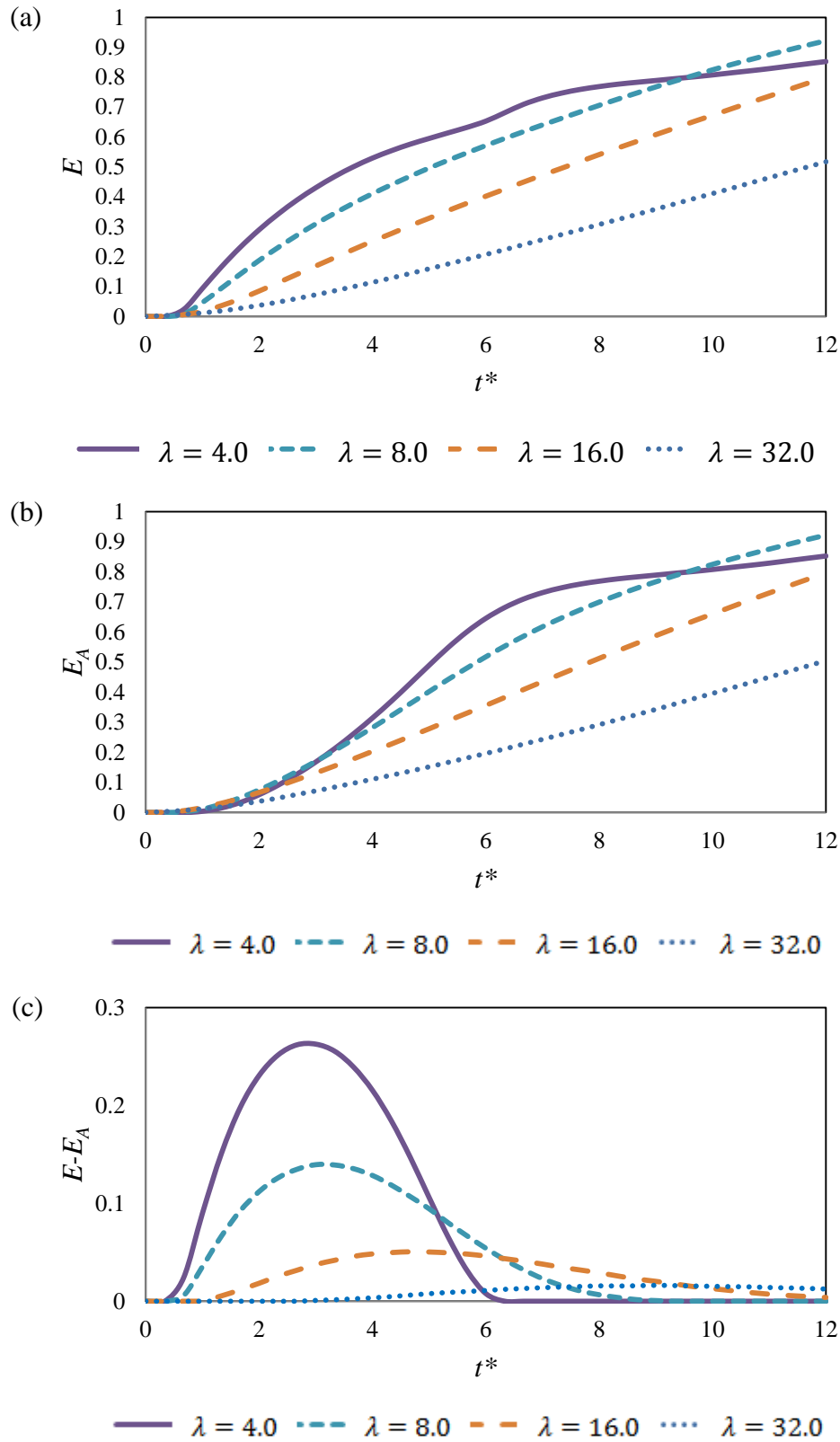


Figure 6.20: Viscosity ratio study (continued), elongation (a) maximum, (b) axial, (c) difference, $Ca = 0.25$, $Re = 100$.

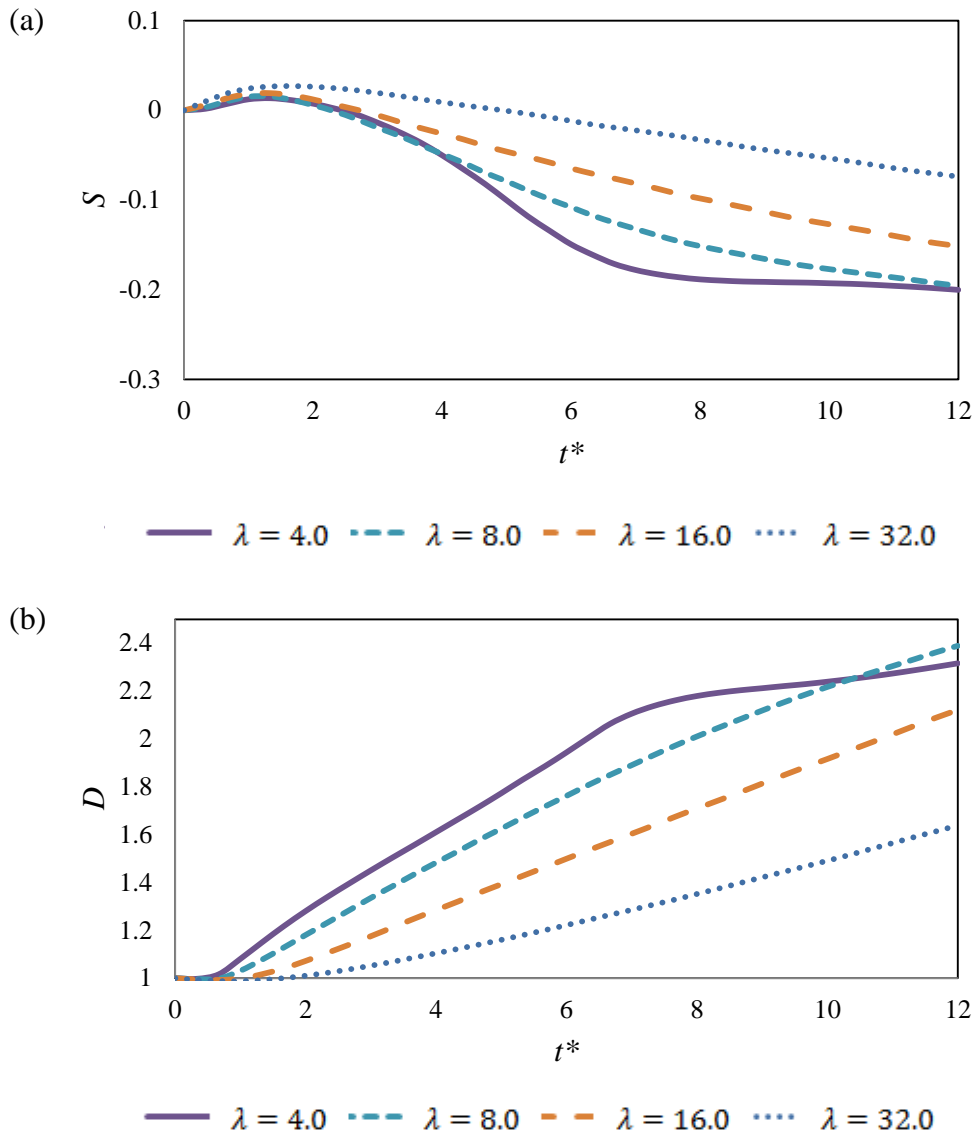


Figure 6.21: Viscosity ratio study (continued), (a) spreading, (b) deformation, $\text{Ca} = 0.25$, $Re = 100$.

The droplet deformation histories are remarkably different for the $\lambda > 4$ cases compared with the smaller viscosity ratio cases. For viscosity ratios greater than 4, no inflection point is present in the total elongation history. Even for this case, the elongation magnitude increases monotonically with time while the cases where $\lambda < 4$ described earlier in this section have both

inflection points and significant overshoots that develop as droplet material near the trailing edge is ejected backward relative to the droplet's center of mass. In cases where $\lambda \geq 8$, no such violent ejection is observable from the deformation histories.

The disappearance of inflection points in the elongation histories where the viscosity ratios are greater than or equal to 8 suggests a regime change where the viscosity ratio magnitude has strong influence on transient droplet deformation. Further evidence of this regime change is evinced in correlating a characteristic time scale with the viscosity ratio as shown in *Figure 6.22*.

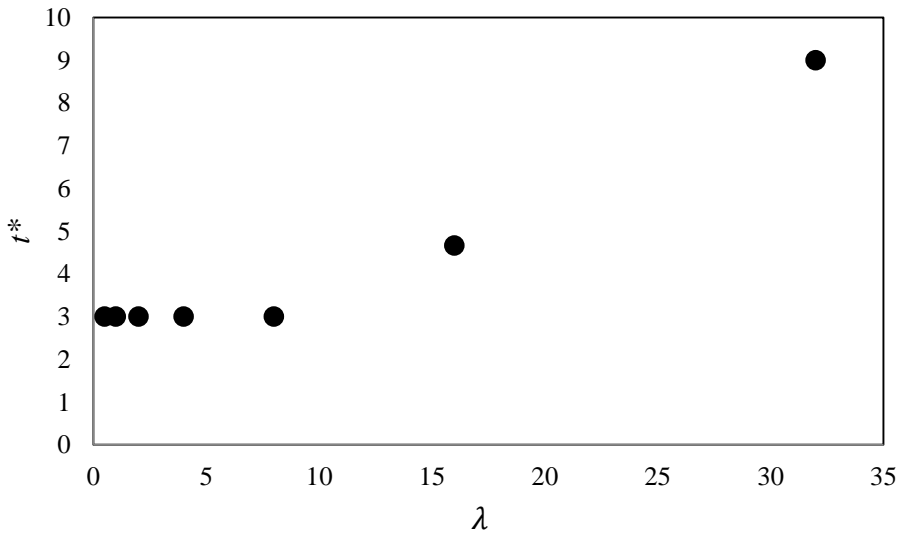


Figure 6.22: Characteristic time when $E - E_A$ is a maximum for different viscosity ratios, $Ca = 0.25$, $Re = 100$.

For viscosity ratios of order unity and even up to 8, little change is observed in the time at which the maximum elongation difference occurs. However, for viscosity ratios larger than 8, the characteristic time at which the maximum difference occurs increases significantly. While the duct length limited our observation window, it is speculated that the increase in viscosity ratio changed the characteristic system damping from a state of under-damping to a state of over-damping. We speculate the cases where the viscosity ratio is 8 and greater will experience monotonic elongation histories that asymptote to their steady-state magnitude. We expect the

spreading and total deformation histories to behave similarly after long times. Put another way, the viscosity ratio functions as an inverse inertial scale. For a high viscosity droplet, the flow in the droplet is of locally lower Reynolds number than the surrounding carrier fluid and consequently inertia plays a relatively minor role in its deformation. Inertia however plays a comparatively large role in the deformation of low viscosity ratio droplets, which allows the possibility of more complicated transient behavior such as overshoots and damped oscillations towards steady-state.

Finally, we may regard *Figure 6.23* to observe how the viscosity ratio affects the flow in the vicinity of the droplet. We observe that the flow is fully developed except in the neighborhood of the droplet for both the $\lambda = 1$ and $\lambda = 16$ cases. The mean stream-wise velocity is greater for the unity viscosity ratio case compared with the more viscous droplet. The droplet viscosity acts to resist droplet deformation which is a form of energy transfer from carrier to dispersed phase. Because the energy (and momentum) transfer is relatively inefficient for the $\lambda = 16$ case, the axial velocity of the highly viscous droplet lags the carrier-fluid's axial velocity resulting in a net imbalance between carrier fluid mass entering the duct near the axis and axially translating droplet mass. To conserve mass, carrier fluid is accelerated through narrow gaps between the droplet and duct walls resulting in greater wall shear-stress than would be present in a single-phase fully developed flow at the same Reynolds number. Further increase in the droplet viscosity relative to the carrier fluid viscosity would result in less deformation at any given time which would increase the velocity of the carrier-fluid in the near-wall region in the neighborhood of the droplet. In the limit of infinite viscosity ratio, we expect the carrier fluid to push the droplet as if it were a rigid-body. At a Reynolds number of 100, recirculation regions would certainly exist on the down-stream side of the droplet. This “wake” region may be

unsteady as a result of the squeezing flow regime between duct-wall and wall-normal droplet-carrier fluid interfaces.

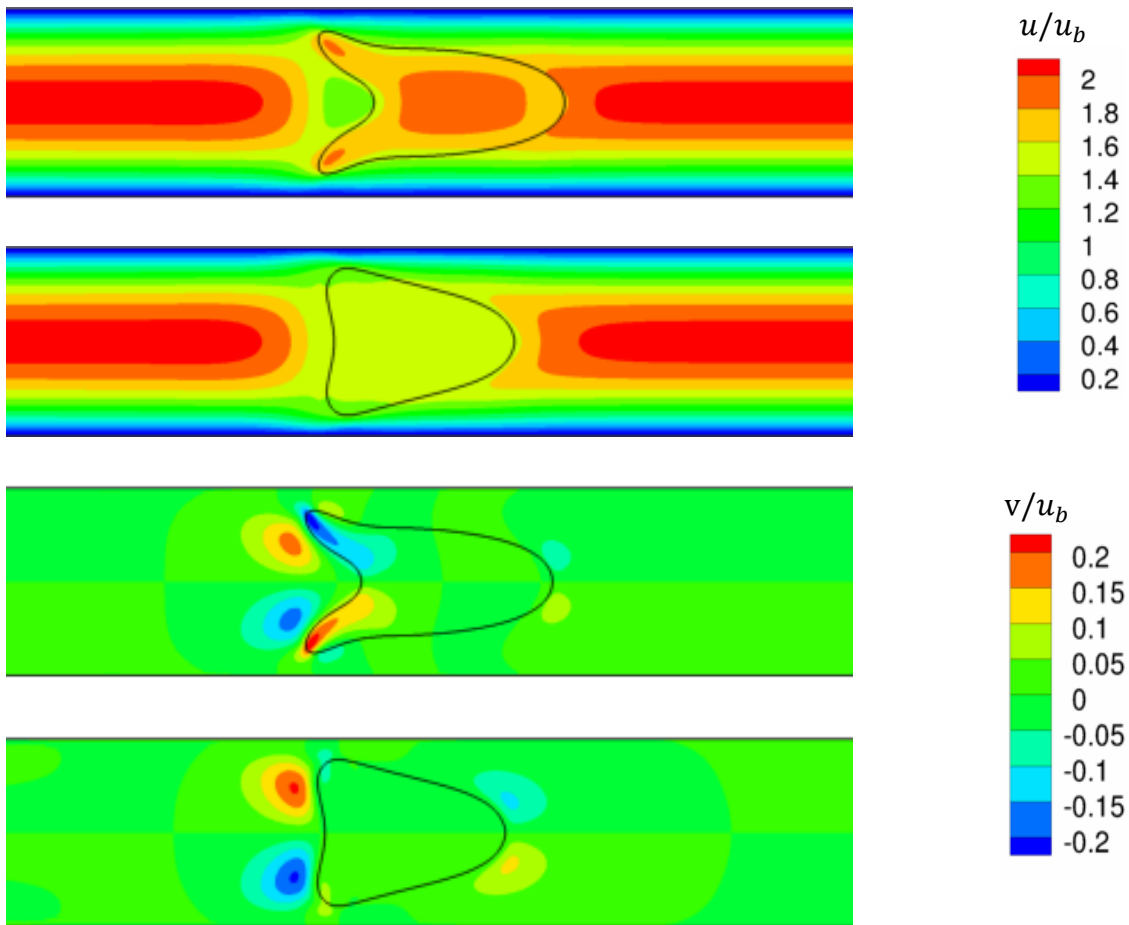


Figure 6.23: Velocity contours overlaid with 2D droplet interface for two viscosity ratios, (a) and (b) stream-wise velocity normalized by mean stream-wise velocity, (c) and (d) wall-normal velocity normalized by mean stream-wise velocity, $\lambda = 1$ for (a) and (c), $\lambda = 16$ for (b) and (d), $Re = 100$, $Ca = 0.25$, $t^*=4$ for both cases.

7. CONCLUSIONS

In this thesis, we presented the Lattice Boltzmann method (LBM) as a procedure for simulating multiphase flows. We introduced two widely used multiphase LBM algorithms, the Shan and Chen and He and Chen method and proposed a modification to the He and Chen algorithm incorporating a pressure Poisson equation, similar to that introduced by Inamuro [64]. By studying a two-dimensional droplet in a channel flow, we showed the modified H-C algorithm could significantly reduce density variation as a result of surface tension and density ratio. We also quantified some of density variation intrinsic to the H-C method for confined flows at modest Mach numbers and moderate Reynolds numbers. We explored a number of problems related to multiphase flow with applications to air conditioning and refrigeration including droplet impingement on smooth, liquid, and textured surfaces, head-on and oblique droplet collisions, and displacement flow in straight and complex micro-channels. This gave us insight into the breadth of problems that LBM is capable of simulating. In each of these cases, the limiting parameter is typically the density ratio. In the H-C method, density ratios higher than five were typically unstable. In the S-C method, vary high density ratios could be simulated by allowing two fluids to be modeled as two phases of the same fluid. Alternatively, multiple fluid components that did not share an EOS could be prescribed in the S-C formulation. In general, the S-C method was capable of simulating much higher density ratios. The tradeoff between the S-C and H-C methods was in the prescription of surface tension magnitude. In H-C, once the EOS was chosen, the surface tension magnitude could be chosen arbitrarily. In the S-C method, interaction forces were prescribed which in theory could be used to correlate or imply surface tension via a Laplace pressure difference. However, the surface tension magnitude could only be known *a posteriori* following a simulation. The arbitrary prescription of surface tension made the

H-C method more robust in simulating a range of problems that could be compared to results obtained in literature. The H-C method was used to simulate droplet deformation in a square-duct at moderate Reynolds number. Droplet deformation magnitude had a strong dependence on capillary number. For moderate Reynolds numbers, the deformation increased as the Reynolds number increased. As the Reynolds number approached the Stokes limit, the Reynolds number became a relatively unimportant parameter in the description of droplet deformation. Droplet to carrier viscosity ratio also played a prominent role in droplet deformation, especially as the viscosity ratio was increased to a magnitude much greater than unity. The droplet study gives us confidence in LBM, specifically H-C as a viable method in the simulation of multiphase flows provided the density ratio is close to unity. Because air conditioning and refrigeration applications often involve vary high density ratio flows, we conclude that the original H-C and S-C algorithms are not currently capable of accurately simulating these flows. The addition of the PPE in the modified H-C method gave some promise for LBM in simulating high density ratio flows. In addition, if the S-C method could be extended, such that interfacial tension could be prescribed *a priori*, this would significantly increase its robustness as a multiphase computational strategy. We hope this work gives readers some level of detail regarding the advantages and disadvantages of LBM as well as insight into the method's derivation, implementation, accuracy, and robustness. We have shown LBM to be a versatile method with regard to the problems it is capable of simulating. The square-duct, droplet deformation work represents a careful study demonstrating LBM as an accurate method, that can be validated with other computational methodologies, and perhaps most importantly, capable of uncovering novel multiphase flow physics.

REFERENCES

- [1] A. B. D. Cassie, S. Baxter, "Wettability of Porous Surfaces," *Trans. Faraday Soc.*, 1944, **40**, 546-551, DOI: 10.1039/TF9444000546.
- [2] A. Gupta, R. Kumar, "Droplet Impingement and breakup on a dry surface," *Computers and Fluids*, 39, (2010) 1696-1703.
- [3] A. Gupta, R. Kumar, "Effect of geometry on droplet formation in the squeezing regime in a microfluidic T-junction," *Microfluid Nanofluid* (2010) 8:799-812, DOI 10.1007/s10404-009-0513-7.
- [4] A. Gupta, R. Kumar, "Flow regime transition at high capillary numbers in a microfluidic T-junction: Viscosity contrast and geometry effect," *Phys. Fluids* **22**, 122001 (2010); doi: 10.1063/1.3523483.
- [5] A. Gupta, R. Kumar, "Two-Dimensional Lattice Boltzmann Model for Droplet Impingement and Breakup in Low Density Ratio Liquids," *Commun. Comput. Phys.* Vol. **10**, No.3, pp. 767-784, (2011), doi: 10.4208/cicp.221209.160910a.
- [6] A. Gupta, S.M.S. Murshed, R. Kumar, "Droplet formation and stability of flows in a microfluidic T-junction," *Appl. Phys. Lett.* **94**, 164107 (2009); doi: 10.1063/1.316089.

- [7] A. J. Griggs, A. Z. Zinchenko, R. H. Davis, “Low-Reynolds-number motion of a deformable drop between two parallel plane walls,” International Journal of Multiphase Flow 33 (2007) 182-206.
- [8] A. K. Gunstensen, D. H. Rothman, “Lattice Boltzmann model of immiscible fluids,” Phys. Rev. A, Vol. 43, No. 8 (1991).
- [9] A. L. Shimpi, D. Wilson. "Building NVIDIA's GT200." ANANDTECH. Web. <<http://www.anandtech.com/show/2549/2>>.
- [10] A. Nourbakhsh, S. Mortazavi, Y. Afshar, “Three-dimensional simulation of drops suspended in Poiseuille flow at non-zero Reynolds numbers,” Phys. Fluids **23**, 123303 (2011); doi: 10.1063/1.3663565.
- [11] A. Tiwari, S. P. Vanka, “A ghost fluid Lattice Boltzmann method for complex geometries,” *Int. J. Numer. Meth. Fluids* 2012; **69**:481–498.
- [12] A. Vananroye, P. J. A. Janssen, P.D. Anderson, P.V. Puyvelde, P. Moldenaers, “Microconfined equiviscous droplet deformation: Comparison of experimental and numerical results,” Phys. Fluids **20**, 013101 (2008); doi: 10.1063/1.2835312.
- [13] B. P. Ho, L. G. Leal, “The creeping motion of liquid drops through a circular tube of comparable diameter,” J. Fluid Mech. Vol. 71, part 2, pp.361-383.

- [14] B. Sakakibara, T. Inamuro, “Lattice Boltzmann simulation of collision dynamics of two unequal-size droplets,” *Int. J. Heat. Mass Trans.* 51 (2008) 3207-3216.
- [15] D. B. Kirk, W. W. Hwu. *Programming Massively Parallel Processors: a Hands-on Approach*. Burlington, MA: Morgan Kaufmann Publ., 2010. Print.
- [16] D. Qian, A. Lawal, “Numerical study on gas and liquid slugs for Taylor flow in a T-junction microchannel,” *Chem. Eng. Sci.* 61 (2006) 7609-7625.
- [17] D. R. Noble, S. Chen, J. G. Georgiadis, R. O. Buckius, “A consistent hydrodynamic boundary condition for the Lattice Boltzmann method,” *Phys. Fluids* 7, 203 (1995); doi: 10.1063/1.868767.
- [18] E. Lac, J. D. Sherwood, “Motion of a drop along the centerline of a capillary in a pressure-driven flow,” *J. Fluid Mech.* (2009) vol. 640, pp.27-54.
- [19] F. M. White, *Viscous Fluid Flow*, 3rd Ed., McGraw-Hill (2006).

- [20] G. B. Jeffery, “The Motion of Ellipsoidal Particles Immersed in a Viscous Fluid,” *Proc. R. Soc. Lond. A* 1922 102, doi: 10.1098/rspa.1922.0078.

- [21] G. Coupier, A. Farutin, C. Minetti, T. Podgorski, C. Misbah, “Shape Diagram of Vesicles in Poiseuille Flow,” Phys. Rev. Letters **108**, 178106 (2012).
- [22] G. Hestrini, S. Haber, E. Wacholder, “The flow fields in and around a droplet moving axially within a tube,” J. Fluid Mech. (1970), **41**, 4, pp.689-705.
- [23] G. I. Taylor, “The Formation of Emulsions in Definable Fields of Flow,” Proc. R. Soc. Lond. A 1934 **146** doi:10.1098/rspa.1934.0169.
- [24] G. K. Batchelor, *An Introduction to Fluid Dynamics*, Cambridge Mathematical Library.
- [25] H. A. Stone, “Dynamics of Drop Deformation and Breakup in Viscous Fluids,” *Annu. Rev. Fluid Mech.* 1994. 26:65-102.
- [26] H. Lan, D. Khismatullin, “A numerical study of the lateral migration and deformation of drops and leukocytes in a rectangular microchannel,” International Journal of Multiphase Flow 47 (2012) 73-84.
- [27] H. L. Goldsmith, S. G. Mason, “Axial Migration of Particles in Poiseuille Flow,” Nature 1961 **190**, 1095-1096.
- [28] J. Chao, R. Mei, R. Singh, W. Shyy, “A filter-based, mass-conserving lattice Boltzmann method for immiscible multiphase flows,” *Int. J. Numer. Meth. Fluids* 2011: **66**:633-647.

- [29] J. U. Brackbill, D. B. Kothe, C. Zemach, “A Continuum Method for Modeling Surface Tension,” *J. Comp. Phys.* **100**, 335-354 (1992).
- [30] J. Zhang, “Acceleration of Five-Point Red-Black Gauss-Seidel in Multigrid for Poisson Equation,” *Applied Mathematics and Computation*, 80:73-93 (1996).
- [31] K. C. Sahu, S. P. Vanka, “A multiphase lattice Boltzmann study of buoyancy-induced mixing in a tilted channel,” *Computers & Fluids* 50 (2011) 199-215.
- [32] L. Amaya-Bower, and T. Lee, “Lattice Boltzmann simulations of bubble formation in a microfluidic T-junction,” *Phil. Trans. R. Soc. A* (2011) 369, 2405–2413, doi:10.1098/rsta.2011.0025.
- [33] M. A. Khan, Y. Wang, “Droplet motion in a microconfined shear flow via a three-dimensional spectral boundary element method,” *Phys. Fluids* **22**, 123301 (2010); doi: 10.1063/1.3525357.
- [34] M. A. Rahman, A. M. Jacobi, “Experimental Study of Wetting Anisotropy and Condensate Drainage Enhancement on Microgrooved Aluminum Surface,” *Proceedings of ASME 2011 Int. Mech. Eng. Cong. & Expo. (IMECE2011)*, Nov. 11-17, 2011, Denver, CO.

[35] M. Cheng, J. Hua, J. Lou, “Simulation of bubble-bubble interaction using a lattice Boltzmann method,” *Computers and Fluids*, **39**, 2, 260 (2010).

[36] M. De Menech, P. Garstecki, F. Jousse, H.A. Stone, “Transition from squeezing to dripping in a microfluidic T-shaped junction,” *J. Fluid Mech.* (2008), vol. 595, pp. 141–161.
doi:10.1017/S002211200700910X.

[37] M. Mishra, A. D. Wit, K. C. Sahu, “Double diffusive effects on pressure-driven miscible displacement flows in a channel,” *J. Fluid Mech.* (2012), vol. 712, pp. 579-597.
doi:10.1017/jfm.2012.439.

[38] M. R. Swift, W. R. Osborn, J. M. Yeomans, “Lattice Boltzmann Simulation of Nonideal Fluids,” *PRL*, Vol. 75, No. 5, (1995).

[39] M. Shapira, S. Haber, “Low Reynolds Number Motion of A Droplet Between Two Parallel Plates,” *Int. J. Multiphase Flow* Vol. 14, No.4 pp.483-506, 1988.

[40] M. Shapira, S. Haber, “Low Reynolds Number Motion of a Droplet in Shear Flow including Wall Effects,” *Int. J. Multiphase Flow*, Vol. 16, No.2, pp. 305-321, 1990.

[41] N. F. Carnahan, K. E. Starling, “Equation of State for Nonattracting Rigid Spheres,” *J. Chem. Phys.* **52**, 2, (1969).

- [42] N. K. Omebere-Iyari, B. J. Azzopardi, “A Study of Flow Patterns for Gas/Liquid Flow in Small Diameter Tubes,” *Trans IChemE, Part A, Chemical Engineering Research and Design*, 2007, 85(A2): 180–192.
- [43] NVIDIA Corporation, “CUDA C Programming Guide,” *NVIDIA*. Web. <docs.nvidia.com/cuda/pdf/CUDA_C_Programming_Guide.pdf>. (2012).
- [44] P. Garstecki, M.J. Ruerstman, H.A. Stone, G.M. Whitesides, “Formation of droplets and bubbles in a microfluidic T-junction—scaling and mechanism of break-up,” *Lab Chip*, 2006, **6**, 437-446. DOI: 10.1039/b510841a.
- [45] P. J. A. Janssen, P. D. Anderson, “A boundary-integral model for drop deformation between two parallel plates with non-unit viscosity ratio drops,” *J. Comp. Phys.* 227, (2008) 8807-8819.
- [46] P. J. Janssen, P. D. Anderson, “Boundary-integral method for drop deformation between parallel plates,” *Phys. Fluids* **19**, 043602 (2007); doi:10.1063/1.2715621.
- [47] P. L. Bhatnagar, E. P. Gross, and M. Krook, “A model for collision process in gases. I. Small amplitude processes in charged and neutral one-component system,” *Phys. Rev.* **94**, 511 (1954).

[48] P. R. Redapangu, K. C. Sahu, S. P. Vanka, “A study of pressure-driven displacement flow of two immiscible liquids using a multiphase lattice Boltzmann approach,” *Phys. Fluids* **24**, 102110 (2012); doi: 10.1063/1.4760257.

[49] P. Yuan, L. Schaefer, “Equations of state in a lattice Boltzmann model,” *Physics of Fluids* **18**, 042101 (2006), doi: 10.1063/1.21187070.

[50] Q. Zou, X. He, “On pressure and velocity boundary conditions for the lattice Boltzmann BGK model,” *Phys. Fluids* **9**, 1591 (1997); doi: 10.1063/1.869307.

[51] R. N. Wenzel, “Resistance of Solid Surfaces to Wetting by Water,” *Industrial and Eng. Chem.* Vol 28, No. 8, 988-994, (1936).

[52] R. K. Singh, K. Sarkar, “Inertial effects on the dynamics, streamline topology and interfacial stresses due to a drop in shear,” *J. Fluid Mech.* (2011) vol. 683, pp.149-171.

[53] R. Zhang, X. He, S. Chen, “Interface and surface tension in incompressible lattice Boltzmann multiphase model,” *Computer Physics Communications* 129 (2000) 121-130.

[54] S. Chandra, C.T. Avedisian, “On the Collision of a Droplet with a Solid Surface,” *Proc. R. Soc. Lond. A* 1991 **432**, 13-41, doi: 10.1098/rspa.1991.0002.

- [55] S. Chapman, T.G. Cowling, “The Mathematical Theory of Non-Uniform Gases,” Cambridge Mathematical Library, 3rd ed.
- [56] S. Chen, G. D. Doolen, “Lattice Boltzmann Method for Fluid Flows,” *Annu. Rev. Fluid Mech.* **30**: 329-64 (1998).
- [57] S. Chen, Z. Wang, X. Shan, G. D. Doolen, “Lattice Boltzmann Computational Fluid Dynamics in Three Dimensions,” *J. Stat. Phys.*, Vol. 68, Nos. 3/4 1992.
- [58] S. K. Doddi, P. Bagchi, “Lateral migration of a capsule in a plane Poiseuille flow,” *International Journal of Multiphase Flow* 34 (2008) 966-986.
- [59] S. Mortazavi, G. Tryggvason, “A numerical study of the motion of drops in Poiseuille flow. Part 1. Lateral migration of one drop,” *J. Fluid Mech.* (2000), vol. 411, pp.325-350.
- [60] S. Mukherjee, J. Abraham, “A pressure-evolution-based multi-relaxation-time high-density-ratio two-phase lattice-Boltzmann model,” *Computers & Fluids* **36** (2007) 1149-1158.
- [61] S. P. Schofield, M. A. Christon, V. Dyadechko, R. V. Garimella, R. B. Lowrie, B. K. Swartz, “Multi-material incompressible flow simulation using the moment-of-fluid-method,” *Int. J. Numer. Meth. Fluids.* 2010; **63**:931-952.

- [62] S. S. Chikatamarla, I. V. Karlin, “Lattices for the lattice Boltzmann method,” Phys. Rev. E **79**, 046701 (2009).
- [63] T. Inamuro, S. Tajima, F. Ogino, “Lattice Boltzmann simulation of droplet collision dynamics,” Int. J. Heat. Mass Trans. 47 (2004) 4649-4657.
- [64] T. Inamuro, T. Ogata, S. Tajima, N. Konishi, “A lattice Boltzmann method for incompressible two-phase flows with large density differences,” *J. Comp. Physics* 198 (2004) 628-644.
- [65] T. Lee, C. Lin, “A stable discretization of the lattice Boltzmann equation for simulation of incompressible two-phase flows at high density ratio,” *J. Comp. Phys.* **206**, 16-47, (2005).
- [66] V. Sibillo, G. Pasquariello, M. Simeone, V. Cristini, S. Guido, “Drop Deformation in Microconfined Shear Flow,” PRL **97**, 054502 (2006).
- [67] W. L. Olbricht, L.G. Leal, “The Creeping motion of liquid drops through a circular tube of comparable diameter: the effect of density differences between the fluids,” *J. Fluid Mech.* (1982), vol. 115, pp.187-216.
- [68] W. Wang, Z. Liu, Y. Jin, Y. Cheng, “LBM simulation of droplet formation in micro-channels,” Chemical Engineering Journal 173 (2011) 828-836.

- [69] X. Gu, A. Gupta, R. Kumar, “Lattice Boltzmann Simulation of Surface Impingement at High-Density Ratio,” *J. Therm. Phys. Heat. Trans.* **23**, 4, (2009). DOI: 10.2514/1.44032.
- [70] X. He, R. Zhang, S. Chen, G.D. Doolen, “On the three-dimensional Rayleigh-Taylor instability,” *Phys. Fluids* Vol. 11, No.5, (1999).
- [71] X. He, S. Chen, R. Zhang, “A Lattice Boltzmann Scheme for Incompressible Multiphase Flow and its Application in Simulation of Rayleigh-Taylor Instability,” *J. Comp. Phys.* **152**, 642-663, (1999).
- [72] X. He, X. Shan, G. D. Doolen, “Discrete Boltzmann equation model for nonideal gases,” *Phys. Rev. E*, Vol. 57, No. 1, (1998).
- [73] X. Shan, “Analysis and reduction of the spurious current in a class of multiphase lattice Boltzmann models,” *Phys. Rev. E*, **73**, 047701 (2006).
- [74] X. Shan, G. Doolen, “Multicomponent Lattice-Boltzmann Model with Interparticle Interaction,” *J. Stat. Phys.* Vol. 81, Nos. 1/2 1995.
- [75] X. Shan, H. Chen, “Lattice Boltzmann model for simulating flows with multiple phases and components,” *Phys. Rev. E*, Vol. 47, No. 3, 1993.

[76] Y. H. Kim, W. Choi, J. S. Lee, “Water droplet properties on periodically structured superhydrophobic surfaces: a lattice Boltzmann approach to multiphase flows with high water/air density ratio,” *Microfluid Nanofluid* (2011) 10:173-185, DOI 10.1007/s10404-010-0658-4.

[77] Y. Kataoka, T. Inamuro, “Numerical simulations of the behaviour of a drop in a square pipe flow using the two-phase lattice Boltzmann method,” *Phil. Trans. R. Soc. A* (2011) **369**, 2528-2536, doi:10.1098/rsta.2011.0041.

[78] Y. Wang, P. Dimitrakopoulos, “Low-Reynolds-number droplet motion in a square microfluidic channel,” *Theor. Comput. Fluid Dyn.* (2012) 26:361-379.

[79] Z. Yu, O. Hemminger, L.-S. Fan, “Experiment and lattice Boltzmann simulation of two-phase gas-liquid flows in micro-channels,” *Chemical Engineering Science* 62 (2007) 7172-7183.

APPENDIX

A. Brief Review of Kinetic Theory

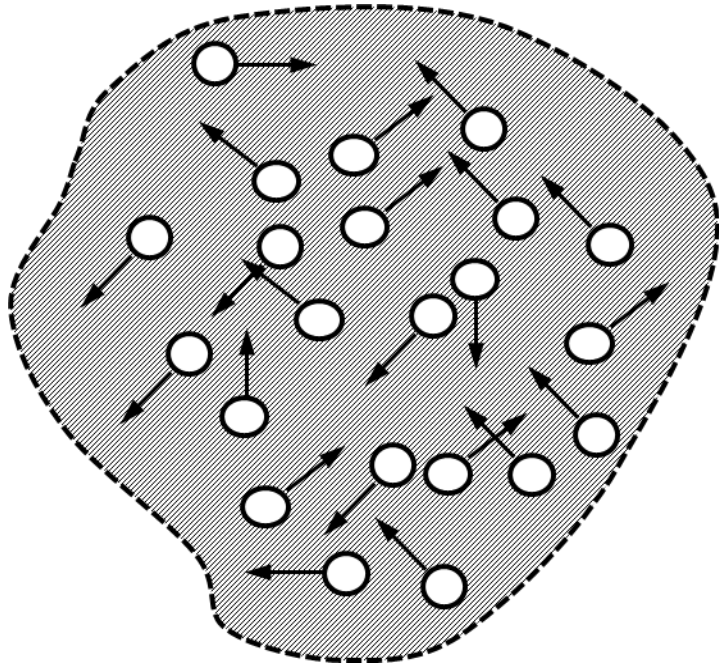


Figure A.1: Instantaneous snapshot of molecules and their respective velocity vectors in an arbitrary control volume.

It is substantive to briefly discuss the relevant theory used in the derivation of the LBM equations. Shown in *Figure A.1* is a collection of fluid molecules⁴⁷ in an arbitrary control volume. Arrows denote hypothetical instantaneous velocity vectors for each of these molecules. In principle, it is possible to determine how such a closed system evolves by writing a force balance for each molecule, and a conservation relationship ensuring the total number of particles is conserved. Such a formulation is deemed “Lagrangian.” From a physical standpoint, it would be nice to capture every piece of physics in such a system, that is the position and momentum of each molecule could be tracked for an arbitrary amount of time. However, from a practical

⁴⁷ The term fluid “molecules” should not be confused with the term fluid “element” which will follow and be defined in the context of the continuum hypothesis.

standpoint, it would become prohibitively expensive (from a computational standpoint say) to track every molecule for any practical system size. For example, a 6 ounce glass of water contains approximately 9.85 moles, or about 5.93×10^{24} water molecules. To circumvent this impasse, we seek an alternative description. The traditional alternative is the “Eulerian” formulation. In the Eulerian formulation, the notion of individual fluid molecules loses all meaning. In this formulation, a fluid comprised of many molecules is described in terms of its macroscopic properties, that is, measurable quantities such as density, viscosity, pressure, temperature, and velocity. As discussed in Batchelor [24], it becomes necessary to introduce the concept of a continuum via the continuum hypothesis. In essence, the hypothesis says that in the system being examined, there must exist a large separation of length scales, such that at any point⁴⁸, an average or macroscopic quantity can be defined. At the smallest extreme, the relevant flow scale is the mean free-path, the characteristic separation distance between molecules. At such a scale, a continuum description is not appropriate. That is, any measurable quantity—temperature for instance—would change so rapidly over small separation distances that no such average temperature description would be appropriate. At the other extreme, there exists a characteristic length scale where macroscopic variation in properties is easily measured. Such a length scale could be the size of a room⁴⁹, say, since it is easy to imagine a room that is cold on one side in exposure to a draft, and warm on the other in proximity to a lit fireplace. Therefore, the continuum hypothesis says there must exist an intermediate length scale between these extremes. Such a length scale has finite size and contains many fluid molecules. This length scale is called a “point” and the collection of molecules in a control volume of this size is deemed a fluid “element.” When we speak of the Eulerian description, macroscopic properties

⁴⁸ To be defined.

⁴⁹ The distance over which changes in macroscopic properties is discernible is certainly much smaller than a room, but the former is used as a simple illustrative example.

are defined under the preceding notions. Therefore, in this new description, the notion of individual molecules has lost all meaning. However, in many practical engineering problems, it is the macroscopic properties (flow-rate, pressure drop, etc.) that are of interest, and the dynamics of each molecule are immaterial.

Interestingly, the Lattice Boltzmann Method is an Eulerian formulation built-up from a Lagrangian perspective. Referring to *Figures A.1 and A.2*, we could imagine at one instance in time, counting the total number of molecules (N) inside this control volume that each have an instantaneous velocity ξ , and construct a number distribution containing an N for every magnitude of ξ encountered. If the size of the control volume is taken to be a point, defined in

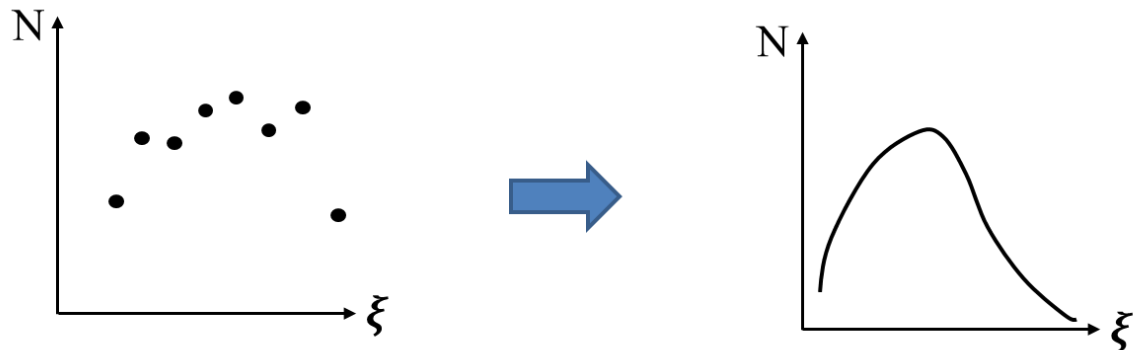


Figure A.2: Transition from discrete to continuous particle distribution as the number of molecules sampled becomes large.

the context of the continuum hypothesis, then the number distribution is no longer recognizable as discrete points, but rather a continuous distribution over realizable molecular velocities. Alternatively, this number distribution may be referred to as a number density since the total number of molecules in the control volume can be calculated by integrating the distribution over all possible molecular velocities:

$$N_t \equiv \text{total molecules} = \int N d\xi \quad (\text{A.1})$$

A related concept is the particle distribution function (pdf) which is defined in (A.2):

$$f(\xi, x, t) = \frac{N(\xi) \times MM}{\text{unit volume}} \quad (\text{A.2})$$

where MM is the molecular mass of the single particle species in the control volume. The fundamental volume unit is m^3 in SI. The arguments of f are shown to emphasize its dependence on the velocities ξ of the molecular species in the control volume. Further, if instead of one control volume, we consider a finite macroscopic domain where each point in the domain has a measurable macroscopic particle distribution function, then the pdf may be said to vary spatially at each location x, in the domain. The final argument allows the possibility for the shape of the pdf to change with time. Under these conditions, we may define familiar quantities:

$$\rho \equiv \frac{\text{total mass}}{\text{unit volume}} = \int f d\xi \quad (\text{A.3})$$

$$\rho u = \int \xi f d\xi \quad (\text{A.4})$$

Where ρ and u are the fluid density and velocity at any point in the domain, respectively. A special case to consider is when the pdf does not vary spatially or temporally. Then the expressions for density and momentum are invariant since the integrands on the right hand of side of (A.3) and (A.4) respectively do not change. Using Boltzmann's H-Theorem, Maxwell showed that the pdf corresponding to a uniform steady state of molecules has the form given in (A.5) [55, 71]:

$$f^{eq} = \frac{\rho}{(2\pi RT)^{3/2}} e^{-\frac{(\xi-u)^2}{2RT}} \quad (A.5)$$

Where T is the macroscopic temperature and R is the specific gas constant. It is interesting to note that Maxwell's distribution is described by both small scale features, viz. the molecular velocity ξ , and large scale features, viz. measurable quantities such as temperature, velocity, and density.

To allow for more complicated system dynamics, we must allow for the possibility that the pdf changes in time. The most general expression for the evolution of the pdf is given by the Boltzmann equation in (A.6) [55]:

$$\frac{\partial f}{\partial t} + \xi \cdot \nabla f = -F \cdot \frac{\partial f}{\partial \xi} + \left(\frac{\partial f}{\partial t} \right)_{coll} \quad (A.6)$$

The left hand side of (A.6) possesses a form similar to that of a material derivative, however the current form is expressed in terms of molecular velocities ξ , so that the traditional label of a material derivative is not appropriate. The right hand side of (A.6) contains two terms, the first represents the effect of body forces on the evolution of the pdf while the second term represents the effect of molecular collisions on variation in the pdf. Note that the Boltzmann equation, in the same vein as the Maxwell distribution, contains explicit macroscopic and microscopic effects. In acknowledgement of the range of scales present in the governing equation, this continuum model is often referred to as "mesoscopic."

We have already assumed the pdf itself to be a measurable or macroscopic quantity, F , the forcing term will turn out to also be expressible in terms of macroscopic quantities but will similarly contain an understanding that this macroscopic form is built up from microscopic interactions. Therefore, the latter and the former terms are quantities measurable at a point, as previously defined. With the notion of measurability, the collision term so too must be understood as the net effect of collisions to change the shape of the pdf, as can be measured at a point. That is, the time and length scales of each collision make it impossible to observe them in the Lagrangian sense so we must surrender to the net measurable result. The form of the forcing term requires more discussion which will be addressed in sections 2.2 and 2.3. The final note regards the collision term.

To the best of the author's knowledge no simple close-form analytical expression exists for the collision term. Chapman and Cowling [55] present an integral expression assuming the collection of molecules is of low enough density such that only binary collisions need to be considered. Such an expression may be suitable for gases. However if such a model is capable of handling liquid fluids, this expression will not be appropriate. Further, the integral expression itself introduces unclosed terms to equation (A.6) which themselves would require modeling. The simplest and most common expression given for the collision term was expressed by Bhatnagar, Gross, and Krook in 1954 [47] and is typically referred to as the BGK-approximation (A.7):

$$\left(\frac{\partial f}{\partial t}\right)_{coll} \approx -\frac{f - f^{eq}}{\tau} \quad (A.7)$$

Where f^{eq} was given in (A.5) and τ is called the relaxation time. The BGK-approximation is written with the assumption that the net effect of collisions is to "relax" the pdf toward

equilibrium at a constant rate with characteristic relaxation time given by τ and can be derived using Taylor series arguments [57]. The physical rationale for a uniform relaxation rate is the same as the argument suggesting that momentum transfer by diffusion is characterized by a single viscosity for Newtonian fluids. As it turns out, the two quantities will be related. That is, the time scale over which relaxation occurs will turn out to be proportional to the efficiency in the propagation of information, be it spatial gradients in the distribution function or in momentum. While some authors [60] for example have used collision models incorporating multiple relaxation times (MRT), the BGK-approximation is the most widely used due to its simplicity and physical connection to momentum diffusivity (kinematic viscosity). For redundancy we write the complete Boltzmann equation with BGK-approximation, which forms the foundation of most widely used LBM algorithms:

$$\frac{\partial f}{\partial t} + \xi \cdot \nabla f = -F \cdot \frac{\partial f}{\partial \xi} - \frac{f - f^{eq}}{\tau} \quad (A.8)$$

Before presenting the LBM algorithms implemented in this investigation, we emphasize the Boltzmann equation is the evolution equation for a single pdf, that is, for the distribution function of molecules of a single type, where the notion of a fluid is defined in the context of the continuum hypothesis. The application of the continuous model to multiphase flows will not be considered here. Rather, multiphase LBM algorithms are presented in the methods section of Chapter 2 where careful attention is given to distinguish the differences between the single and multiphase algorithms.